UNIVERSITÀ
DELLA CALABRIA

Dottorato di Recerca in:

Scienze ed Ingegneria dell'Ambiente, delle Costruzioni e dell'Energia

(XXIX CICLO)

Synthesis and Characterization of Nanomaterials:
Graphene, Silicene and Carbon Nano-Onions

S.S.D-FIS/01 – FISICA SPERIMENTALE

Tutor:

Prof. **Lorenzo S. CAPUTI**

Coordinatore:

Prof. **Salvatore CRITELLI**

Dottorando:

Salih Mohamed OSMAN

Rende/ 2017

Dedication

To my late father, God bless his soul,

To my mother, wish you wellness,

To my lovely wife and kids,

I dedicate this Research.

ACKNOWLEDGMENT

Undertaking this PhD has been a truly life-changing experience for me and it would not have been possible to do without the support and guidance that I received from many people.

So, firstly I would like to sincerely thank my supervisor ***Prof. Lorenzo S. Caputi*** for his excellent guidance, he knew how to guide my research thanks to his high vision in both scientific and general cultures, I am indebted to him indefinitely.

Also I would like to thank the educational institutions in Sudan; University of Kassala and MOHE for their estimated support.

My thanks extend also to the members of Laboratory of Surface Nanoscience for their friendship and for providing me the best conditions to carry out my research. Particularly, I want to thank ***Dr. Anna Cupolillo*** for her valuable guidance, kindness and professionalism in the scientific matters which have allowed me to be more efficient throughout the period of my research. Also I express special thanks to all my seniors and juniors colleagues in the lab; Nadia, Denia, Marlon, Diana, Francesca and Andrea for the good teamwork and lovely friendship environment they have given me.

I am also grateful to my family support. I would like to thank my kind mother for her encouragement, wishes and her continuous prayers to achieve and complete my work. Also I would like to thank my brothers and sisters for their constant support and encouragement. In particular I thank my own family; wife and children for their encouragement and patience throughout the PhD period, I owe to them.

Finally, I would like to express my deep appreciation to all the friends I have known at the UNICAL, in particular to all Sudanese friends for the wonderful moments we have spent together.

Rende/Italy, July 2017 Salih M. Osman

CONTENTS

List of Figures

ABSTRACT

The electronic structure of the graphene/Ni(111) system was investigated by means of electron energy-loss spectroscopy (EELS). A single layer of graphene has been obtained on Ni(111) by dissociation of ethylene. Angle-resolved EEL spectra show a low energy plasmon dispersing up to about 2 eV, resulting from fluctuation of a charge density located around the Fermi energy, due to hybridization between Ni and graphene states. The dispersion is typical of a two-dimensional charge layer, and the calculated Fermi velocity is a factor of ~0.5 lower than in isolated graphene. The interface-π plasmon, related to interband transitions involving hybridized states at the K point of the hexagonal Brillouin zone, has been measured at different scattering geometries. The resulting dispersion curve exhibits a square root behavior, indicating also in this case a two-dimensional character of the interface charge density. As well**,** it has been shown that it is possible to use EELS in the reflection mode to measure the fine structure of the carbon K-edge in monolayer graphene on Ni(111), thus demonstrating that reflection EELS is a very sensitive tool, particularly useful in cases where the TEM-based ELNES cannot be applied.

Clean Ag(111) surface and the two phases of silicene on Ag(111), mixed (4×4, √13×√13R19°, 2√3×2√3R30°) and 2√3×2√3R30, have been studied by XPS, LEED and EELS. EEL spectra of the Ag(111) surface covered by silicene in the (4×4, √13×√13R19°, 2√3×2√3R30°) mixed phase shows a well-defined plasmon peak whose center is located at about 1.75 eV. The 2√3×2√3R30° phase shows EEL spectra that exhibit a peak located at about 0.75 eV loss, which moves clearly towards higher energies with increasing momentum transfer. The typical parabolic dispersion relation obtained from such spectra confirms that the peak is due to a collective excitation which is evidently associated to the silicene layer. These plasmons associated to silicene have never been observed in the past. Our results show that the plasmonic properties of silicene on Ag(111) are strongly dependent on the geometrical arrangement of Si atoms with respect to the substrate.

Carbonaceous nanomaterials have been obtained by underwater arc discharge between graphite electrodes. TEM images showed that the resulting particles suspended in water consist of CNOs with other carbonaceous materials such as CNTs and graphene. We observed for the first time the formation of a solid agglomerate on the cathode surface. Raman and TEM studies

revealed that the agglomerate is made exclusively of CNOs. The defragmentation of such agglomerate allows to obtain CNOs free of other carbonaceous materials without the complex purification procedures needed for floating nanomaterials.

ABSTRACT
(Italian Version)

La struttura elettronica del sistema grafene / Ni (111) è stata studiata mediante la spettroscopia di perdita di energia di elettroni (EELS). Un singolo strato di grafene è stato ottenuto sul Ni (111) mediante dissociazione di etilene. Gli spettri EEL risolti in angolo mostrano un plasmone a bassa energia che disperde fino a circa 2 eV, derivante dalla fluttuazione di densità di carica situata intorno all'energia di Fermi, a causa dell'ibridizzazione tra stati Ni e grafene. La dispersione è tipica di un materiale bidimensionale e la velocità di Fermi calcolata presenta un fattore inferiore di ~ 0,5 rispetto a quello del grafene isolato. Il plasmone di interfaccia-π, correlato alle transizioni interbanda che coinvolgono stati ibridati al punto M della zona esagonale di Brillouin, è stato misurato in differenti geometrie di dispersione. La curva di dispersione risultante mostra una dipendenza dell'energia dalla radice del vettotr d'onda, indicando anche in questo caso un carattere bidimensionale della densità di carica dell'interfaccia. Inoltre, è stato dimostrato che è possibile utilizzare la spettroscopia EEL in riflessione per misurare la struttura fine della linea K del carbonio nel sistema grafene/Ni (111), dimostrando quindi che l'EELS in riflessione è uno strumento molto sensibile, particolarmente utile nei casi in cui EELS-TEM non possa essere applicata.

Il silicene è stato sintetizzato mediante crescita epitassiale di atomi di silicio su un substrato di Ag (111). Il grado di ordine dello strato ottenuto è stato verificato mediante la diffrazione di elettroni a bassa energia (LEED). Osservazioni LEED rivelano la formazione di due fasi ordinate in funzione della temperatura del substrato. Alla temperatura di sintesi T=270°C, la nostra osservazione LEED rivela la sovrapposizione di tre strutture ordinate 4×4, $\sqrt{13}\times\sqrt{13}R19°$, $2\sqrt{3}\times2\sqrt{3}R30^{\circ}$, mentre all'aumentare della tempratura è stato possible osservare il pattern LEED della fase $2\sqrt{3}\times2\sqrt{3}R30^{\circ}$. Le misure di perdita di energia risolte in angolo realizzate per le due fase evidenziano che le proprietà plasmoniche del Silicene cresciuto su Ag(111) sono fortemente influenzate dalla disposizione geometrica degli atomi di silicio rispetto al substrato. Sono stati osservati plasmoni per entrambe le fasi. Il valore del plasmone di perdita di energia ottenuto nel caso della fase (4×4, $\sqrt{13}\times\sqrt{13}R19°$, $2\sqrt{3}\times2\sqrt{3}R30^{\circ}$), localizzato ad 1.75 eV, corrisponde sorprendentemente all'energia del plasmone calcolato per il silicene free-standing. Tale modo elettronico, attribuibile al silicene, non è mai stato osservato in lettreratura.

I CNO, costituiti da strati concentrici di atomi di carbonio con ibridizzazione sp^2 e dimensioni dell'ordine delle decine di nanometri, sono stati sintetizzati mediante scarica elettrica in acqua tra elettrodi di grafite ed investigati attraverso microscopia a trasmissione elettronica (TEM) e spettroscopia Raman. Dopo la realizzazione del processo di scarica, è stato possibile rilevare la presenza di nanoparticelle sospese in acqua (nanotubi, nano-onios, graphene e carbone amorfo) e di un agglomerato situato sulla superficie del catodo mai osservato in letteratura. Al fine di spiegare la formazione di tale agglomerate, abbiamo proposto un nuovo processo di cristallizzazione in cui si è ipotizzato che la cristallizzazione non sia dovuta al gradiente di temperatura tra plasma e acqua, ma al gradiente localizzato nelle immediate vicinanze della superficie del catodo, che durante la scarica si mantiene ad una temperatura sensibilmente inferiore rispetto a quella dell'anodo. Tale meccanismo di cristallizzazione genera probabilmente strati di materiale nanostrutturato che si sovrappongono fino a formare, sulla superficie del catodo, un solido che ha l'apparenza della grafite, ma che, sottoposto a indagini con spettroscopia Raman e microscopia elettronica in trasmissione, si dimostra essere costituito da un agglomerato CNO, con scarse quantità di altri tipi di materiali carboniosi (nanotubi, carbonio amorfo).

CHAPTER ONE

INTRODUCTION

The origin of nanoscience usually is associated with a 1959 lecture by Richard Feynman [1]. Possibly, the first use of the term "nanotechnology" in the scientific literature was in a 1974 paper involving "ion-sputter machining" by Taniguchi [2]. The first nanotechnology journal, *Nanotechnology*, was launched in 1990 by the Institute of Physics in the United Kingdom. The number of publications related to nanotechnology mirrors the historical time line. Results from a Web of Science search combining the terms "nanomaterial," "nanoparticle," and "nanostructure" show dramatic growth in published papers (Figure 2.1), from less than 100 in 1990 to almost 45,000 in 2011.

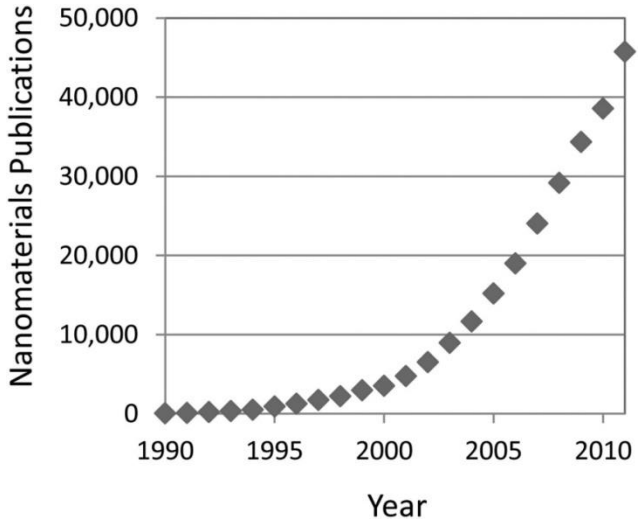

Figure 2.1: Graph shows dramatic growth in published papers related to nanotechnology.

Nanotechnology is part of a natural progression in many different areas of science coupled with development of new tools that enable researchers to see, model, and control structures at the nanometer scale. Although, in many ways, nanotechnology is not new, experimental and computational tool development enables research to be done that was not previously possible. New approaches can be taken to address previously intractable problems. Therefore, nanoscience and nanotechnology do not represent a new discipline, but rather advancements within several disciplines and a convergence of concepts and ideas across disciplines. As such, nanotechnology introduces important new ideas and cross-fertilization that enables scientific breakthroughs and development of various new technologies.

Some of the most intriguing materials are those only a single atom thick. These two-dimensional materials, such as graphene and silicene, have attracted tremendous attention due to their unique physical and chemical properties. On the other hand, graphene is one of the allotropes of carbon that, together with fullerenes and carbon nanotubes, has determined was called the “carbon revolution”. One of the more important and promising carbon allotropes nowadays are the so-called “carbon nano-onions”, which are made of spherical or polyhedral concentric layers of carbon atoms arranged in a honeycomb net.

The purpose of this thesis was to synthesize and study Graphene, Silicene and Carbon Nano-Onions (CNO).

Graphene was obtained on a Ni(111) surface, and its plasmonic properties were studied by electron energy loss spectroscopy. Moreover, the structure of the carbon K-edge loss was measured and compared with theoretical results.

Silicene was synthesized on Ag(111) in different geometrical arrangements determined by LEED, and it has been shown that they have peculiar plasmonic properties. In particular, a Silicene layer made of a mix of three different phases seems to behave as a free-standing Silicene layer.

CNO were obtained by the underwater arc discharge technique. A new crystallization mechanism has been introduced to explain the formation of a conglomerate made almost exclusively of CNO which forms in the plasmatic zone.

1.1 Graphene

Graphene is a flat single layer of carbon atoms arranged in a honeycomb lattice with two crystallographically equivalent atoms (A and B) in its primitive unit cell [1–3] [Figure 2.2 a]. The sp^2 hybridization between one 2*s* orbital and two 2*p* orbitals leads to a trigonal planar structure with a formation of strong bonds between carbon atoms that are separated by 1.42 Å. The bonding orbitals have a filled shell and, hence, form deeper valence band levels. The $2p_z$ orbitals on the neighbouring carbon atoms are perpendicular to the planar structure of the graphene layer and can bind covalently, leading to the formation of a band.

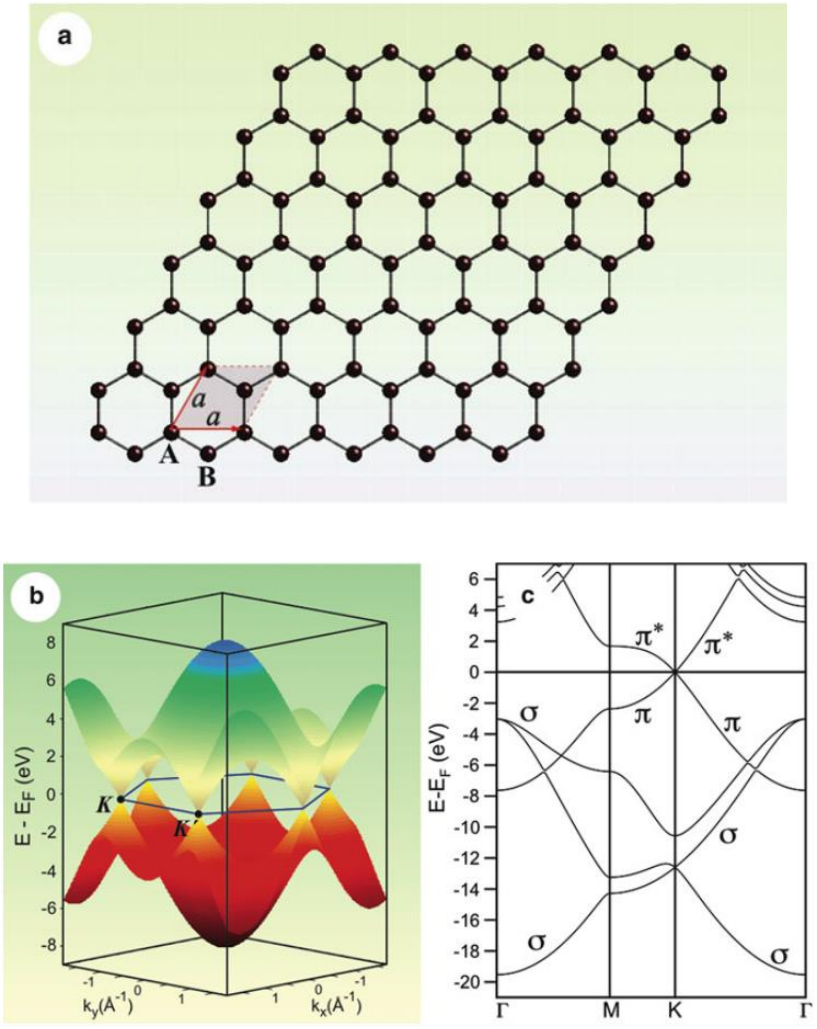

Figure 2.2: (**a**) Crystal structure of the graphene layer, where carbon atoms are arranged in a honeycomb lattice. The unit cell of graphene with lattice constant a has two carbon atoms per unit cell, A and B. (**b**) Electronic dispersion of π and π^* states in the honeycomb lattice of free-standing graphene. (**c**) Band structure of free-standing graphene (σ, π and π^* bands are marked).

The unique property of the electronic structure of graphene is that the π and π* bands touch at a single point at the Fermi energy (E_F) at the corner of graphene's hexagonal Brillouin zone, and close to this so-called Dirac point the bands display a linear dispersion and form Dirac cones [4] [Figure 2.2 b]. Thus, undoped graphene is a semimetal ("zerogap semiconductor"). The linear dispersion of the bands mimics the physics of quasi-particles with zero mass, the so-called massless Dirac fermions [1–3]. The fascinating electronic and transport properties of graphene [1–3] make it to a point of focus not only in fundamental research but also in applied science and technology with a vision to implement graphene in a myriad of electronic devices replacing the existing silicon technology.

However, a widespread implementation of graphene in electronics has been hampered by the two major difficulties: reliable production of high-quality samples, especially in a large-scale fashion and the "zero-gap" electronic structure of graphene, which leads to limitations for direct application of this material in possible electronic devices. As a response to the first challenge, a number of approaches for single layer graphene preparation have been tested, corroborating chemical vapor deposition (CVD) on transition-metal surfaces to be the most promising alternative to micromechanical cleavage for producing macroscopic graphene films. In 2008, mass-production of continuous graphene wafers by the CVD method on polycrystalline Ni or Cu surfaces and its transfer to arbitrary substrates was demonstrated [4–6]. The transferred graphene films show very low sheet resistance of 280 Ω per square, with 80% optical transparency, high electron mobility of 3,700 $cm^2V^{-1}s^{-1}$, and the half-integer quantum Hall effect at low temperatures, indicating that the quality of graphene grown by CVD is as high as that of mechanically cleaved graphene. Further modifications of this method within less than one year led to even more fascinating results, where graphene layers as large as 30 inches were transferred on to a polymer film for the preparation of transparent electrodes [9].

Despite the fascinating recent achievements in graphene production, the second problem of controllable doping should be solved prior to being able to implement graphene in any kind of electronic device. Several strategies exist, which allow the modification of the electronic structure of graphene, including (1) fabrication of narrow, straight-edged stripes of graphene, so-called nanoribbons [8,9], (2) preparation of bi-layer graphene [10,11], (3) direct chemical doping of graphene by an exchange of a small amount of carbon atoms by nitrogen [14], boron [15] or

transition-metal atoms [16]; (4) modification of the electronic structure of the graphene by interaction with substrates [15–19]; (5) intercalation of materials underneath graphene prepared on different substrates [20–25]; (6) deposition of different materials on top of graphene [26–28]. Not surprisingly, the investigation of graphene interaction with supporting or doping materials, which may provide an additional important degree of control of graphene properties, has become one of the most important research fields [29–32].

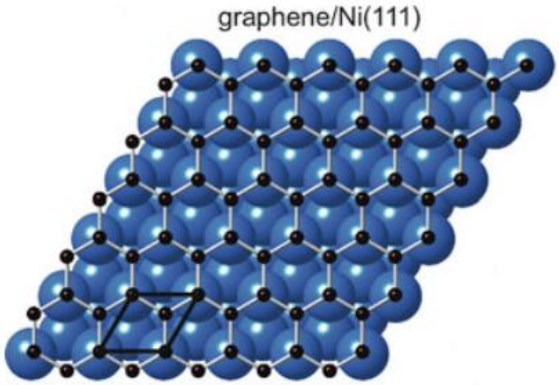

Figure 2.3: Top-view of a simple ball model for the top-*fcc* graphene/Ni(111) system is shown. Carbon atoms are *small black spheres* and nickel atoms are *big blue spheres*.

Two common methods of graphene preparation on metallic surfaces exist: (1) elevated temperature segregation of the carbon atoms to the surface of a bulk metallic sample, which was doped with carbon prior to the treatment [Figure 2.4 a] and (2) thermal decomposition of carbon-containing molecules on the surface of transition metals (TMs) [Figure 2.4 b]. In the first method, the transition-metal sample with some amount of carbon impurities or the bulk crystal previously loaded with carbon (via keeping the sample at elevated temperature in the atmosphere of CO or hydrocarbons) is annealed at higher temperatures. This procedure leads to the segregation of carbon atoms to the surface of the metal. Careful control of the temperature and the cooling rate of the sample allow varying the thicknesses of the grown graphene layer: monolayer versus multilayer growth.

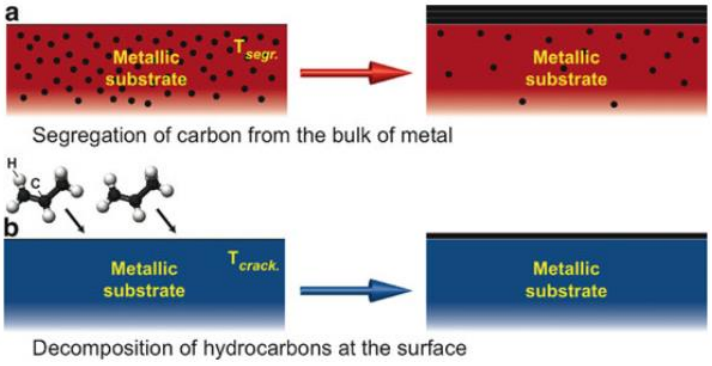

Figure 2.4: Two ways of the graphene preparation on metal surfaces: (**a**) Segregation of bulk-dissolved carbon atoms to the surface at high temperature T_{segr}; (**b**) Decomposition (cracking) of hydrocarbon molecules at the surface of transition metals at high temperature T_{crack}

The second method involves the thermal decomposition (cracking) of carbon-containing molecules at a metal surface. Light hydrocarbon molecules, such as ethylene or propene, are commonly used, but the successful decomposition of CO, acetylene, and of heavy hydrocarbon molecules, such as cyclohexane, n-heptane, benzene, and toluene, was also demonstrated [17]. Molecules can be adsorbed on a metal surface at room temperature, and then annealing of the sample leads to the decomposition of molecules and hydrogen desorption. Alternatively, the hot sample surface can be directly exposed to precursor molecules, which decompose at the sample surface. Recent experiments demonstrate that both methods, segregation and decomposition, lead to graphene layers of similar quality. In case of segregation, the kinetics of single graphene layer formation is defined by a careful control of the annealing temperature (but multilayers of graphene could also be prepared). In the second method, the graphene thickness is naturally restricted to a single-layer due to the fact that the chemical reaction on the catalytically active metallic surface takes the place. Thus, the speed of hydrocarbon decomposition drops down by several orders of magnitude as soon as the first graphene monolayer is formed [33,34].

1.2 Silicene

Silicene is a single atomic layer of silicon much like graphene [37]. Early work, both theoretical [2–6] and experimental [7,8] , went mostly unnoticed until silicene nanoribbons were reported to have been fabricated on a silver substrate [45]. Since then, silicene sheets have been grown mainly on Ag(111) [10–14]; these were achieved under ultrahigh vacuum conditions by evaporation of silicon wafer and slow deposition onto a substrate at 220–260 °C.

The interest in silicene is exactly the same as that for graphene, in being two-dimensional (2D) and possessing Dirac cones [51]. One advantage relies on its possible application in electronics, whereby its natural compatibility with the current Si technology might make fabrication a commercial reality. Indeed, a field-effect transistor made out of silicene has finally been demonstrated in 2015 [52].

Although theorists had speculated about the existence and possible properties of silicene, [15,17,18] researchers first observed silicon structures that were suggestive of silicene in 2010 [19,20]. Using a scanning tunneling microscope they studied self-assembled silicene nanoribbons and silicene sheets deposited onto a silver crystal, Ag(110) and Ag(111), with atomic resolution. The images revealed hexagons in a honeycomb structure similar to that of graphene which, however, were shown to originate from the silver surface mimicking the hexagons [57]. Density functional theory (DFT) calculations showed that silicon atoms tend to form such honeycomb structures on silver, and adopt a slight curvature that makes the graphene-like configuration more likely. This was followed by the discovery of dumbbell reconstruction in silicene [58] which explains the formation mechanisms of layered silicene [59] and silicene on Ag [60]. In 2015, a silicene field-effect transistor made its debut [61] that opens up new opportunities for two-dimensional silicon for various fundamental science studies and electronic applications [26,27].

Similarities with graphene come from the similar atoms of silicon and carbon. They lie next to each other in the same group on the periodic table and have an s^2 p^2 electronic structure. The 2D structures of silicene and graphene also are quite similar but have important differences [64]. While both form hexagonal structures, graphene is completely flat, while silicene forms buckled hexagonal layers. Its buckled structure gives silicene a tuneable band gap by applying an

external electric field. Silicene's hydrogenation reaction is more exothermic than graphene's. Another difference is that since silicon's covalent bonds do not have pi-stacking, silicene does not cluster into a graphite-like form [65].

Silicene and graphene have similar electronic structures. Both have a Dirac cone and linear electronic dispersion around the Γ point. Both also have a quantum spin Hall effect. Both are expected to have the characteristics of massless Dirac fermions that carry charge, but this is only predicted for silicene and has not been observed, likely because it is expected to only occur with free-standing silicene which has not been synthesized. It is believed that the substrate silicene is made on has a substantial effect on its electronic properties [65].

Unlike carbon atoms in graphene, silicon atoms tend to adopt sp^3 hybridization over sp^2 in silicene, which makes it highly chemically active on the surface and allows its electronic states to be easily tuned by chemical functionalization [66].

2D silicene is not fully planar, apparently featuring chair-like puckering distortions in the rings. This leads to ordered surface ripples. Hydrogenation of silicenes to silicanes is exothermic. This led to the prediction that the process of conversion of silicene to silicane (hydrogenated silicene) is a candidate for hydrogen storage. Unlike graphite, which consists of weakly held stacks of graphene layers through dispersion forces, interlayer coupling in silicenes is very strong. The buckling of the hexagonal structure of silicene is caused by pseudo-Jahn-Teller distortion (PJT). This is caused by strong vibronic coupling of unoccupied molecular orbitals and occupied molecular orbitals. These orbitals are close enough in energy to cause the distortion to high symmetry configurations of silicene. The buckled structure can be flattened by suppressing the PJT distortion by increasing the energy gap between the unoccupied molecular orbitals and occupied molecular orbitals. This can be done by adding lithium ions [65]. In addition to its potential compatibility with existing semiconductor techniques, silicene has the advantage that its edges do not exhibit oxygen reactivity [67].

In 2012 several groups independently reported ordered phases on the Ag(111) surface [11,13,14]. Results from scanning tunneling spectroscopy measurements [68] and from angle-resolved photoemission spectroscopy (ARPES) appeared to show that silicene would have

similar electronic properties as graphene, namely an electronic dispersion resembling that of relativistic Dirac fermions at the K points of the Brillouin zone, [50] but the interpretation was later disputed and shown to arise due to a substrate ban [33–39]. The *p-d* hybridisation mechanism between Ag and Si is important to stabilise the nearly flat silicon clusters and the effectiveness of Ag substrate for silicene growth explained by DFT calculations and molecular dynamics simulations [38,40]. The unique hybridized electronic structures of epitaxial 4×4 silicene on Ag(111) determines highly chemical reactivity of silicene surface, which are revealed by scanning tunneling microscopy and angle-resolved photoemission spectroscopy. The hybridization between Si and Ag results in a metallic surface state, which can gradually decay due to oxygen adsorption. X-ray photoemission spectroscopy confirms the decoupling of Si-Ag bonds after oxygen treatment as well as the relatively oxygen resistance of Ag(111) surface, in contrast to 4×4 silicene [with respect to Ag(111)] [74].

1.3 Carbon nano-onions (CNO)

Beginning with the discovery of fullerenes (1985) [77], moving to carbon nanotubes in (1991) [78], and then to graphene in (2004) [37], carbon nanomaterials have been widely studied and have shown to have a multitude of potential applications. However, another unique allotropic form of carbon, Carbon Nano Onions (CNOs) [3–9], which was actually discovered before these other materials, has long been overshadowed by these more popular and much more thoroughly investigated carbon nanomaterials.

CNOs consist of multilayered quasi-spherical and polyhedral shaped shells that represent another new nanophase of carbon material that owes its name to its concentric layered structures resembling that of an onion [80]. In the last several years, CNOs have attracted a great deal of attention because of their unique chemical and physical properties. These properties are different from those of other nano-sized carbon materials.

CNOs have been extensively studied to understand their underlying nature and to explore their potentiality for a wide variety of technological applications [81]. Although CNOs has been synthesized by many different methods in the last 30 years, large scale production has yet to be fully achieved.

Sumio Iijima first discovered CNOs while looking at a sample of carbon black in a transmission electron microscope (TEM) in 1980 [84]. The small amount of CNOs that were created in vacuum was observed as a byproduct of the synthesis of carbon black. From then until today the methods that have been developed to synthesize CNOs still remain in their infancy and suffer from issues relating to quality, quantity and purity. Various synthesis pathways have led to discoveries of CNOs with unique physical properties including varying shell numbers, graphitic structures, core types, and precursors.

Twelve years after the first discovery of the CNOs, Daniel Ugarte (1992) [79] is credited with developing a formation mechanism for the creation of spherical graphitic structures by focusing an electron beam on a sample of amorphous carbon. This process caused the carbon to graphitize and began to curl. After sufficient time, it closed on itself forming an onion like

structure. It is surmised that the curving and closure occurred in order to minimize the surface energy of the newly formed edge planes of graphite.

Because of its multitude of applications, it is of paramount importance to be able to synthesize this material economically in consistent size, high purity and large volume. According to the literature available, to date, the method that is the most utilized is the thermal transformation of nanodiamonds in vacuum [83]. According to published claims, the material can be made in sizeable volume using this method, as opposed to the very limited volume production of the other above mentioned processes. CNOs can also be produces by DC underwater arc discharge between graphite electrodes [83,84].

Recently, Bartelmess and Giordani published an extensive review on the development of carbon nano onions (CNOs) and the many pathways (over the years) that have been used to synthesize this material [87]. CNOs have even attracted the interest of NASA researchers for their tri-biological properties as additives for aerospace applications. Despite much interest in different carbon-based nanomaterials, CNOs as functional constructs for intracellular transport have not been widely explored. However, given their size, homogeneity and purity (compared with carbon nanotubes) they could in principle add an important new avenue for the transport of imaging and therapeutic agents. These carbon particles have demonstrated a higher cellular uptake, low cytotoxicity and lower inflammatory potential, than CNTs, thus creating a very promising future for their biomedical applications.”

CHAPTER TWO

EXPERIMENTAL METHODS

2.1 Ultra-High Vacuum (UHV) Chamber

UHV is a necessary condition for many surface analytic techniques to reduce surface contamination, by reducing the number of molecules reaching the sample over the time period necessary to perform investigation. Moreover, surface-sensitive spectroscopies utilize electron beams and analyzers that need ultra-high vacuum conditions. Typically, UHV requires high pumping speed, possibly multiple vacuum pumps in series and/or parallel.

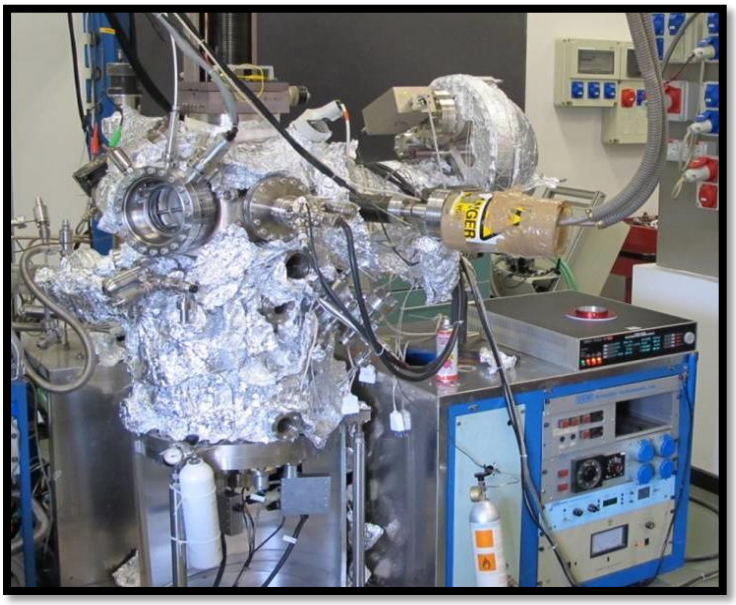

Figure 2.1: Ultra High Vacuum Chamber in Nanoscience Laboratory

The UHV chamber used in this work is divided into two communicant sections as we have in Figure 2.1. In the upper section we performed Electron Energy Loss Spectroscopy (EELS), Low Electron Energy Diffraction (LEED) and X-Ray Photoelectron Spectroscopy (XPS). For these purposes, the upper part is equipped with an electron gun, an X-Ray source (Al Kα, 1486.6 eV), an hemispherical electron energy analyzer that can collect the electrons emitted (or scattered) by the sample, and a Retarding Field Analyzer for LEED measurements. In the upper section are also present three gas-lines for the controlled release of gases in the analysis chamber, and an ion gun that generates a beam of argon ions.

The lower part of the UHV chamber contains an apparatus for High Resolution Electron Energy Loss Spectroscopy (HREELS) made of a fixed monochromator and a rotating analyzer, both 50 mm electrostatic hemispherical. The angular acceptance of the analyzer is 2°.

2.2 Low Energy Electron Diffraction (LEED)

LEED is a technique that allows to gain information about the long range order of atoms at the surface of a crystal through the diffraction of electrons with low energy. LEED permits the determination of the surface symmetry of single-crystalline materials by bombardment with low energy electrons and observation of diffracted electrons as spots on a fluorescent screen (Figure 2.2).

Figure 2.2: Picture of low energy electron difraction apparatus.

The LEED detector usually contains an electron gun, three or four hemispherical concentric grids (the Retarding Field Analyzer) and a phosphor screen. Electron gun can produce electrons with energy from 20 to 200 eV, the electrons are emitted by a cathode filament which is at a negative potential with respect to the sample. The electrons are accelerated and focused into a beam, with a typical width that extends from 0.1 to 0.5 mm. Some of the electrons incident on the sample surface are backscattered elastically, and diffraction can be detected when the sample has an ordered surface. The grids are used for screening out the inelastic scattered electrons (Figure 2.3); therefore the first grid screens the space above the sample from the

retarding field, the next grid is at a potential to block low energy electrons, it is called the suppressor and is a retarding field analyzer to block inelastically scattered electrons.

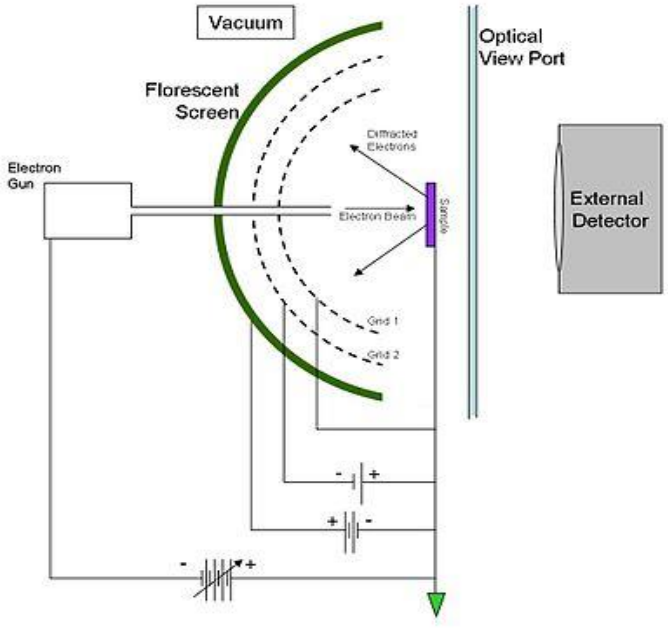

Figure 2.3: Diagram of Low Energy Electron Diffraction apparatus.

Only the elastically scattered electrons are accelerated and hit a fluorescent screen producing the projecting of the reciprocal lattice of the sample (diffraction LEED pattern).

The electron beam can be represented by a plane wave with a wavelength in accordance to the de Broglie hypothesis:

$$\lambda = \frac{h}{\sqrt{2mE}} \quad , \qquad \lambda\,[\text{nm}] \approx \sqrt{\frac{1.5}{E[eV]}}$$

The interaction between the scattering centers present in the surface and the incident electrons is most conveniently described in reciprocal space. In three dimensions the primitive reciprocal lattice vectors {**a*, b*, c***} are related to the real space lattice {**a, b, c**} in the following way:

$$\mathbf{a^*} = \frac{2\pi\,\mathbf{b}\times\mathbf{c}}{\mathbf{a}\cdot(\mathbf{b}\times\mathbf{c})} \qquad \mathbf{b^*} = \frac{2\pi\,\mathbf{c}\times\mathbf{a}}{\mathbf{b}\cdot(\mathbf{c}\times\mathbf{a})} \qquad \mathbf{c^*} = \frac{2\pi\,\mathbf{a}\times\mathbf{b}}{\mathbf{c}\cdot(\mathbf{a}\times\mathbf{b})}$$

For an incident electron with wave vector $k_0=2\pi/\lambda_0$ and scattered wave vector $k=2\pi/\lambda$, the condition for constructive interference and hence diffraction of scattered electron waves is given by the Laue condition:

$$\mathbf{k}-\mathbf{k}_0 = \mathbf{G}_{hkl},$$

where, (h,k,l) is a set of integers and $\mathbf{G}_{hkl}=h\mathbf{a}^*+k\mathbf{b}^*+l\mathbf{c}^*$ is a vector of the reciprocal lattice (Figure 2.4). The magnitudes of the wave vectors are unchanged, i.e. $|\mathbf{k}_0| = |\mathbf{k}|$, since only elastic scattering is considered. Since the mean free path of low energy electrons in the matter is only a few angstroms, only the first few atomic layers contribute to the diffraction. This means that there are no diffraction conditions in the direction perpendicular to the sample surface. As a consequence the reciprocal lattice of a surface is a 2D lattice with rods extending perpendicular from each lattice point.

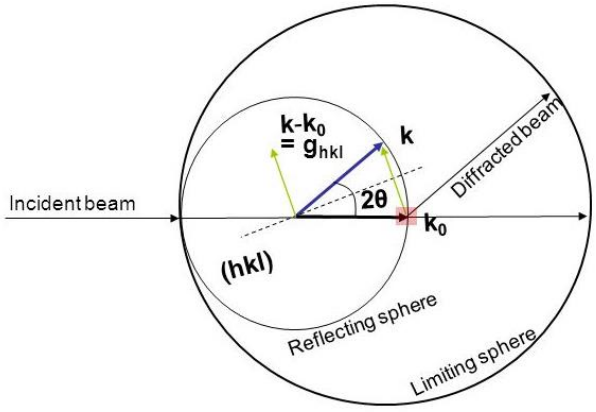

Figure 2.4: Ewald's sphere construction for the case of diffraction from a 2D-lattice.

2.3 X-ray Photoelectron Spectroscopy (XPS)

The main component of a XPS system include a source of X-rays, based on the fluorescent emission of photons from a magnesium or aluminum slab caused by high energetic electrons emitted by a filament and accelerated towards the anode by a voltage of the order of some KeV. Non-monochromatic magnesium X-rays have a wavelength of 9.89 angstroms which corresponds to a photon energy of 1253 eV. The energy width of the non-monochromatic X-ray

is roughly 0.70 eV, which is the ultimate energy resolution of a system using non monochromatic X-rays.

The mean free path of electrons in solids is very small, the detected electrons originate from only the top few atomic layers, making XPS a surface-sensitive technique for chemical analysis. Quantitative data can be obtained from peak heights or peak areas and identification of chemical states often can be made from exact measurements of peak positions and separations. Each element has a unique set of binding energies, XPS can be used to identify and determine the concentration of the elements in the surface. Variations in the elemental binding energies (chemical shifts) arise from differences in the chemical potential and polarizability of compounds. These chemical shifts can be used to identify the chemical state of the materials being analyzed.

A schematic figure about an experimental setup of photoelectron spectroscopy can be seen in Figure 2.5 below consisting of 3 main parts: X-ray source**,** UHV vacuum system and detection & analyzer system.

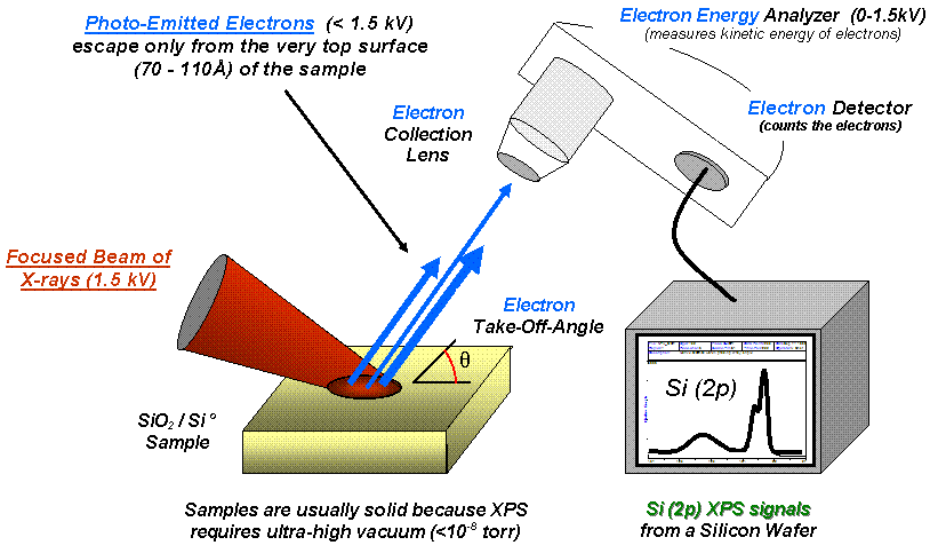

Figure 2.5: Schematic figure of an XPS system.

In XPS we are concerned with a special form of photoemission, i.e., the ejection of an electron from a core level by an X-ray photon of energy *hv*. The energy of the emitted

photoelectrons is then analysed by the electron spectrometer and the data presented as a graph of intensity versus electron energy – the X-ray induced photoelectron spectrum.

The kinetic energy (E_K) of the electron is the experimental quantity measured by the spectrometer, but this is dependent on the photon energy of the X-rays employed and is therefore not an intrinsic material property. The binding energy of the electron (E_B) is the parameter which identifies the electron specifically, both in terms of its parent element and atomic energy level. The relationship between the parameters involved in the XPS experiment is:

$$E_B = h\nu - E_K - W$$

where hν is the photon energy, E_K is the kinetic energy of the electron, and W is the spectrometer work function. As all three quantities on the right-hand side of the equation are known or measurable, it is a simple matter to calculate the binding energy of the electron. In practice, this task will be performed by the control electronics or data system associated with the spectrometer and the operator merely selects a binding or kinetic energy scale whichever is considered the more appropriate. [88]

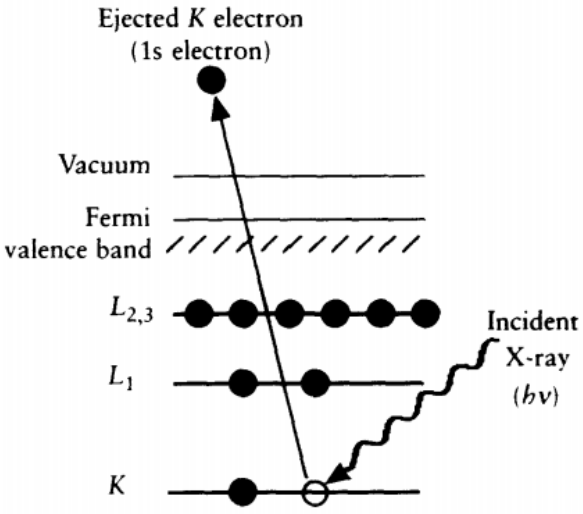

Figure 2.6: Schematic diagram of the XPS process, showing photoionization of an atom by the ejection of a 1s electron

The process of photoemission is shown schematically in Figure 2.6, where an electron from the K shell is ejected from the atom (a 1s photoelectron). The photoelectron spectrum will reproduce the electronic structure of an element quite accurately since all electrons with a binding energy less than the photon energy will feature in the spectrum.

2.4 Electron Energy Loss Spectroscopy (EELS)

EELS is one of the most common surface analysis techniques used to investigate the excitations in a crystal, caused by an incident electrons beam called primary beam, by analyzing the energy spectrum of electrons backscattered from it. An electron passing through material can interact with electron clouds of the atoms present and transfer some of its kinetic energy to them. There are two modes of operating for EELS:

1. Electron Energy Loss Spectroscopy in transmission mode.
2. Electron Energy Loss Spectroscopy in reflection mode.

EELS in transmission mode uses electrons at energies of the order on tenths of keV. At those high energies, the incident electrons beam passes through a thin foil of the material of interest and the transmitted one contains inelastically scattered electrons whose energy has been decreased by amounts corresponding to characteristic absorption energies in the solid. At lower primary energies, (from few to hundreds of eV) the Electron Energy Loss Spectroscopy is used in the reflection mode, in this approach the reflected beam is monitored for the electronic excitations occurred in the surface. Bulk and surface plasmons are the principal features of these spectra.

High Resolution EELS employs a monochromatic incident electron beam of quite low energy (a few eV). The primary focus of this technique is the study of vibrational structure of the surface and especially of adsorbents on that surface.

The energy of the primary beam has fundamental importance to understand how deep the sample is probed, in fact Figure 2.7 represents the mean free path (counted in monolayers) versus the energy of the incident electron beam.

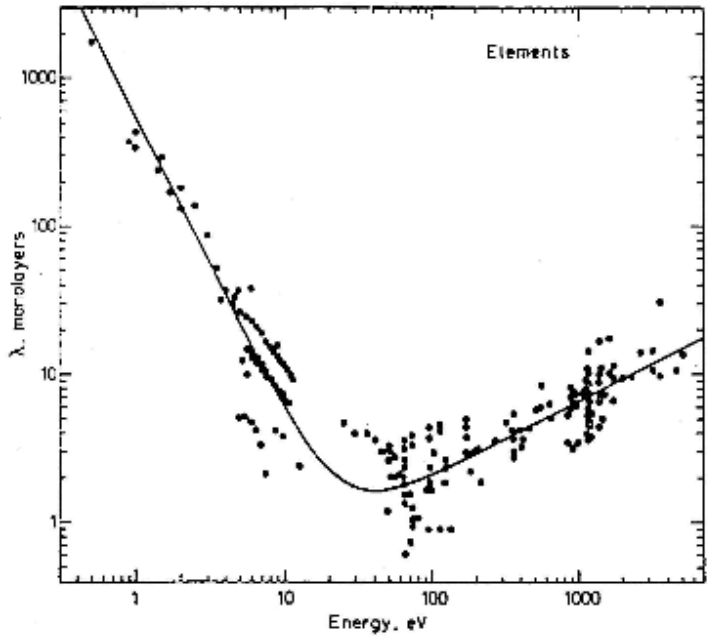

Figure 2.7: Electrons mean free path as function of their energies.

The mean free path, that is the mean distance covered by an electron in a medium before to undergo an inelastic collision, shows a minimum around 50 eV, and after this minimum, increasing primary energy implies the increasing of the mean free path. This graph is universal, it means that it's a good estimate of electrons mean free path in all medium, and also shows that for probe more than 10 monolayers (10-20 Å) of materials it's necessary to use electrons of more than 1000 eV of energy; therefore, all our measurements, carried out at a primary energy of about 100 eV, characterized mainly the surface properties of the sample. Similarly, also measurements obtained by X-Ray excitation source are surface sensitive, in fact, as assumed above, *although the photons* can penetrate more and more than the electron probe, the analyzer scans only the electrons coming from the outer layers very near to the surface of the sample.

In electron energy-loss spectroscopy, we deal directly with the primary process of electron excitation, which results in the fast electron losing a characteristic amount of energy. The electron beam scattered by the sample is directed into a high-resolution electron spectrometer that separates the electrons according to their kinetic energy and produces an electron energy-loss spectrum showing the number of electrons (scattered intensity) as a function of their decrease in kinetic energy.

The scattered electrons have principally the same energy of the incident electron beam (elastic peak) and only few electrons are emitted with lower energy respect to the primary energy. These latter are inelastic electrons and the energy they lost (E_{loss}) is the same energy that the crystal absorbed to produce an excitation.

The sample excitations induced by an electronic perturbation, are mainly divided into three groups, each for a specific energy range:

1. Core electron excitations (E_{loss} of the order of hundreds of eV)
2. Valence band excitations (single particle interband or intraband transitions), surface and bulk collective excitations (plasmons) (E_{loss} of the order of tens of eV).
3. Vibrational excitations of the sample (acoustic and optic phonon) and vibrational excitations of atoms or molecules adsorbed on the surface (E_{loss} of the order of meV).

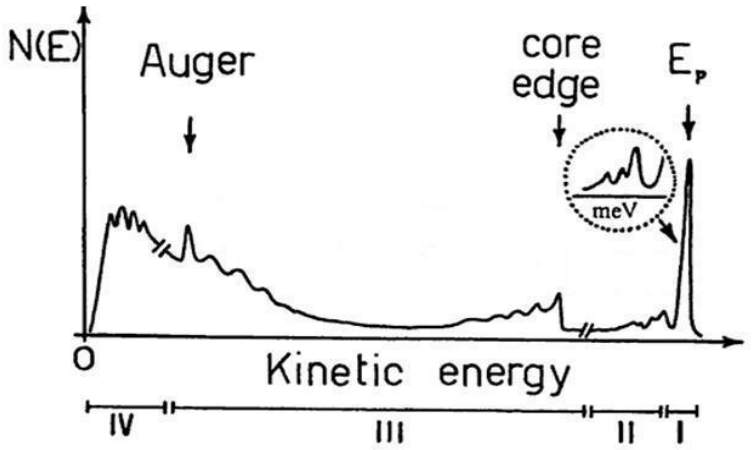

Figure 2.8: Energy of the electrons emitted after the interaction with a beam of primary electrons of energy *E*p.

In Figure 2.8 is plotted the typical energy distribution *N(E)* of the electrons emitted by the crystal after the interaction with a beam of primary electrons of energy E_p. The previous figure can be divided in four sections, each of which represents different ranges of E_{loss} with different sample information:

The region **I** includes the highest peak of the energy distribution with energy E_p that is the elastic peak and allows finding information about the structure of the sample. It contains all electrons that have suffered an elastic interaction only. The peaks close to the elastic peak

(within about 1 eV) allow to gain information about the vibrational modes of the crystal (phonons) and the vibrational excitations of atoms and molecules adsorbed on the surface.

In the second region (**II)** it is possible to distinguish all the electrons that had inelastic interaction with the solid. The EELS spectroscopy is used, in this energy range, to have information about surface and bulk collective excitations and therefore about its dielectric function. Here, the plasmon peaks are the predominant features.

The third region (**III**) contains electrons which suffered higher energy losses and secondary electrons at high energy. Ionization edges appear at electron energy losses that are typical for a specific element and thus qualitative analysis of a material is possible by EELS. The onset of such an ionization edge corresponds to the threshold energy that is necessary to promote an inner shell electron from its energetically favored ground state to the lowest unoccupied level. This energy is specific for a certain shell and for a certain element. Above this threshold energy, all energy losses are possible since an electron transferred to the vacuum might carry any amount of additional energy. If the atom has a well-structured density of states (DOS) around the Fermi level, not all transitions are equally likely. This gives rise to a fine structure of the area close to the edge that reflects the DOS and gives information about the bonding state. This method is called electron energy loss near edge structure (ELNES). From a careful evaluation of the fine structure farther away from the edge, until hundreds eV above the core excitations, information about coordination and interatomic distances are obtainable (extended energy loss fine structure, EXELFS).

In the last region (**IV**) is an high and wide peak caused by the secondary electrons, also this peak has a fine structure that can be analyzed by the angle-resolved Secondary Electron Emission (SEE). This analysis provides information about the density and the dispersion of empty states just above the Fermi level.

There are several basic flavors of EELS, primarily classified by the geometry and by the kinetic energy of the incident electrons. Probably the most common today is transmission EELS, in which the kinetic energies are typically 100 to 300 keV and the incident electrons pass entirely through the material sample. Usually this occurs in a transmission electron microscope (TEM),

although some dedicated systems exist which enable extreme resolution in terms of energy and momentum transfer at the expense of spatial resolution.

Instead, the reflection geometry is particularly sensitive to surface properties but is limited to very small energy losses such as those associated with surface plasmons or direct interband transitions. Lucas and Sunjc [89] made the first publications about this, followed by Evans e Mills [2– 4].

The EELS spectroscopy has several analogies with optic absorption, in fact both techniques give information about the density of electronic bands in the examined solid. EELS, however, makes it possible to change easily the energy of the incident beam, in order to probe a larger energy range. Furthermore, the low mean free path of electrons in the reflection geometry makes this technique more sensible to the surface proprieties with respect to optical spectroscopy.

2.4.1 Theoretical Fundaments

In a continuous and homogeneous medium, the response to an electric external perturbation can be described by the dielectric theory. When an electron approaches a dielectric material, the electron density inside the solid changes to shield the long range electric field produced by the incoming perturbation. The density fluctuations generated inside the medium are related to the wave vector and the frequency of the external field, so the transferred energy depends on the field density energy variation inside the solid.

An electron inside the solid can acquire energy $\hbar\omega$ and impulse $\hbar\boldsymbol{q}$, because of inelastic interaction with an incident electron, if it lost the same amount of energy $\Delta E = \hbar\omega$.

The incident electron can be described by the electronic distribution:

$$\rho(\boldsymbol{r}, t) = -e\,\delta(\boldsymbol{r} - \boldsymbol{v}t)$$

The interaction potential produced inside the solid, follows the Poisson equation:

$$\varepsilon(\boldsymbol{q}, \omega)\nabla^2\varphi(\boldsymbol{r}, t) = -4\pi\,\delta(\boldsymbol{r} - \boldsymbol{v}t)$$

If we pass in the Fourier space, the transform function of $\varphi(\boldsymbol{r}, t)$ is:

$$\varphi(\boldsymbol{q},\omega) = \frac{8\pi^2 e}{q^2 \varepsilon(\boldsymbol{q},\omega)}$$

The energy loss of the electron in length unit inside the medium is $E_x|_{r=vt}$, where E_x is the component of the electric field along the x axis, perpendicular to the surface. Whereas

$$E(\boldsymbol{r},t) = -\nabla\varphi(\boldsymbol{r},t) = -i \int \boldsymbol{q}\, dq \int d\omega\ \varphi(\boldsymbol{q},\omega)\, e^{i(\boldsymbol{q}\cdot\boldsymbol{r}-\omega t)}$$

Replacing in this equation, the expression found for $\varphi(\boldsymbol{r},t)$ we obtain the loss energy probability in length unit as function of the exchanged moment $\boldsymbol{q}$ and of the frequency ω:

where $-Im\left[\frac{1}{\varepsilon(\boldsymbol{q},\omega)}\right] = \frac{\varepsilon_2}{{\varepsilon_1}^2+{\varepsilon_2}^2}$ is the bulk loss function.

So the bulk loss function describes the inelastic interaction of high energy electrons that pass through the sample.

A maximum in the loss function occurs when $\varepsilon_1 = 0$ and $\varepsilon_2 \approx 0$. One can see that the condition under which $\varepsilon_1 = 0$ corresponds to the excitation of a plasma wave in the medium.

The most used models to describe a solid material are the Drude and Lorentz models [93]. The first one deals the conduction electrons as a free electrons gas not subject to atomic potential, and in this case the dielectric function, in the limit of $q \to 0$, is:

$$\varepsilon(\omega) = 1 - \frac{{\omega_p}^2}{\omega^2 + i(\omega/\tau)}$$

where ω_p is the plasma frequency (${\omega_p}^2 = \frac{4\pi n e^2}{m_e}$) and τ is the relaxing time that takes into account the interactions between the electrons.

In the following figure is represented the real and the imaginary part of ε and $-Im[1/\varepsilon]$.

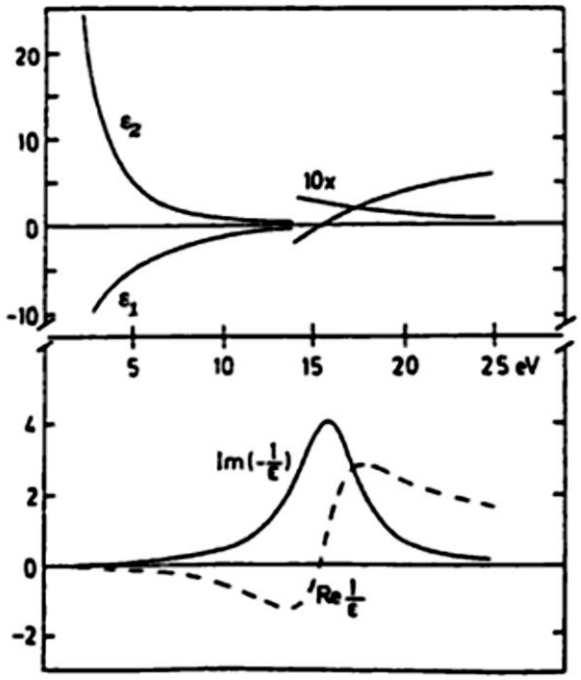

Figure 2.9: Real and imaginary part of the dielectric function ε (upper side) and real and imaginary part of 1/ ε (bottom side) for the Drude model.

The imaginary part of the dielectric function (Figure 2.9), ε_2 is monotonically decreasing and does not exhibit any structure, so a free electron gas does not generate any optical absorption. The loss function, instead, exhibits a maximum at the plasma frequency ω_p, corresponding to the excitation energy of a bulk plasmon in a free electron gas (from several eV to few tens of eV).

Lorentz model is based on treating electrons as damped harmonically bound particles subject to external electric fields. This model describes successfully bound electrons in a solid interacting with an electric field **E** and affected by an elastic-like restoring force with a own resonance frequency ω_0. Furthermore, to adapt, this ideal model to the experimental reality, the existence of a viscous term Γ is assumed that can explain the linewidths experimentally observed and avoid annoying divergences. The real materials have different resonances with different intensities, so it is associated at the resonance frequency ω_0, an empirical parameter f_0 called oscillator strength factor through which it possible to weigh the different intensities, so it satisfies the relation:

$$\sum_i f_i = 1$$

To obtain the Lorentz oscillator relation, in the single resonance frequency ω_0 case, we start from the second law of dynamics:

$$m(\ddot{\boldsymbol{x}} + \Gamma\dot{\boldsymbol{x}} + {\omega_0}^2\boldsymbol{x}) = e\boldsymbol{E}$$

Where m is the electron mass, e is the electron charge and E is the electron external field applied to the material. Solving the equation for $\boldsymbol{x}$ and replacing the external field by $\boldsymbol{E} = \boldsymbol{E_0}e^{-i\omega t}$, it is obtained:

$$\boldsymbol{x} = \frac{\left(e\boldsymbol{E_0}/m\right)e^{-i\omega t}}{{\omega_0}^2 - \omega^2 - i\omega\Gamma}$$

Using the equations for the microscopic dipole $\boldsymbol{p} = e\boldsymbol{x}$ and for macroscopic polarization $\boldsymbol{P} = n\boldsymbol{p}f_0$ it is extracted:

$$\boldsymbol{P} = \frac{\left(ne^2/m\right)f_0\boldsymbol{E_0}e^{-i\omega t}}{{\omega_0}^2 - \omega^2 - i\omega\Gamma}$$

Knowing that polarization and electric field are related through the equation $\boldsymbol{P} = \varepsilon_0(\varepsilon - 1)\boldsymbol{E}$ the dielectric function, for just one type of transition $\hbar\omega_0$ is

$$\varepsilon(\omega) = 1 + \frac{f_0{\omega_p}^2}{{\omega_0}^2 - \omega^2 - i\omega\Gamma}$$

where $\omega_p = \sqrt{\frac{ne^2}{m\varepsilon_0}}$ is the plasma frequency and f_0 is the oscillator strength factor. So for different resonances the real and imaginary part of the dielectric function, respectively ε_1 and ε_2, are:

$$\varepsilon_1(\omega) = 1 + {\omega_p}^2 \sum_i \frac{f_i({\omega_i}^2 - \omega^2)}{({\omega_i}^2 - \omega^2)^2 + \omega^2 {\Gamma_i}^2}$$

$$\varepsilon_2(\omega) = {\omega_p}^2 \omega \sum_i \frac{f_i \Gamma_i}{({\omega_i}^2 - \omega^2)^2 + \omega^2 {\Gamma_i}^2}$$

Generally this is a good approximation for semiconductor, insulators and for all metals which possess bound electrons (*d* or *p* valence electrons).

The following figure reports ε_1, ε_2, $-Im\left[1/\varepsilon\right]$ and $Re\left[1/\varepsilon\right]$ calculated for the Lorentz model

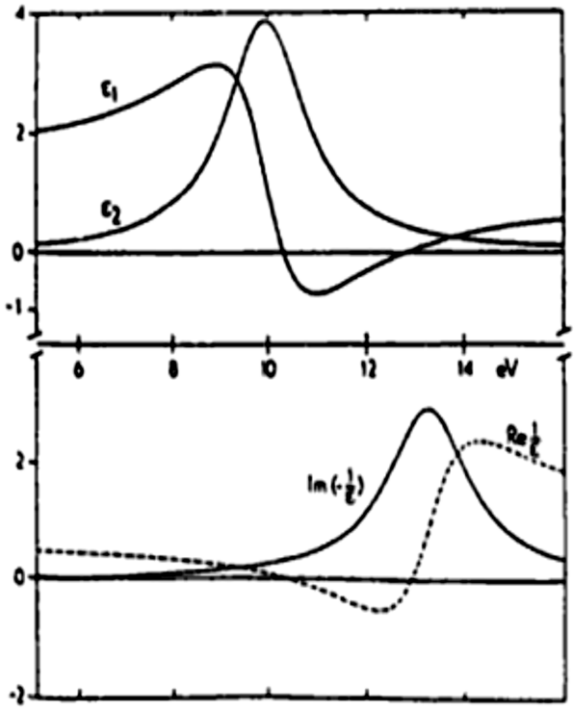

Figure 2.10: Real and imaginary part of the dielectric function ε (upper side) and real and imaginary part of 1/ ε (bottom side) for the Lorentz model.

In Figure 2.10 , the peak in ε_2 function represents an optical absorption at $\hbar\omega_0$, while the loss function exhibits a maximum at a frequency $\omega > \omega_0$ where $\varepsilon_1 = 0$ and $\varepsilon_2 \approx 0$. The occurrence of these conditions corresponds to a collective excitation in the solid known as "interband plasmon" in analogy to the free electron model.

More generally the behavior of metals is described by a dielectric function that is the sum of the intraband type (Drude model) and the interband type (Lorentz model). So the dielectric function is described by:

$$\varepsilon_1{}^{tot}(\omega) = \varepsilon_1{}^{free}(\omega) + \varepsilon_1{}^{bound}(\omega)$$

$$\varepsilon_2{}^{tot}(\omega) = \varepsilon_2{}^{free}(\omega) + \varepsilon_2{}^{bound}(\omega)$$

Observing trends of ε_2 and $-Im[1/\varepsilon]$ for metals and semiconductors, it's clear that the maximum of these two function are never in the same energy position, on the contrary we can assume that the maximum of ε_2 matches with the minimum of $-Im[1/\varepsilon]$, like if

$$-Im[1/\varepsilon] \sim 1/\varepsilon_2.$$

In conclusion this is the evidence that the single particle excitations and the collective excitations are generally in competition, making the EEL probability, in the range of 1-20 eV, inversely proportional to the optical absorption.

2.4.2 EELS in reflection geometry

The schematic representation of the EELS in reflection geometry is shown in the following Figure 2.11.

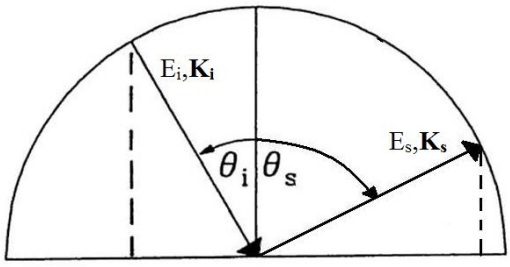

Figure 2.11: EELS reflection geometry representation

We assume that an electron with energy E_i and wave vector $\boldsymbol{K_i}$ hits the sample at an angle of incidence θ_i with respect to the surface normal and it scatters off the crystal with energy E_s and wave vector $\boldsymbol{K_s}$ at an angle θ_s.

We are describing an inelastic process, so the incident electron can transfer energy (E_{Loss}) and momentum ($\boldsymbol{q}$) to the sample. From the conservation rule of energy we know that:

$$E_i = E_s + E_{Loss}$$

The conservation of the component parallel to the surface of the momentum is more restrictive, in fact just the component parallel to the surface must be preserved. So, we have:

$$\boldsymbol{K_{i\backslash\backslash}} = \boldsymbol{K_{s\backslash\backslash}} + \boldsymbol{q}_{\backslash\backslash}$$

Therefore, the component parallel to the surface of the momentum transfer is calculated as:

$$\left|\boldsymbol{q}_{\backslash\backslash}\right| = |\boldsymbol{K_i}| \sin\theta_i - |\boldsymbol{K_s}| \sin\theta_s$$

Taking into account the relation between the energy and the momentum for a free electron $E = \frac{\hbar K^2}{2m}$ we can calculate $\left|\boldsymbol{q}_{\backslash\backslash}\right|$:

$$\left|\boldsymbol{q}_{\backslash\backslash}\right| = \sqrt{\frac{2m}{\hbar}}\left(\sqrt{E_i}\sin\theta_i - \sqrt{E_i - E_{Loss}}\sin\theta_s\right)$$

Thus, using monochromatic electron beam with a rotating analyzer it is possible, for each loss energy, calculate the component parallel to the surface of the momentum transfer obtaining the energy dispersion curve of the observed loss $\omega(\boldsymbol{q}_{\backslash\backslash})$.

2.5 Raman Spectroscopy

Raman spectroscopy is a spectroscopic technique based on inelastic scattering of monochromatic light, usually from a laser source (Figure 2.12.a). Inelastic scattering means that the frequency of photons in monochromatic light changes upon interaction with a sample. Photons of the laser light are absorbed by the sample and then reemitted. The frequency of part of the reemitted photons is shifted up or down with respect to the original monochromatic

frequency, which is called the Raman effect. This shift provides information about vibrational, rotational and other low frequency transitions in molecules.

The Raman effect is based on molecular deformations in an electric field E determined by the molecular polarizability α. The laser beam can be considered as an oscillating electromagnetic wave with electrical vector E. Upon interaction with the sample it induces an electric dipole moment $P = \alpha E$ which deforms molecules. Because of periodical deformation, molecules start vibrating with a characteristic frequency υ_m.

In other words, monochromatic laser light with frequency υ_0 excites molecules and transforms them into oscillating dipoles. Such oscillating dipoles emit light of three different frequencies when: 1) a molecule with no Raman-active modes absorbs a photon with the frequency υ_0, the excited molecule returns back to the same basic vibrational state and emits light with the same frequency υ_0 as an excitation source. This type of interaction is called an elastic Rayleigh scattering; 2) a photon with frequency υ_0 is absorbed by a Raman-active molecule in its basic vibrational state. Part of the photon's energy is transferred to the Raman-active mode with frequency υ_m and the resulting frequency of scattered light is reduced to $\upsilon_0 - \upsilon_m$. This Raman frequency is called Stokes frequency, or just Stokes; 3) a photon with frequency υ_0 is absorbed by a Raman-active molecule, which, at the time of interaction, is already in an excited vibrational state. Part of the energy of the excited Raman-active mode is released, the molecule goes to a lower vibrational state and the resulting frequency of scattered light goes up to $\upsilon_0 + \upsilon_m$. This Raman frequency is called Anti-Stokes frequency, or just AntiStokes. A sketch of the Raman effect is shown in Figure 2.12.b [94]. A typical Raman spectrum (Figure 2.12.c) will then show the measured shift in the frequency of the reemitted light with respect to the exciting radiation and will have a strong peak around 0 cm^{-1} (unless a filter is used to block this signal). The Stokes and anti-Stokes band will appear at symmetric positions of either side of 0. Normally Stokes bands are stronger than anti-Stokes, depending on the sample temperature and on the energy spacing of the vibrational levels (anti-Stokes band should not appear at 0 K).

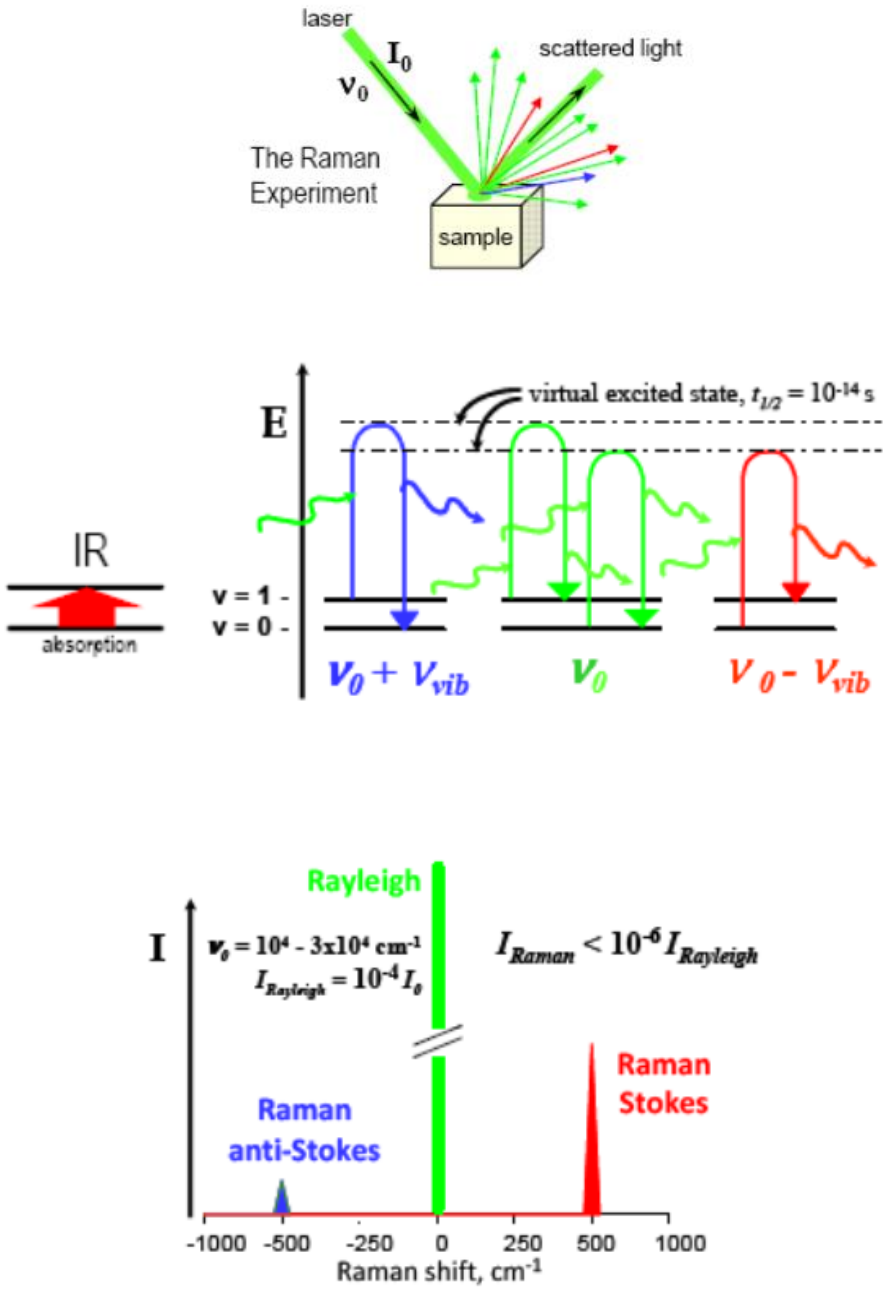

Figure 2.12: Raman spectroscopy:(a) laser-sample interaction; (b) Raman effect; (c) Raman spectrum

About 99.999% of all incident photons in spontaneous Raman undergo elastic Rayleigh scattering. This type of signal is useless for practical purposes of molecular characterization. Only about 10^{-4} % of the incident light produces inelastic Raman signal with frequencies $\upsilon_0 \pm \upsilon_m$ [94].

Raman spectroscopy is a very important analysis technique in the field of carbon research and has historically played an important role in the structural characterization of graphitic materials [95]. In fact, this spectroscopy technique allows to distinguish clearly between single and multilayer graphene thanks to the fact that Graphene vibrational properties depend on thickness of the flakes and this is reflected in the characteristic spectral features [96]. Figure 2.13 shows a Raman spectrum of monolayer graphene with respect to the Raman spectrum of graphite.

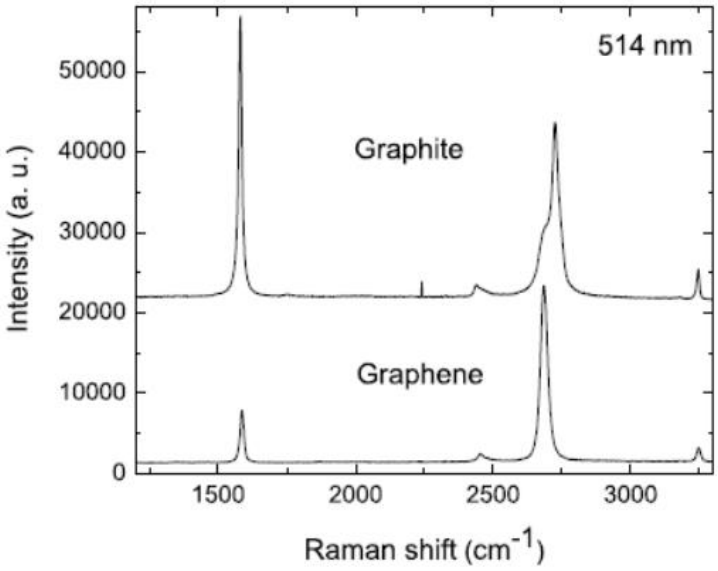

Figure 2.13: Raman spectra of graphite (top) and graphene (bottom) [97].

Graphene has two fundamental hallmarks: a first peak at around 1580 cm-1 named the G peak, and a second band around 2700 cm-1 called the G' or 2D peak. The shape of the 2D peak, in monolayer graphene, is sharp, narrow and centered at 2700 cm-1. This peak broadens in thicker flakes, as already in bilayers is the resulting envelop of four subpeaks (Figure 2.14) [15]. The position of the G peak shifts towards lower frequencies and its intensity increases significantly as the thickness grows. In graphene the G peak is smaller than the 2D while, already for bilayers and thicker flakes, the G peak is prominent.

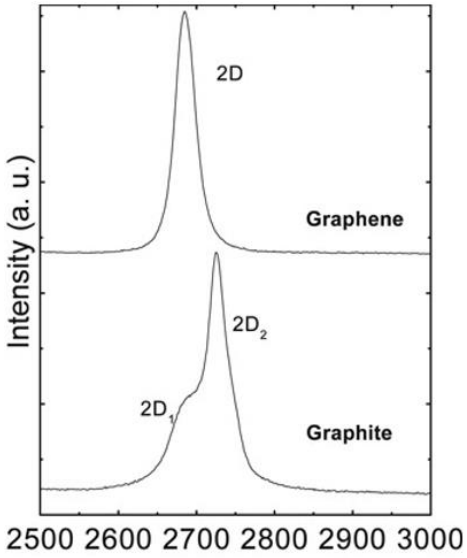

Figure 2.14: Evolution of the 2D peak from monolayer graphene to bulk graphite. The 2D peak's shape changes with respect to the thickness of the sample [97].

2.6 Transmission Electron Microscopy (TEM)

The transmission electron microscope is a very powerful tool for material science. A high energy beam of electrons is shone through a very thin sample, and the interactions between the electrons and the atoms can be used to observe features such as the crystal structure and features in the structure like dislocations and grain boundaries. TEM can be used to study the growth of layers, their composition and defects in semiconductors. High resolution can be used to analyze the quality, shape, size and density of quantum wells, wires and dots.

The TEM operates on the same basic principles as the light microscope but uses electrons instead of light. Because the wavelength of electrons is much smaller than that of light, the optimal resolution attainable for TEM images is many orders of magnitude better than that from a light microscope. Thus, TEMs can reveal the finest details of internal structure - in some cases as small as individual atoms. [98]

2.6.1 Fundamental Theory of TEM

2.6.1.1 The Concept of Resolution

The smallest distance between two points that we can resolve by our eyes is about 0.1-0.2 mm, depending on how good our eyes are. This distance is the resolution or resolving power of our eyes. The instrument that can show us pictures revealing detail finer than 0.1 mm could be described as a microscope.

The Rayleigh criterion defines the resolution of light microscope as:

$$\delta = \frac{0.61\,\lambda}{\mu\, sin\beta},$$

where λ is the wavelength of the radiation, μ is the refractive index of the view medium and β is the semi-angle of collection of the magnifying lens. The variable of refractive index and semi-angle is small, thus the resolution of light microscope is mainly decided by the wavelength of the radiation source. Taking green light as an example, its 550 nm wavelength gives 300 nm resolution, which is not high enough to separate two nearby atoms in solid-state materials. In facthe distance between two atoms in solid is around 0.2nm.

Based on wave-particle duality, we know that electron has some wave-like properties:

$$\lambda = \frac{h}{p}$$

If an electron is accelerated by an electrostatic potential drop eU, the electron wavelength can be described as:

$$\lambda = \frac{h}{\sqrt{2m_{\circ}eU\left(1 + \frac{eU}{2m_{\circ}c^2}\right)}}$$

If we take the potential as 100keV, the wavelength is 0.0037nm. The resolution of electron microscope should be better than that of light microscope.

2.6.1.2 The Instrument of Transmission Electron Microscope

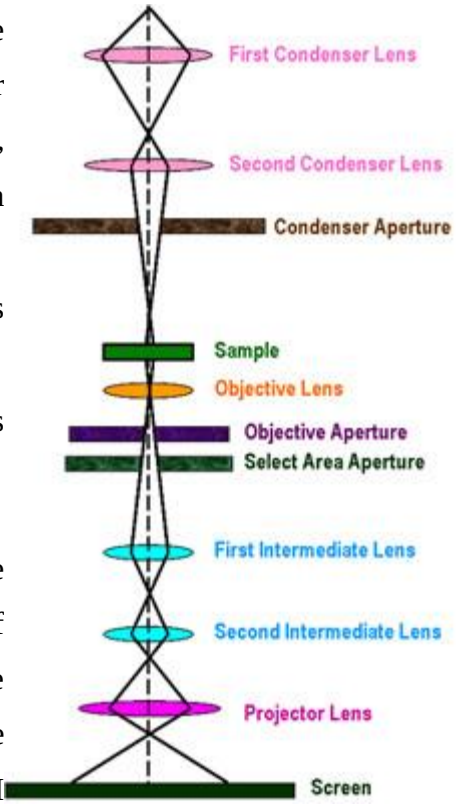

- Illumination system. It takes the electrons from the gun and transfers them to the specimen giving either a broad beam or a focused beam. In the ray-diagram, the parts above the specimen belong to illumination system.
- The objective lens and stage. This combination is the heart of TEM.
- The TEM imaging system. Physically, it includes the intermediate lens and projector lens.

The diffraction pattern and image are formed at the back focus plane and image plane of the objective lens. If we take the back focus plane as the objective plane of the intermediate lens and projector lens, we will obtain the diffraction pattern on the screen. It is said that the TEM works in diffraction mode. If we take the image plane of the objective lens as the objective plane of the intermediate lens and projector lens, we will form image on the screen. It is the image mode.

2.6.1.3 The Interaction between Electrons and Specimen

Because the average distance between two successive incident electrons is around 0.15mm (taking 100keV as the accelerate potential), which is far great than the TEM specimen thickness (~100-500 nm), we can consider the interaction between electrons and specimen as single electron scattering event. From the wave-particle duality point of view, the incident electron can be expressed as a plane wave $\Psi(r) = e^{2\pi i k_0 r}$. Resolving the Schrödinger equation, we can get the departure electron wave function as:

$$\Psi(r) = \Psi_0(r) + \frac{me}{2\pi\hbar^2}\int dr' \frac{e^{2\pi i k|r-r'|}}{|r-r'|} V(r')\,\Psi(r')$$

Taking Mutt approximation:

$$\Psi(r) = e^{2\pi i k_0 r} + \frac{me}{2\pi\hbar^2}\frac{e^{2\pi i k r}}{r}\int dr' e^{-2\pi i(k-k_0)}V(r')$$

the amplitude of the scattering beam is the Fourier transform of the specimen's potential.

If we considering perfect crystal, its potential can be described as:

$$V(r) = \sum_n \sum_r V_\alpha(r - R_n - r_\alpha)S_p(r)$$

$S_p(r)$ is the shape factor of crystal.

The Fourier transform of the potential is:

$$\Phi(u) = \sum_g \delta(u-g)V_g$$

where V_g is the structural factor and

$$V_g = \sum_\alpha e^{-2\pi i g r} f_\alpha(g)$$

The diffraction intensity can be calculated as:

$$|\Phi(u)|^2 = \left|\{\sum_g \delta(u-g)V_g\} \otimes S_p(u)\right|^2$$

2.6.1.4 Diffraction Contrast

There are two basic modes of TEM operation, namely the bright-field mode, where the (000) transmitted beam contributes to the image, and the dark-field imaging mode, in which the (000) beam is excluded. The size of the objective aperture in bright-field mode directly determines the information to be emphasized in the final image. When the size is chosen so as to exclude the diffracted beams, one has the configuration normally used for low-resolution defect studies, so-called *diffraction contrast*. In this case, a crystalline specimen is oriented to excite a

particular diffracted beam, or a systematic row of reflections, and the image is sensitive to the differences in specimen thickness, distortion of crystal lattices due to defects, strain and bending.

2.6.1.5 Phase Contrast

Diffraction contrast is a dominant mechanism for imaging dislocations and defects in the specimen. However, the resolution of this imaging technique is limited to 1-3 nm. Diffraction contrast mainly reflects the long-range strain field in the specimen and it is unable, however, to provide high-resolution information about the atom distribution in the specimen.

The diffraction of electrons is purely a result of the wave property of particles. The *wavelength* of an electron is a typical quantity for characterizing an incident plane wave.

The calculation of electron wavelength has been performed previously, however, without consideration the perturbation of the crystal potential on the electron kinetic energy. If the electron is traveling in a crystal, which is characterized by an electrostatic potential field V(x,y,z), the equation should be modified as

$$eU_0 = K.E. + P.E = \left(\sqrt{m_\circ^2 c^4 + p^2 c^2} - m_\circ c^4\right) + (-eV)$$

Therefore, the structure perturbed electron wavelength can be obtained. The effective *wave number* is

$$K_{eff} = \frac{1}{\lambda_{eff}} = \frac{p}{h} = \frac{1}{h}\left[2m_\circ e(U_0 + V)\left(1 + \frac{e(U_0 + V)}{2m_\circ c^2}\right)\right]^{1/2}$$

$$= \frac{1}{\lambda}\left[\left(1 + \frac{V}{U_0}\right)\left(1 + \frac{eV}{2m_\circ c^2 + eU_0}\right)\right]^{1/2}$$

$$\approx \frac{1}{\lambda}\left[1 + \frac{V(r)}{U_0}\right]^{1/2}$$

$$\approx \frac{1}{\lambda}\left[1 + \frac{V(r)}{2U_0}\right]$$

where an approximation of V << U_0 is made. We now consider a case in which the specimen covers only half space and leave the other half as vacuum. Thus the relative phase shift of the wave traveling in the crystal field relative to the wave traveling in the absence of a field for a specimen thickness d is

$$\int_0^d dz\, 2\pi \left(\frac{1}{\lambda_{eff}} - \frac{1}{\lambda}\right) \approx \sigma V_p(b)$$

$$\sigma = \frac{\pi}{\lambda U_0}$$

The *projected potential* of the crystal is

$$V_p(b) = \int_0^d dz\, V(r)$$

Therefore, the effect of the potential field is represented by multiplying the wave function by a phase grating function

$$Q(b) = \exp[i\sigma V_p(b)]$$

This is known as the *phase object approximation* (POA), in which the crystal acts as a phase grating filter. From this expression, it can be seen that the effect of the crystal potential is to modify the phase of the incident electron wave. The variation of the projected crystal potential results in the change of electron phase. The contrast produced by this mechanism is called *phase contrast*.[99]

CHAPTER THREE

GRAPHENE

Graphene on Ni(111)

3.1 Introduction

Graphene layers (or monolayers of graphite) on transition-metals surfaces have been known approximately for three decades. First experiments on graphene/Ni interfaces can be traced back to the mid-1970s [35–39]. In these early experiments segregation of bulk-dissolved carbon on different surfaces of Ni was investigated in order to explore the influence of the graphene layer on their catalytic activity. Structural stability and different growth modes of graphene layers were studied in these works mainly by means of low-energy electron diffraction (LEED) and Auger-electron spectroscopy (AES). Later on, investigations of the atomic structure of graphene on a Ni surface were performed [40,41]. The so-called *fcc* - *hcp* arrangement of carbon atoms above the Ni(111) surface was proposed based on the results of surface extended-energy-loss fine-structure spectroscopy studies [105]. The graphene layer on Ni(111) was found to be flat and slightly expanded compared to bulk graphite (by ~2%). The graphene-Ni distance was estimated to be 2.80 Å, and the Ni(111) substrate was found to remain unchanged. The atomic structure of the graphene/Ni(111) system was also investigated by means of LEED intensity analysis of particular diffraction spots [106]. The results of this study did not support the previous conclusions about the system geometry [105], and *top-fcc* configuration with a slightly buckled graphene layer was found to be the most probable configuration. This work also predicted a shorter distance of 2.10 Å between the graphene layer and the Ni(111) surface in agreement with the main observations of electron spectroscopy experiments [106].

The electronic structure of the graphene/Ni(111) system was investigated by means of angle-integrated photoemission, electron energy-loss spectroscopy (EELS), and ionization loss spectroscopy methods [40–42]. The energy bands of graphene were found practically unchanged compared to those of a pure graphite crystal, but an almost rigid shift to higher binding energies of all graphene-derived bands was detected in the experiment, indicating a charge transfer of 0.02 e^-/carbon atom from the Ni substrate to the graphene overlayer. Further experiments on graphene/Ni(111) [21,43] performed by means of angle-resolved PES showed that the energy shift to higher binding energies is different for π- and σ-derived states indicating the different strength of hybridization between Ni 3*d* valence band states and out-of-plane and in-plane

valence band states of the graphene layer. The orbital hybridization of the valence band states of graphene and the substrate leads to a considerable interaction between C and Ni atoms, resulting in a rather short distance between graphene and Ni(111), and also to the weakening of the C–C in-plane bonds.

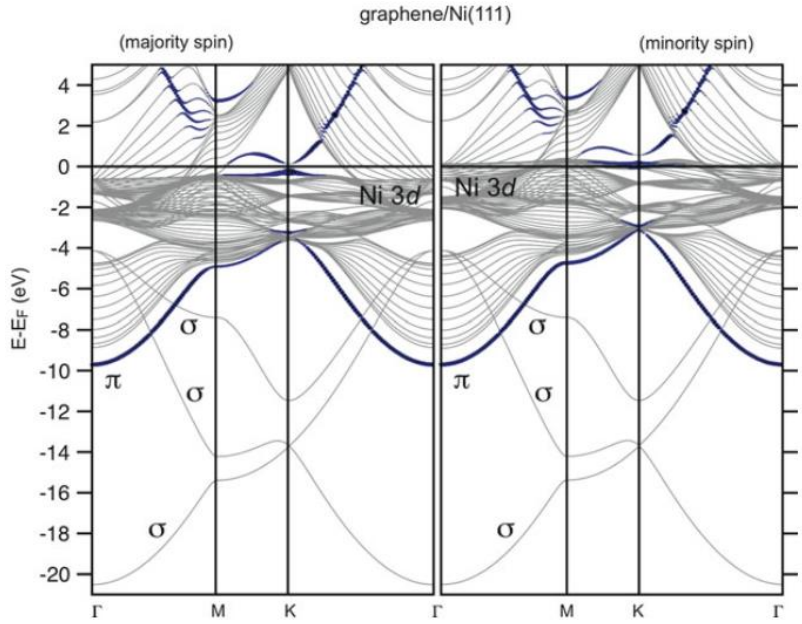

Figure 3.1: Calculated majority and minority spin band structures for a slab terminated by graphene/Ni(111) interface for a most energetically favorable *top-fcc* configuration. For the *blue (darker) lines*, the carbon p_z character is used as a weighting factor. [109]

These results were confirmed by recent experiments [45,46] and theoretical calculations [44,47–49] (Figure 3.1). This section presents a detailed analysis of the growth and electronic structure of graphene on transition metal surfaces, focusing mostly on Ni(111). The main experimental observations are presented and discussed in the light of the currently available band-structure calculations.

3.2 Atomic Structure of Graphene on Ni(111)

Figure 3.2a shows an STM image of single-layer graphene on Ni(111) after thermal decomposition of propylene. A typical LEED pattern of monolayer graphene on Ni(111) is presented as an inset. The graphene layer is continuous and exhibits a highly ordered crystallographic structure without any visible defects even over large areas. Since Ni(111) and graphene have the nearly similar lattice parameters (the lattice mismatch is of only 1.3 %), graphene forms a hexagonal (1×1) structure. A higher magnification STM image of the graphene surface is shown in Figure 3.2b with the honeycomb of ideal graphene marked in the image.

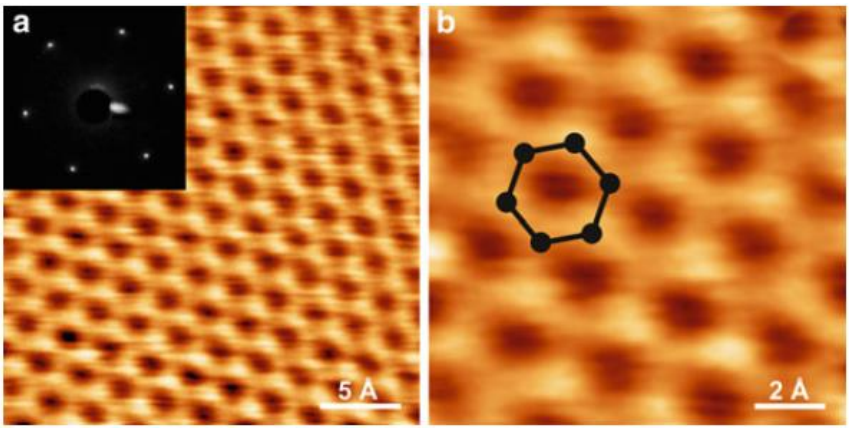

Figure 3.2: (**a**) A topographic STM image of the high-quality graphene/Ni(111) system. The inset shows a LEED image obtained at 63 eV. (**b**) Magnified STM image of the perfect graphene lattice. The graphene honeycomb is marked in (**b**). Data are taken from [111]

So far, several possible atomic configurations were considered for the graphene/Ni(111) interface. Three "high-symmetry" structures are known as *hcp-fcc*, *top-hcp*, and *top-fcc*. In the *top-hcp* configuration, the C atoms are placed directly above the Ni atoms of the first layer (top site) and the second layer (*hcp* site) [112]. In *top-fcc*, the C atoms are arranged above the Ni atoms of the first and third (*fcc*) layers. In the *hcp-fcc* configuration, the C atoms are placed above *hcp* and *fcc* sites. Three additional configurations were considered recently, which were called *bridge-top*, *bridge-fcc*, and *bridge-hcp*. In these structures, the C atoms are not placed in *hcp-fcc*, *top-hcp*, and *top-fcc* sites but in between [115].

At the moment, no clear consensus exists about which of the above described structures is more energetically stable and which kinds of structures are observed in experiments. From the

theoretical side, Bertoni et al. [112] used density functional theory (DFT) with the Perdew, Burke, and Ernzerhof generalized gradient approximation (GGA-PBE), which indicated the *top-fcc* to be the most stable atomic configuration at the graphene/Ni(111) interface. DFT-PBE studies were also performed by Kalibaeva et al. [116][reporting that *top-fcc* structure is the lowest energy configuration, whereas *hcp-fcc* has been shown to be unstable. The calculations including three additional "low-symmetry" configurations showed that within DTF with GGA-PBE, none of the structures is stable at the experimentally relevant temperatures; with local-density approximation (LDA), the *bridge-top* configuration was found to be the most energetically favorable one [115]. However, the performed k-point sampling of the Brillouin zone performed in this work seems to be not sufficient for this system (compare [115] and [114]), requiring a further investigations of the graphene/Ni(111) system. From the experimental side, Rosei et al. [105] and Klink et al. [117] found that the most stable structure is *hcp-fcc*, whereas Gamo et al. [106] found *top-fcc* to be the most favorable configuration.

Graphene terraces (Figure 3.2) have a peak-to-peak roughness of 0.2 Å and show a honeycomb structure with a lattice constant of 2.4 ± 0.1 Å [Figure 3.2b], which agrees well with the expected 2.46 Å lattice spacing of graphene [22,46,53,54]. STM images show that within each honeycomb carbon atoms corresponding to different sites appear with a different contrast, which can be attributed to the differences in the local stacking of the graphene sheet and the Ni(111) substrate. Therefore, STM images could be interpreted in the following way: Figure 3.1 shows a single layer graphene, where one half of carbon atoms are situated on top of nickel atoms and the other half occupy one of the two non-equivalent threefold hollow cites – *fcc* or *hcp*. However, it turns to be impossible to directly identify which of the hollow sites is occupied.

3.3 Electronic Structure of Graphene on Ni(111)

The lattice matched interface between graphene and Ni(111) is among the most extensively studied graphene/metal systems [21,40,41,43,46,47,53–60]. A considerable modification of graphene's electronic structure due to the orbital mixing between Ni 3*d* and graphene π states was predicted theoretically [44,47–49,57] and observed recently by near-edge X-ray absorption fine-structure spectroscopy (NEXAFS) [59,60]. Figure 3.3 shows angle-dependent C 1*s* NEXAFS spectra of graphene on Ni(111) in comparison with the C 1*s*

absorption spectrum of highly oriented pyrolytic graphite (HOPG). The spectrum of HOPG is characterized by the C 1*s*→π^* resonance at 285.3 eV and two C 1*s*→σ^* resonances around 291.6 eV and 292.7 eV. The shape of this spectrum can be best described including effects of dynamical screening of the core hole [126]. Comparing the C 1*s* NEXAFS spectrum of the graphene/Ni(111) system with the reference graphite spectrum, considerable changes in the spectral shapes are observed, indicating a substantial orbital hybridization between graphene and Ni valence band states at the interface. This is a direct experimental evidence for significant chemical interaction between graphene and Ni(111), in accordance with the relatively high adsorption energy of 125 meV per C atom calculated for this system [127]. A new strong feature at 287.1 eV originates from transitions to the states with π symmetry, as evident by the angle dependence.

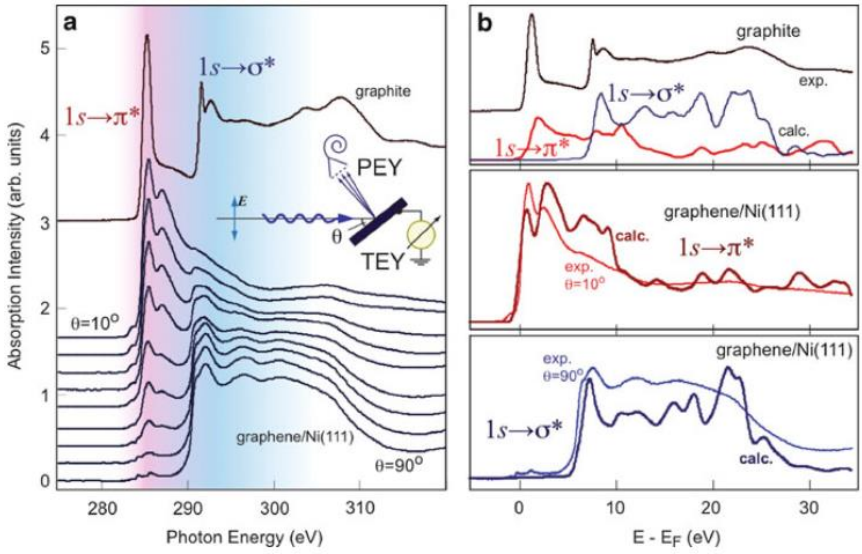

Figure 3.3: (**a**) Angle-dependent C 1*s* NEXAFS spectra of the graphene/Ni(111) system measured as a function of angle θ, between polarization vector of the incoming linearly polarized light and the surface normal. (**b**) Comparison between experimental NEXAFS spectra and calculated EELS of graphite and graphene/Ni(111) for two different incident angles, θ , where transitions from C 1*s* core level on mostly π^*- or σ^*-states occurred. Experimental and theoretical data are from [46,59] and [112] respectively.

The characteristic double-peak structure at 285.5 eV and 287.1 eV can be qualitatively understood already with the ground-state DFT calculations [112], while the dynamics of core hole screening has to be considered for correct reproduction of the spectral profile [125]. In the ground-state approximation, the first π^* resonance can be roughly associated with the unoccupied C 2*p* density of states (DOS) located at the C atoms on top of Ni atoms, while the second π^* peak

is mainly due to the C 2*p* DOS on the C atoms located at *fcc* hollow sites [47,59,60]. However, in a real experiment individual contributions are considerably mixed and further affected by the core hole and its dynamical screening. The σ^* resonances are also influenced by the interaction with the substrate: they are visibly broadened and shifted by 0.6 eV to lower energies. The broadening is a result of the increased screening by the substrate electrons. The reduction of the $\pi^*-\sigma^*$ separation reflects the reduced anisotropy of the potential for outgoing electrons due to the slight ripple in the graphene layer on Ni(111) accompanied by a softening of the C–C bonds.

In the following, we would like to compare the NEXAFS results [46,59] with the recently calculated C *K*-edge EELS spectra for the graphene/Ni(111) interface [112]. The calculated EELS spectra are found to agree well with the experimental NEXAFS data [see Figure 3.3b]: (1) the spectra show the same angle (scattering vector) dependence and (2) the experimentally observed NEXAFS features are well reproduced in the calculated EELS spectra. For example, two peaks in the NEXAFS spectra in the $1s \rightarrow \pi^*$ spectral region at 285.5 eV and 287.1 eV photon energy can be assigned to the double peak structure in the calculated EELS spectrum at 0.8 eV and 3.0 eV above the Fermi level [112]. According to the theoretical calculations [112], the first sharp feature in the NEXAFS spectrum is due to the transition of the electron from the 1*s* core level into the interface state I_4 above the Fermi level (around the *K* point in the hexagonal Brillouin zone, see Figure 3.1), which originates from the C p_z – Ni 3*d* hybridization and corresponds to the antibonding orbital between a carbon atom C-*top* and an interface Ni atom. The second peak in the NEXAFS spectrum is due to the dipole transition of an electron from the 1*s* core level into the interface state I_5 above the Fermi level (around the M -point in the hexagonal Brillouin zone, see Figure 3.1), which originates from C p_z –Ni p_x, p_y, 3*d* hybridization and corresponds to a bonding orbital between C-*top* and C-*fcc* atoms, involving an Ni interface atom. In the case of the NEXAFS C $1s \rightarrow \sigma^*$, the theory also correctly describes the shape of the absorption spectra [112].

Since the π electrons of graphene are actively involved in the bonding with the Ni substrate, the overall strength of the C–C bonds is considerably decreased. This fact is reflected in the relatively low growth temperature ($500^{\circ}C - 650^{\circ}C$ depending on the hydrocarbon flux) and high solubility of carbon in Ni. The growth temperature is significantly lower than that used for graphene formation on more passive metal surfaces (e.g., $850^{\circ}C - 1{,}000^{\circ}C$ in the case of

graphene/Pt or graphene/Ir), where the C–C bonds are not weakened so drastically by the substrate. The metastable equilibrium state of graphene on Ni(111) associated with the permanent formation and re-evaporation of graphene flakes can be reached in the temperature window as low as $650^{\circ}C - 670^{\circ}C$ [121] [Figure 3.4 a, b]. CVD growth is assisted by carbon dissolving in Ni and segregation to the surface, as can be judged from direct monitoring of the growth process with high-resolution C 1*s* PES (Photo-electron spectroscopy). Figure 3.4 b shows the C 1*s* PE spectra of the final graphene film grown on Ni(111) obtained at different substrate temperatures [121]. From Figure 3.4, it is evident that with increasing temperature the signal at 283 eV gradually decreases and vanishes completely close to the equilibrium growth conditions. This implies that all atomic carbon from the substrate is activated at this temperature and participates in graphene formation and/or the contribution from the borders of graphene flakes is reduced due to the reduced nucleation density.

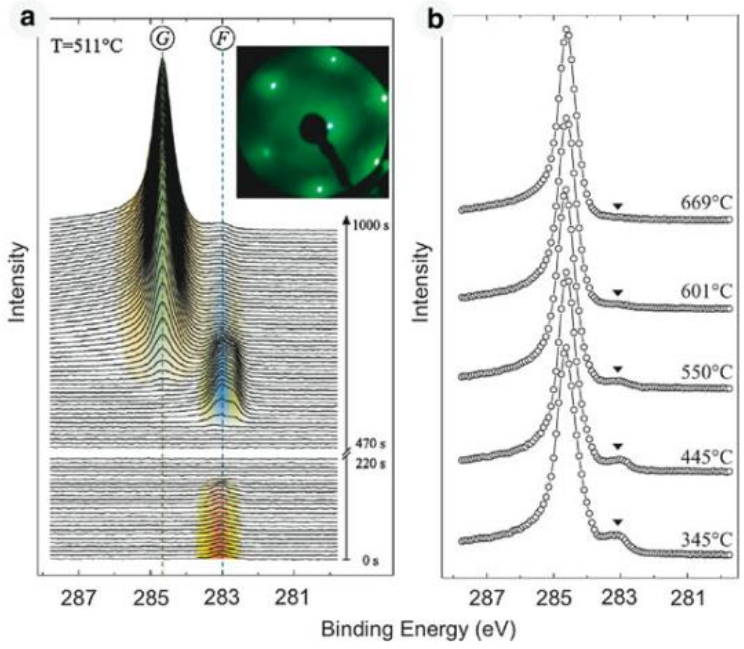

Figure 3.4: (**a**) Time evolution of the PES intensity in the C 1*s* region during the graphene growth. Individual spectra were recorded every 10s. *F* and *G* mark the signals from C_3H_6 fragments and graphene, respectively. The inset shows a LEED pattern (primary energy was 80 eV) after growth of graphene. (**b**) C 1*s* PES spectra of the resulting graphene layer obtained at different temperatures. Data are taken from [121]

Figure 3.5 shows two series of ARPES spectra measured along the $\Gamma - K$ direction of the hexagonal Brillouin zone of the graphene/Ni(111) system [111]. Each series is extracted from the 3D sets of data of photoemission intensity $I(E_B , k_x , k_y)$, where E_B is the binding energy and k_x, k_y

are the orthogonal components of the in-plane wave vector. The presented photoemission data are in very good agreement with the previously published results [20,21,43,45,54]. In Figure 3.5, one can clearly discriminate dispersions of the graphene π- and σ-derived states in the region below 2 eV of the binding energy (BE) as well as Ni 3*d*-derived states near E_F. The binding energy of the graphene π states in the center of the Brillouin zone (in the Γ point) equals to 10.1 eV, which is approximately by 2.4 eV larger than the binding energy of these states in pure graphite [53,59]. The shift to larger binding energy is different for σ and π valence band graphene-derived states. This behavior can be explained by the different hybridization strength between these states and Ni 3*d* valence band states, which is larger for the out-of-plane oriented π states compared with the one for the in-plane oriented σ states of the graphene layer.

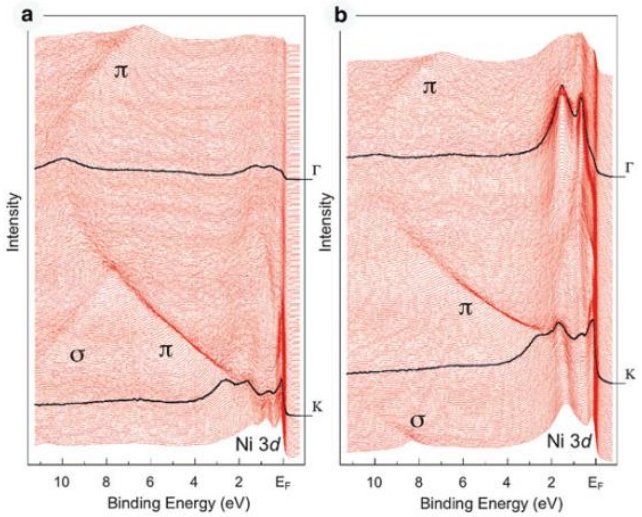

Figure 3.5: Angle-resolved photoemission spectra of the graphene/Ni(111) system recorded along the Γ - K direction of the hexagonal Brillouin zone at (**a**) 70 eV and (**b**) 100 eV of photon energy. Spectra corresponding to Γ and K points are marked by thick black lines. [111]

The effect of hybridization between Ni 3*d* and graphene π states can be clearly demonstrated in the region around the *K* point of the Brillouin zone: (1) one of the Ni 3*d* bands at 1.5 eV of BE changes its binding energy by ≈ 150 meV to larger BE when approaching the *K* point; (2) a hybridization shoulder is visible in photoemission spectra, which disperses from approximately 1.6 eV to the binding energy of the graphene π states at the *K* point. The strong hybridization observed in PES spectra underlines the fact that the π states might become spin-polarized and might gain a non-zero magnetic moment due to the admixture of the Ni 3d states into the C π states.

Considering the electronic band structure of the graphene/Ni(111), the region around the *K* point delivers the most interesting and important information with respect to the possible spin-filtering effects in the graphene/FM (Ferromagnetic) or FM/graphene/FM sandwich-like structures. First, the spectral function of the graphene layer on Ni(111) is characterized by the absence of well-ordered structure of the graphene π-bands in the vicinity of the Fermi level and second, the Dirac-cone is not preserved. Both observations can be attributed to a strong interaction between graphene layer and metallic substrate leading to a strong hybridization between the graphene π and the Ni 3*d* valence band states. In the vicinity of the *K* point, a number of photoemission peaks can be clearly distinguished: (1) a sharp peak about the Fermi level at 0.1−0.2 eV BE, (2) a graphene π-states-related peak at 2.65 eV BE, (3) two peaks at 0.7 eV and 1.65 eV BE.

The analysis of the experimentally obtained electronic structure has recently been performed in [111] relying mainly on two comprehensive sets of electronic structure calculations currently available for the graphene/Ni(111) system [47,49]. Calculations by Bertoni et al. [112] predict the existence of three interface states below the Fermi level originating from the strong hybridization between the Ni 3*d* and the graphene π states and corresponding to: (I_1) bonding between C-*fcc* and interface Ni atoms; (I_2) bonding between C-*top* and interface Ni atoms; (I_3) antibonding between C-*fcc* and interface Ni atoms. Karpan et al. [114] performed the band structure calculations of the graphene/Ni(111) system with the major emphasis on the investigation of the spin-dependent transport properties of the Ni/graphene/Ni sandwich structures. Both calculations yielded a quite complicated band structure of the graphene/Ni(111) system around E_F due to the strong hybridization between the graphene and the Ni valence band states. The interpretation of the experimentally observed photoemission features around the Fermi level could be performed as presented in Ref. [111]. The photoemission peak close to E_F (0.1–0.2 eV BE) could be considered as a combination of the interface state I_3 (both spins) with a large contribution of the graphene π–character and the Ni 3*d*(↓)-band. The second peak at 0:7 eV BE could be assigned to the combination of the Ni 3*d*(↑)- and Ni 3*d*(↓)-bands present in both calculations. The feature at 1.65 eV could be considered as a combination of Ni 3*d*(↑)-band and I_2(↓)-state with a large graphene π-character. The last photoemission peak (2.65 eV BE) could be assigned to the interface state I_2(↑) with large contribution of the graphene π-character. In order

to check the theoretical predictions concerning the CPP (current-perpendicular-to-the-plane) spin-dependent electronic transport properties of the ideal graphene/Ni(111) interface, an analysis of the constant energy photoemission maps close to E_F was performed in [111] Figure 3.6). However, flat Ni 3*d* bands, which dominate the photoemission intensity around E_F make the detailed analysis rather difficult.

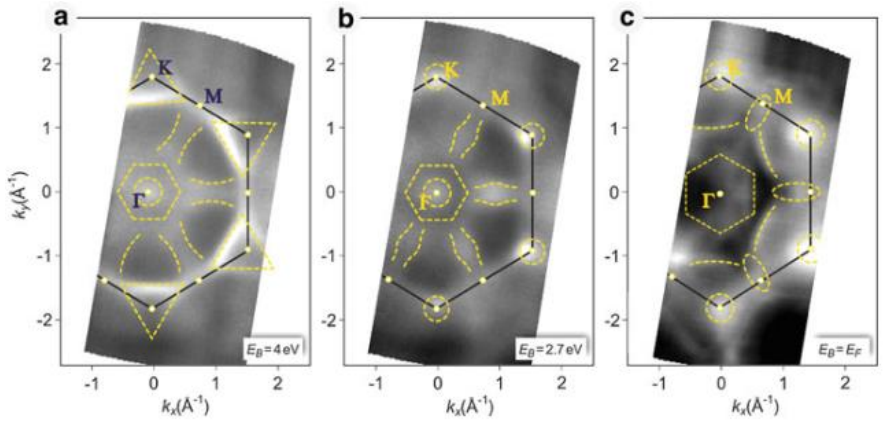

Figure 3.6: Constant energy cuts of the 3D data sets in the energy-wave vector space, I(***E***B, ***k***x, ***k***y), obtained through a β-scan from the graphene/Ni(111) system at 100 eV of photon energy. The energy cuts are taken at (**a**) 4 eV and (**b**) 2.7 eV BE as well as at (**c**) E_F. [111]

The energy cuts were taken at (a) 4 eV and (b) 2.7 eV of BE as well as at (c) the Fermi level. The energy cut at EB = 4 eV shows characteristic photoemission intensity patterns of the graphene layer, which reflect the symmetry of the system. Below the Dirac point (crossing of straight dispersion lines of π states in free-standing graphene), the graphene π bands are visible in the first Brillouin zone, whereas no bands can be seen in the second one [128]. Additionally, several energy bands are present in the middle of the Brillouin zone (outlined by dashed yellow lines), which also show hexagonal symmetry. These bands originate from the hybridization of the Ni and graphene valence band states. The constant energy cut taken in the region of the minimal binding energy of the graphene π states (E_B = 2.7 eV) is shown in Figure 3.6 b. In the case of graphene/Ni(111), the Dirac point is not preserved due to the strong hybridization of Ni 3*d* and graphene π states around the *K* point. This can also be directly recognized at this energy cut, where graphene π states produce broad intensity spots instead of sharp points in the wave-vector space. As in the previous case, we observe a number of valence band states in the middle part of the Brillouin zone, which again could be assigned to the hybridization-derived states.

The most interesting and important information in view on the spin-dependent transport properties of the graphene/Ni(111) system can be extracted from the constant energy cut obtained at the Fermi energy, which is presented at Figure 3.6c. Already the analysis of Figure 3.5 a, b shows that the photoemission intensity is increased around the *K* point and along the *K*−*M* direction of the hexagonal Brillouin zone, that correlates with the increased photoemission intensity observed in the energy cut shown in Figure 3.6c for the Fermi energy. Additionally, a number of arcs surrounding the *K* points and weak (but distinguished) diamond-shape regions of increased intensity are clearly visible in the middle part and around the *M* points of the Brillouin zone, respectively. Upon the comparison of the obtained photoemission results for the graphene/Ni(111) system (Figure 3.5 and Figure 3.6) as well as the Fermi-energy cut with the band structure calculations for this system [33, 34, 69, 72] (Figure 3.1), there are very good agreement between theory and experiment. Particularly, the region around the Fermi level for the ideal graphene/Ni(111) system is well reproduced in the experiment, confirming the main predictions of the theory. However, more experimental and theoretical efforts are required to determine the spin character of individual bands.

3.4 Low Energy Plasmon of Graphene/Ni(111)

In this part will talk about angle resolved electron-energy-loss (AREELS) investigation of the low-energy plasmon (the so-called sheet plasmon) in the Graphene/Ni(1111) system, arising from the collective excitation of the hybridized charge density around the Fermi level. AREELS show a low energy plasmon dispersing up to about 2 eV, resulting from fluctuation of a charge density located around the Fermi energy, due to hybridization between Ni and graphene states. The dispersion is typical of a two-dimensional charge layer, and the calculated Fermi velocity is a factor of ~0.5 lower than in isolated graphene.

The AREELS measurements were performed at room temperature in an ultrahigh vacuum chamber (2×10^{-10} Torr base pressure), using a high-resolution electron energy loss (EEL) spectrometer with two 50 mm hemispherical deflectors for both monochromator and analyzer. The incident electron beam was at a fixed angle of incidence of 45° with respect to the surface

normal, along the ΓK surface azimuth, with 20 eV kinetic energy. A medium energy resolution of 20 meV was set to achieve the best signal-to-noise ratio. The angular acceptance of the analyzer was 2°.

The momentum transfer component parallel to the surface $q_{\parallel}$ was changed by rotating the analyzer, always along the ΓK azimuthal direction; its value was calculated by the following equation, which reflects the conservation of energy and of in-plane momentum: $q_{\parallel} = [\sin\theta_i - (1 - E_l/E_p)^{1/2} \sin\theta_s] (2mE_p/\hbar^2)^{1/2}$, where E_p is the energy of the primary electron beam, E_l the loss energy, m is the mass of the free electron, θ_i and θ_s are the angles with respect to the surface normal of the sample for incident and scattered electrons, respectively.

Ni substrate was prepared by a well established cleaning procedure. Several cycles of sputtering with 2 KeV Ar^+ ions and annealing at 1200 K were repeated until a sharp LEED pattern and the Auger spectum showed the achievement of a clean and ordered Ni (111) surface.

Graphene layer was prepared by exposing the Ni sample to 200 L (1 Langmuir = 10^{-6} Torr s) ethylene at 750 K. The LEED spots of the graphene/Ni (111) system revealed a well-ordered p(1×1) overstructure, as expected from the small lattice mismatch, while the Auger spectrum showed the typical graphitic lineshape (Figure 3.7).

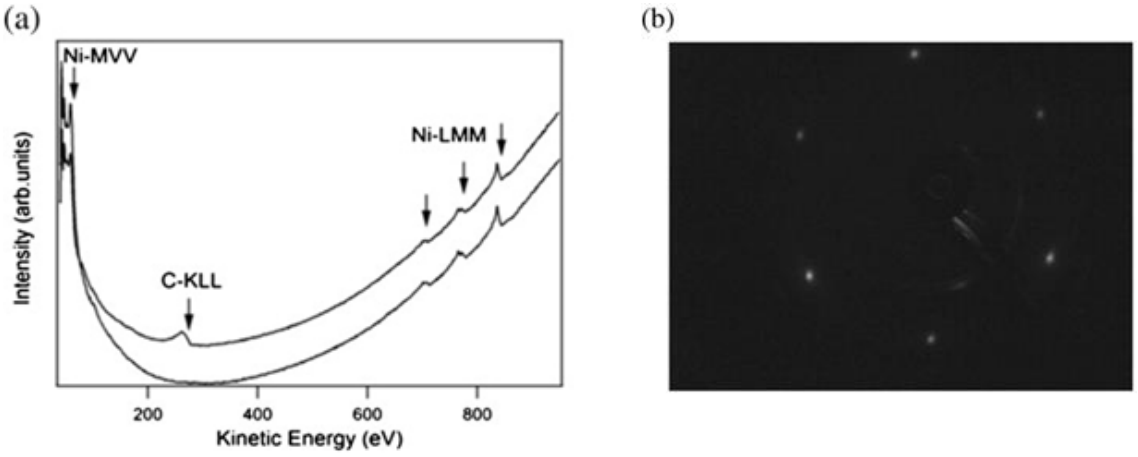

Figure 3.7: (a) AES spectra of clean Ni surface (bottom curve) and graphene/Ni (111) system; (b) LEED image of the graphene/Ni (111) system collected at a primary electron energy of 65 eV

Figure 3.8 shows the AREEL spectra in the 0–6 eV loss range, obtained on the graphene-covered Ni (111) sample, for different values of the scattering angle θ_s. The prominent feature, a plasmon located in the 0–2 eV loss range, dominates all the spectra, changing its position and intensity with changing θ_s.

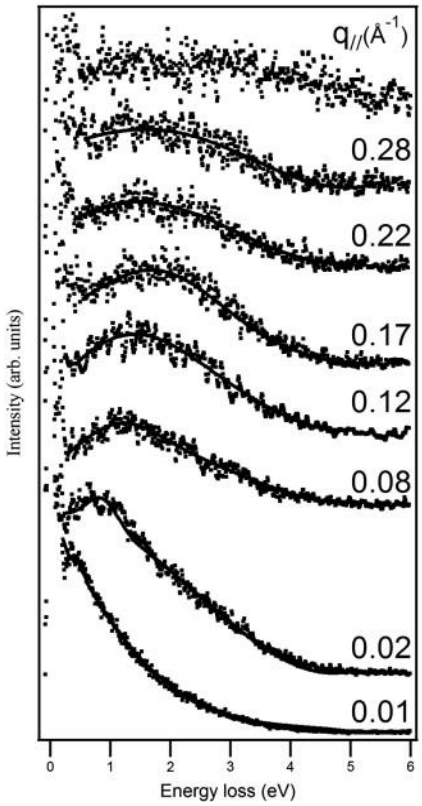

Figure 3.8: EEL spectra obtained on graphene-covered Ni (111) for different values of the scattering angle θ_s. The fitting curve (Gaussian + polynomial background) was superimposed on each experimental curve. The position of the main peak in the spectrum has been used to calculate the indicated $q_{||}$ value

In order to extract the energy and width of the peak, each spectrum has been fitted with a polynomial background and a Gaussian lineshape for the plasmon. Then, the $q_{||}$ value has been calculated as mentioned above. The relative loss intensity rapidly drops and the peak nearly disappears at around $q_{||} = 0.3$ Å^{-1} (upper curve in Figure 3.8). The $q_{||}$ dependence of the loss intensity reflects the sharp angular distribution of the dipole lobe being rapidly dropped within a small $q_{||}$ range. Further, at around $q_{||} = 0.3$ Å^{-1} the intensity of the plasmon rapidly disappears, this additional drop suggests the onset of Landau damping where the plasmon branch enters the single-particle excitation regime and decays into electron–hole pairs.

The error in the determination of the loss energy has been estimated by considering the errors in determining peak position in the fitting process, while the error in $q_{||}$, mainly due to the

detector angular acceptance, is in the range of ± 0.02–0.03 $Å^{-1}$. The energy dispersion curve of the observed loss peak has been obtained along the ΓK direction of the hexagonal BZ, and is shown in Figure 3.9.

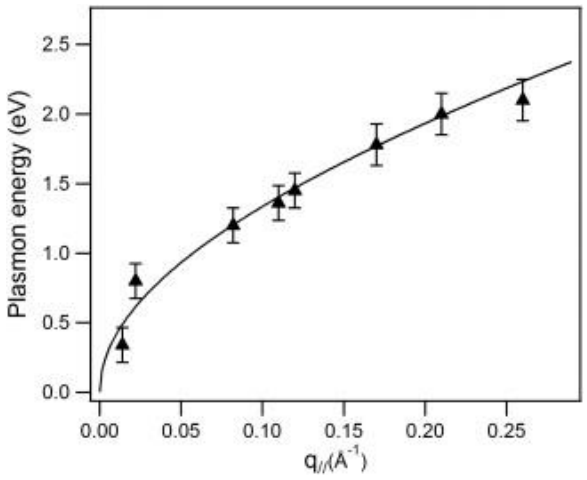

Figure 3.9: Energy dispersion relation of the observed loss peak. The solid curve represents the best fit of our experimental result according to full RPA dispersion

In the same figure, a fitting curve is also shown, which will be discussed ahead.

As discussed by Hwang and Das Sarma [129], because of the different energy band dispersions, screening properties in doped graphene exhibit significantly different behavior with respect to conventional 2D systems [130]. Although plasmons in both graphene and conventional 2D charge densities commonly show the $\sqrt{q_{\|}}$ dependence in the long wavelength limit, the dispersions calculated including the finite wavevector nonlocal effects, within the random phase approximation (RPA), appear to be quite different for the two cases. Liu et al. [131] made a comparative High Resolution EEL study of the plasmon excitations in both an Ag layer on a Si substrate and epitaxial graphene grown on a SiC substrate, finding intriguing differences. As predicted, the two systems, which both can be considered as one-atom thick two dimensional electron gas, behave in different ways, with graphene/SiC showing a screening behavior very different from that of an ideal 2D system. In fact, non-local corrections for finite q cause a linearly decreasing $\omega(q)$ for graphene with increasing q while produce an opposite trend for typical 2D systems. Furthermore, very recently the measured dispersion of the intraband plasmon in single layer graphene (SLG) with no multilayer effects showed distinct features in the plasmon damping and its decay mechanism [132].

The collective properties of graphene on strongly interacting transition metal surfaces are expected to be very different with respect to suspended graphene or weakly interacting surfaces. In an early paper, Nagashima *et al* [133] observed two-dimensional plasmons in monolayer graphite on TiC (111) surface; they ascribed the origin of the low energy collective excitation to new electronic states at the Fermi level due to the hybridization between π states of graphite and substrate *d* electrons. At chemisorption interfaces, according to recent theoretical results for graphene/Ni electronic structure [6,7], graphene's intrinsic π-band structure is significantly changed. Due to a large wave function overlap between metal's *d*-electrons and graphene's π-electrons, a new distinctive density of states appears at the Fermi level. X-ray absorption spectroscopy (XAS) and angle resolved photoemission investigations [8,9] demonstrate the existence of such interface bands. The comparison of the experimental obtained electronic structure with available band structure calculations allowed the clear assignment of spectral features in the XAS and ARPES data.

Among these states, those partially occupied by electrons contribute to form an interface charge density *n*. We assign the dispersing plasmon measured in our AREEL spectra to a collective excitation of this interface charge density.

Calculated dispersions of the intraband plasmon are inherent to doped graphene sheet, where the Dirac cone structure is preserved, or to 2D nearly free electron gas [1,2]. However, graphene/Ni interface is a more realistic complex interface and it was demonstrated how the strong graphene-metal interaction significantly influences the Dirac cone structure [112]. An inspection of our data indicates that the dispersion curve is similar to the plasmon dispersion of a 2D-confined electron gas which sustains a surface plasmon. Within the framework of the non-local response theory using RPA, the plasmon dispersion of a 2D nearly free-electron gas is the following [130]:

$$\omega_{2D}\left(q_{||}\right) = \left[4\pi N_{2D} e^2 m^{*-1}(1+\varepsilon_s)^{-1}\left|q_{||}\right| + 6N_{2D}h^2\pi(2m^*)^{-2}\left|q_{||}\right|^2 + O\left(\left|q_{||}\right|\right)^3\right]^{1/2}$$

where $\omega_{2D}(q_{||})$ is the 2D plasma frequency, N_{2D} is the areal density of electrons, m^* is the effective electron mass, e is the elementary electric charge and ε_s is the dielectric constant of the

substrate. The first term is identical to the $\sqrt{q_{\|}}$ dispersion from the classical local response theory for a very thin film [137].

The second and higher-order term originates from non-local effects and can be rewritten as $3/4v_F^2 q_{\|}$, where v_F is the Fermi velocity [130].

The solid curve in Figure 3.8 is the best fit of our experimental data according to Stern's full RPA dispersion. It has to be noted that non local effects cause a linearly increasing $\omega(q)$ with increasing q. This means that the screening properties of the graphene/Ni system associated to the interface charge density are very different from what happens in the weakly interacting graphene/SiC system [131], showing instead a greater similarity with normal 2D electron gas. The fitting procedure allowed us to obtain quantitative information. From the fitting procedure including the second-order term in $|q_{\|}|$, we obtain $v_F = 5 \cdot 10^5$ m/s, which then is only a factor ~ 0.5 smaller with respect to that of isolated graphene. Due to the indetermination on the dielectric constant of the Ni substrate, only the ratio between N_{2D} and $m^*(1 + \varepsilon_s)$ is obtained. If we report m^* in units of electron mass, the data have the best fit parameter $N_{2D}m^{*-1}(1 + \varepsilon_s)^{-1} = 1.5 \cdot 10^{15}$ cm^{-2}, which is comparable to the electron density reported in Ref. [133] for a low energy 2D plasmon in monolayer graphite on TiC (111).

3.5 Interface-π Plasmon of Graphene/Ni(111)

The aim of this experiment was to investigate by EELS the interband plasmon of the graphene/Ni(111) system. The interface-π plasmon, related to interband transitions involving hybridized states at the K point of the hexagonal Brillouin zone, has been measured at different scattering geometries. The resulting dispersion curve exhibits a square root behavior, indicating the 2D character of the interface collective excitation.

Figure 3.10 shows a series of EEL spectra collected at different analysis angles with respect to the surface normal in the 0−12 eV loss range.

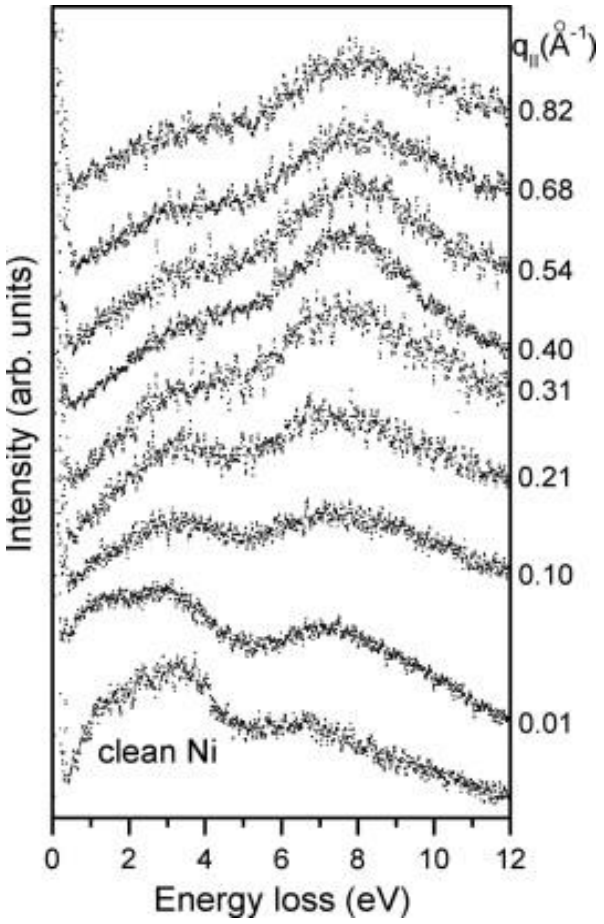

Figure 3.10: EEL spectra obtained on clean Ni(111) (lower curve) and graphene-covered Ni(111) for different experimental geometries. The $q_{\|}$ values calculated for each of the dispersing interface-π plasmon peaks, are shown on the right side.

The lower spectrum refers to clean Ni(111), while the other spectra have been obtained on the graphene-covered Ni(111) sample. The clean Ni(111) spectrum and the lower of the graphene/Ni(111) spectra, have been obtained in the same experimental geometry. The EEL spectrum of the clean sample shows structures due to collective excitations involving Ni electronic states. Once the graphene layer is formed, a peak appears centered at about 7 eV, whose energy changes with changing analysis angle with respect to the surface normal. After polynomial background subtraction, the position and width of such peak were determined by Gaussian fitting. The $q_{\|}$ for each EEL spectrum was calculated as mentioned above, and the results are shown on the right side of Figure 3.10. The error in the determination of E_1 resulting from the Gaussian fit is in the range of ±80–100 meV, while the error in $q_{\|}$, mainly determined by the detector angular acceptance, is in the ±0.05–0.07 Å^{-1} range. Figure 3.11 shows a plot of the energy loss values associated to the interband plasmon, as a function of $q_{\|}$. For increasing $q_{\|}$,

the signal-to-noise ratio in related energy loss spectra decreases, thus causing an increase of the uncertainty in the plasmon energy determination.

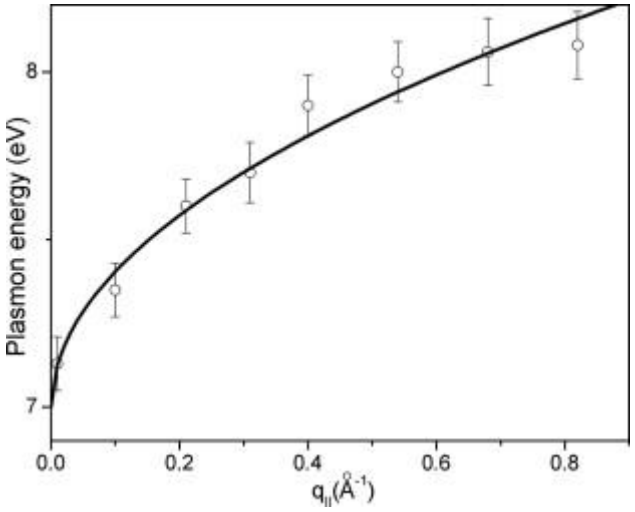

Figure 3.11: Energy loss values of the interface-**p** plasmon peak plotted vs. $\boldsymbol{q}_{\parallel}$. The line represents the dispersion curve obtained by a square-root fit of the experimental points, whose equation is given in the text.

The plasmon at about 7 eV in graphite is known as the π plasmon, arising from π–π* interband transitions at the M point of the BZ [1,2]. The dispersion of such plasmon shows the parabolic behavior typical of the fluctuation of a three-dimensional charge density [140]. In free-standing graphene, a loss at 4.8 eV in transmission electron energy loss experiments ($q \sim 0$) is attributed to the π plasmon excitation [141]. Electron energy loss experiments made on single wall carbon nanotubes give almost the same result for $q \sim 0$, and show a linear dispersion of the π plasmon, which is attributed to local field effects which mix transitions at K and M points of the BZ [142]. For graphene weakly bound on SiC(0001) a similar linearity of the π plasmon dispersion is found, also in this case attributed to local field effects [143].

The collective properties of graphene on strongly interacting transition metal surfaces are expected to be very different with respect to suspended graphene or graphene on weakly interacting surfaces. In an early paper, Nagashima et al. [144] found a nearly square root dispersion curve of the π plasmon for a "monolayer graphite" on TiC(111). Very recently, electron energy loss experiments performed on the graphene/Ni(1 1 1) system have shown a "reduced" parabolic dispersion of the same interband plasmon [145].

In view of the band structure calculations for graphene on Ni(111) [146], the origin of the dispersing plasmon located at about 7 eV has to be reconsidered. $\pi \rightarrow \pi$ transitions take place in graphene and in graphite between the K and M points of the BZ (with the main contribution coming from the high density-of-states region around M), giving rise to the so-called π plasmon. Such plasmon is found at around 4.8 and 7 eV in graphene and graphite respectively [141], quite close to the $\pi \rightarrow \pi$ excitation range (0–5 eV in graphite and 0–4 eV in graphene), due to the abrupt increase with energy of the real part of the dielectric function, caused by $\sigma \rightarrow \sigma^*$ transitions [139]. The $\pi + \sigma$ plasmon, on the contrary, does not suffer of a similar effect: in graphite it is peaked at 28 eV, a position considerably displaced with respect to the $\sigma \rightarrow \sigma^*$ peak in the imaginary part of the dielectric function, located at about 14 eV [139].

For graphene on Ni(111), the strong hybridization involving Ni 3d and carbon p_z states, causes a dramatic change in the band structure with respect to free-standing graphene and graphite. The occupied π band at point M is shifted to an higher binding energy of ~4.8 eV, and the π band present in graphene above the Fermi level between K and M points disappears, leaving an hybridized state at M at ~3.2 eV [146]. This means that the plasmon we observe at about 7 eV cannot be explained as in graphite or in graphene as related to $\pi \rightarrow \pi$ transitions. In ref. [146], four more interface states (three occupied and one unoccupied) are found around point K as a consequence of hybridization. These states, whose wave functions are located at the interface, correspond to bonding between the two inequivalent C atoms of graphene and topmost Ni atoms. In particular, the unoccupied interface state, located very close to the Fermi level at point K, corresponds to antibonding between carbon and topmost nickel atoms, for carbon atoms in ontop geometry [146]. We propose the plasmon at about 7 eV to be related to transitions involving these states: for this reason we call it interface-π plasmon. The final states of the interband transitions giving rise to the interface plasmon are not anymore states located 2–3 eV above the Fermi level at the M point of the BZ, as in graphite and weakly interacting graphene, but states around K just above the Fermi level, where hybridization destroys the Dirac cones. The interband transitions at M, involving the interface state located at ~3.2 eV above the Fermi level, have an onset of about 8 eV, and have to be considered to contribute to the high energy $\pi + \sigma$ plasmon, located at about 25 eV loss energy, rather than to the 7 eV plasmon.

Whether the character of the charge fluctuation involving these states is 2- or 3-dimensional is of great importance especially in view of possible applications in graphene-based devices. The frequency of a fluctuation in a strictly 2-dimensional charge density exhibits a square root dispersion [147]. In the case of Two-dimensional (2D) plasmons due to interband transitions in general bands localized at solid surfaces, the frequency can be expressed as $\omega_p^2 = \beta + \eta q$ [148]. The term β contains the transition energy between occupied and unoccupied bands and a depolarization term, while ηq expresses the energy of interaction between induced electric dipoles.

The line in Figure 3.11 is a fit of the dispersion points with the square-root equation $\hbar\omega = A + Bq^{1/2}$, where $A = 7.00 \pm 0.05$ eV represents the interface plasmon energy for $q_{\|} \sim 0$, and the positivity of the parameter $B = 1.28 \pm 0.08$ eV $Å^{1/2}$ indicates that the excitation is a longitudinal mode propagating along the surface [148]. In our energy loss measurements, the interface plasmon peak broadens with increasing q, and is not anymore present as a distinct feature for $q \sim 0.9$ $Å^{-1}$. The interface plasmon decay is mainly due to its proximity with strong interband transitions. Such a damping could also affect the magnitude of the oscillator strength, giving rise to a deviation from the ideal square root dispersion for increasing q. In fact, a slight deviation seems to be present in our dispersion curve in Figure 3.11, where the plasmon energy shows some convergence to a value located around 8 eV. To address this point, we are performing calculations of the real and imaginary part of the dielectric function of the graphene/Ni(111) system. Nonetheless, apart from the slight deviation mentioned, the simple analytical expression which better fits our dispersion curve is clearly of the square root type.

The square root behavior indicates that the interface-π longitudinal mode is related to the fluctuation of a strictly 2D charge density, associated to hybridized electronic states at point K of the BZ. An interband plasmon showing a 2D dispersion curve has also been observed for graphene formed on TiC(111), where XPS, UPS and EELS show a strong graphene/substrate hybridization [7,12]. Thus, on both Ni(111) and TiC(111) transition metal surfaces, where hybridization between carbon and nickel states takes place, the interband plasmon exhibits a 2D behavior. These findings are very different with respect to SWCNT and to graphene weakly interacting with SiC: in these cases, the linearity of the plasmon dispersion is attributed to local field effects [142].

Our findings are very different from those found recently on the same system on the basis of results obtained with a conventional EELS system, where a “reduced parabolic” dispersion of the interband plasmon is hypothized [145]. In fact, the experimental points shown in ref. 17 in the 0–1 $Å^{-1}$ q-range could be fitted by different analytical behaviors, whose validity could be estimated on the basis of the experimental error bars, which however are absent in their dispersion curve.

3.6 K-edge ELNES of Graphene/Ni(111)

Here, we present a reflection electron-energy-loss near-edge structure (RELNES) investigation of the graphene/Ni(111) system, in which the fine structure associated with the carbon K-edge loss peak is clearly revealed, and compared with the first-principles calculations of Bertoni et al., and also with the results obtained by transmission ELNES on pristine graphene.

Electron energy loss measurements were made in the specular reflection geometry by a conventional electron gun (Kymball Physics ELG-2A- 5950) and a 100 mm hemispherical analyser (SPECS Phoibos 100), at a primary energy of 900 eV. The incident and emission angles were both 45, and the overall resolution was of the order of 1.0 eV.

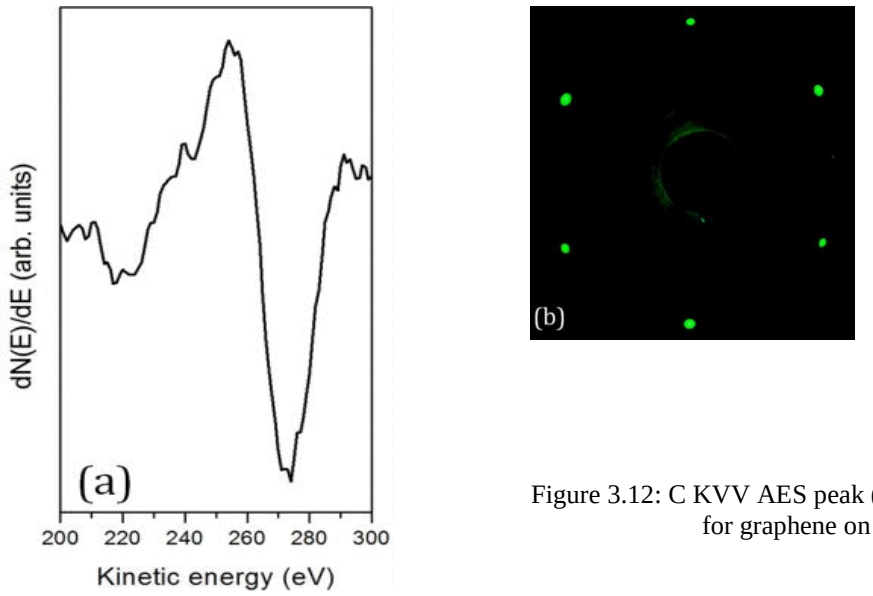

Figure 3.12: C KVV AES peak (a) and LEED pattern (b) for graphene on Ni(111).

After exposure to ethylene, the AES spectrum showed the typical KVV line shape due to sp^2 -hybridized carbon atoms [Figure 3.12 a], and the LEED pattern was undistinguishable from the clean Ni(111) one [Figure 3.12 b]. This is what is expected for a graphene layer adsorbed on Ni(111), because all carbon atoms can sit on high-symmetry sites of the substrate by stressing the C-C distance from 1.42 A˚ (the distance in pristine graphene) to 1.44 A˚ . The graphene growth is a self-limiting process: the highly reactive Ni(111) surface promptly dehydrogenates ethylene, but when graphene begins to cover the substrate, the sticking coefficient decreases until all the surface is covered by a single layer of graphene. At this point, the surface is completely passivated, and a second graphene layer cannot grow on the first layer, unless the surface is exposed to massive doses of hydrocarbons.[35]

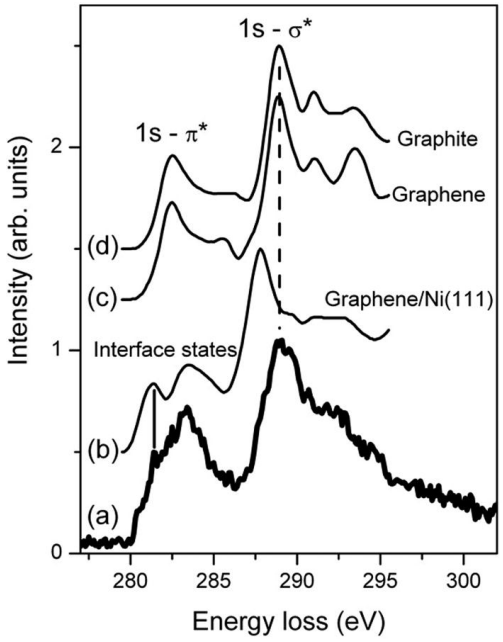

Figure 3.13: (a) The RELNES spectrum of the carbon K-edge measured on graphene/Ni(111). (b)–(d) First principle calculations for graphene/Ni(111), graphene, and graphite, respectively.

The energy loss spectrum measured on the graphene-covered Ni(111) surface showed the carbon K-edge superimposed on a smooth background. After polynomial background subtraction and smoothing, we obtained the RELNES spectrum shown in Figure 3.13 a, in which the two main peaks remind the $1s \rightarrow \pi^*$ and $1s \rightarrow \sigma^*$ structures typical of transmission ELNES spectra of graphene [150] and of reflection ELNES of graphite. [151] After the onset, which is located at 280.0 eV, the two main peaks are located at about 283 and at 289 eV, and also a shoulder on the left side of the first peak is present at 282 eV. In XANES measurements on graphite, the relative

intensities of the 1*s* → π* and 1*s* → σ* contributions are determined by the relative orientation of the graphite c-axis and the light polarization vector.[152] On the other hand, in reflection ELNES experiments on graphite, a similar selection rule exists, in which the role of the direction of the polarization vector is played by the direction of the momentum transferred in the energy loss process. By selecting the primary energy and the incident and analysis direction with respect to the surface normal (c axis), it is possible to enhance one of the two contributions with respect to the other. The same selection rule holds for a graphene layer adsorbed on the Ni(111) surface. [151] In our experimental arrangement, the momentum transferred has comparable perpendicular and parallel components with respect to the surface normal, which coincides with the c-axis of graphene. Thus, we do not expect a component of the RELNES spectrum to dominate on the other.

Figure 3.13 also shows theoretical ELNES spectra obtained by integrating the direction of the momentum transferred over the whole solid angle, for graphite, graphene, and graphene/Ni(111), reproduced from ref. [112] [curves (b), (c), and (d)]. The spectra of graphite and graphene are quite similar, showing the 1*s* → π* and 1*s* → σ* peaks in the same positions [curves (c) and (d)]. The interaction of graphene with the nickel substrate causes important changes in the theoretical spectrum [curve (b)]. The 1*s* → π* peak splits into two components, while the 1*s* → σ* peak suffers a shift of about 1 eV towards lower energy losses.

The comparison of our RELNES spectrum [Figure 3.13 a] with the theoretical spectrum [Figure 3.13 b] shows good agreement as regards the broad structure centered at about 283 eV. In fact, the shoulder we observe at about 282 eV has its counterpart in the first peak of the theoretical spectrum, as indicated by the vertical full line. Also the second peak at 283 eV is in good agreement with the calculated curve. The two peaks are attributed by Bertoni et al. to interface states at points K and M of the Brillouin zone. [112] On the contrary, the experimental 1*s* → σ* peak does not shift towards lower energy loss as predicted by the calculation, but its position corresponds to that predicted for graphite and graphene, as indicated by the vertical dashed line. The broad peak on the right side of the 1*s* → σ* peak in the theoretical curve seems to be reproduced by the corresponding shoulder in the experimental spectrum.

It is worth to mention that in their theoretical work, Bertoni et al. considered three epitaxial structural models, which differ in the positions of the carbon atoms with respect to the surface nickel atoms, and that the most probable structure was determined as that with the lowest energy.[112] Such structure, in which carbon atoms are located on top of first layer nickel atoms and in the so-called *fcc* hollow sites above third layer nickel atoms (the so-called top/*fcc* adsorption model), was used for the calculation of the ELNES spectrum. Recently, various investigations made with different methods have shown that this conclusion has to be revised. In 2011, Zhao et al. observed the coexistence of two adsorption geometries by high resolution X-ray photoelectron spectroscopy supported by density functional theory studies.[153] Successively, Bianchini et al. in their scanning tunnelling microscopy (STM) investigation showed that graphene on Ni(111) is made of coexisting domains with different coordination with respect to the substrate, and that the transition between adjacent domains occurs with distortion of the honeycomb structure, or with sharp edges.[154] Parreiras et al. in another multi-technique approach [155] tested six configurations of graphene on Ni(111), and concluded that a coexistence of different geometries is possible, although they exclude the top/*hcp* geometry observed by STM. [154] Moreover, STM measurements show that the top/*fcc* geometry is predominant with respect to the other observed geometries; then, it is reasonable to compare our RELNES result with the spectrum calculated on the basis of that model. However, the comparison should be made with a calculation made taking into account that the surface is covered by domains of graphene with different coordination with respect to the surface.

The shoulder located at 282 eV could also have another origin. ELNES measurements performed in the transmission mode with a high spatial resolution on graphene obtained by mechanical exfoliation of graphite show that carbon atoms located at the edges of graphene flakes give a spectrum in which the π^* peak intensity is reduced, and a new peak appears on its low energy loss side.[150] Therefore, the shoulder we observe at 282 eV could partially originate from the contribution of graphene-edge carbon atoms. However, the $1s \rightarrow \pi$ peak splitting in ELNES-TEM measurements is associated with single- and double-coordinated carbon atoms in suspended graphene, that are not terminated by –OH and –COOH groups, differently from what is generally accepted.[156] The chemical environment around such carbon atoms is very different from that existing around edge atoms of graphene patches on Ni(111), that are bonded

to the substrate through hybridization of the π orbitals with Ni d electrons, and to carbon atoms of side patches or possibly to –OH and –COOH groups. Therefore, we suggest that the observed splitting of the 1*s* → π peak is due to the graphene/Ni(111) interface states.

3.7 Conclusions

In conclusion, the electronic structure of the graphene/Ni(111) system has been studied by AREELS. We found that the interaction between graphene and Ni substrate contributes to form a new distinctive density of states at the Fermi level. We assign the low energy loss peak measured in our AREEL spectra to a collective excitation of the charge density associated to these states. The plasmon square-root dispersion shows that the character of the fluctuating charge is strictly 2D. The Fermi velocity is just a factor of 0.5 lower than in isolated graphene, making strongly interacting graphene an unexpectedly good candidate for ultrafast applications in the nanoelectronics and nanoplasmonics fields.

In the second part, angle-resolved EELS experiments allowed us to study in detail the electronic collective properties of the graphene/Ni(111) system in the low range of the interband transitions. We reassign the "π" plasmon to transitions between interface states resulting from the graphene/Ni hybridization. Although the interface states responsible of such excitation are the consequence of a strong interaction with the substrate, the charge density associated to these states also exhibits strictly 2D collective properties.

In the last part, we have shown that electron energy loss in the reflection mode is a powerful tool for the study of graphene supported on thick substrates. We have compared our results with the only available calculation, although recently published results show that the adsorption model on which such calculation is based should be partially revised. The comparison shows a good agreement, apart from a shift of the σ* peak. We observed the contributions in the energy loss spectrum related to the empty states due to hybridization at the graphene/nickel interface. ELNES in the transmission mode has the advantage of making possible a spectroscopic characterization with a high lateral resolution, but in the case of thin layers adsorbed on the surface of thick substrates, RELNES is a valid tool to gain information about the electronic structure above the Fermi level.

CHAPTER FOUR

SILICENE

4.1 Silicene on Ag(111)

Since the discovery of silicene several independent studies of the growth of silicene on the Ag(111) surface have revealed the existence of different ordered phases such as (4 × 4), ($\sqrt{13} \times \sqrt{13}$)R13.9° and ($2\sqrt{3} \times 2\sqrt{3}$)R30° [11–13,40–42]. These superstructures are indexed with respect to the Ag(111) unit cell. The different orientations of the same silicene sheet relative to the Ag(111) surface can be obtained by varying the substrate temperature during the silicon growth [159]. A simple method is commonly used to synthesize silicene on Ag(111). By heating a piece of Si wafer up to more than 1373 K, Si atoms are deposited onto the clean Ag(111) substrate. A deposition rate of 0.01–0.1 ML/min is usually used, where 1 ML is corresponds to a full coverage of Si atoms on the substrate surface. The precise control of the substrate temperature is a key to crystalizing Si atoms to form the honeycomb lattice. The temperature should be kept in the range from 473 to 600 K, above 620 K, the silicene layer is not formed.

The emergence of various structures originates from the flexibility of the Si–Si bond. The Si–Si bond in silicene has a mixed character of both sp^2 and sp^3 hybridization so that the local configuration has a high degree of freedom in both the bond length and the bond angle as a function of the mixing. Although structures are often observed for graphene grown on metal substrates, these structures are not due to the buckling but they are derived from the moiré patterns [44–48].

The 4×4 structure is obtained with a substrate temperature around 200 °C. The structure has been surveyed most intensively, partly because it emerges as a single phase with a larger domain size suitable for macroscopic measurements. The STM image of the 4×4 structure shows six protrusions in the unit cell, together with a corner hole, as shown in Figure 4.1. The STM image alone is insufficient to conclude that the Si atoms construct a honeycomb lattice in the 4×4 arrangement.

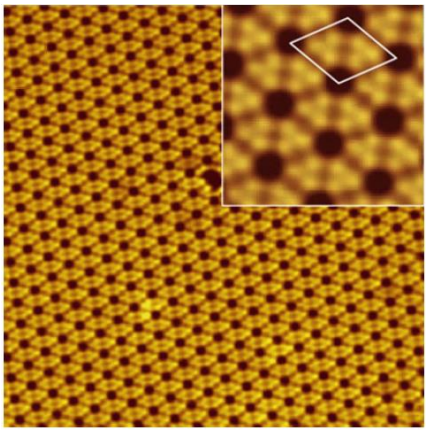

Figure 4.1: STM topographic image of the 4×4 structure grown on Ag(111) taken at 6 K The inset shows a high-resolution image. The white rhombus is a unit cell of the 4×4 structure

Two structural models have been proposed using a combination of STM experiments and DFT calculations. One is the model presented independently by Lin et al. [49] and Vogt et al. [50], and the other is the model proposed by Feng et al. [47]. Figure 4.2 shows these models.

The model proposed by Lin et al. and Vogt et al. contains eighteen Si atoms to form the honeycomb network. Six of these Si atoms are shifted upward relatively to the plane composed of the remaining twelve Si atoms. There is a hexagon at the corner of the unit cell. These features nicely explain the STM image consisting of six protrusions together with the darker hole. Meanwhile, Feng et al. presented a different model based on essentially the same STM image that was observed by Lin et al. and Vogt et al. The model of Feng et al. is composed of hexagons as building blocks, which form a 2D lattice. This model is matched with the one built by removing hexagons at the corner of the unit cell in the model of Lin et al. and Vogt et al. Thus, there exist Si atoms having dangling bonds and they are terminated with H atoms in the model of Feng et al. In this regard, the model of Feng et al. can be considered as a sort of 2D Si-hydride. This model also reproduces the STM image according to the DFT calculations of Feng et al. Since the STM image generally reflects both geometric and electronic structures, it is not straightforward to determine the geometric structure from the image even with the support of DFT calculations. Atomic force microscopy (AFM) has been used to directly visualize the atomic arrangement in the 4×4 structure [41,49]. The AFM image taken in non-contact mode looks very similar to the STM image, and additional information is not provided about the geometric structure. These results indicate that different approaches are required to determine the 4×4 structure.

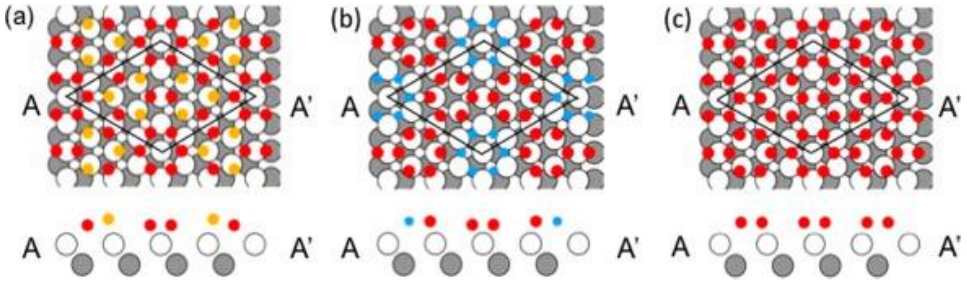

Figure 4.2: Structural models of the 4×4 structure. (a) Model presented by Lin et al. [49] and Vogt et al. [50]. (b) Model presented by Feng et al. [47]. (c) Low-buckled model in which a freestanding buckled silicene is placed on Ag(111) by tuning the lattice constant to match with that of the substrate. The gray circles is Ag atoms, the red and yellow circles represent Si atoms and smaller blue circles in (b) are H atoms.

Diffraction techniques are the most powerful and reliable for structure determination in a broad range of fields from materials science to biology. In surface science, LEED has been most successfully used to determine many surface structures from the clean surfaces of single crystals to complicated surfaces accompanied by long-range reconstructions [166].

The √13×√13R13.9° is obtained after deposition at a substrate temperature around 250 °C [167]. The atomically resolved STM images of the (√13×√13)R13.9° system show two types of structures. The (√13×√13)R13.9° type I and type II structures are shown in Figure 4.3 (1) and (2), respectively. The observation that under similar tunneling conditions, the unit cell of the (√13×√13)R13.9° type II is composed of four protrusions per unit cell, whereas that of the (√13×√13)R13.9° type I structure is composed of only one protrusion. This is confirmed by the DFT calculations [41,53]. Within the unit cell, the relative positions of the Si and Ag atoms are very different between the type I and type II structures leading to very different out-of-plane coordinates.

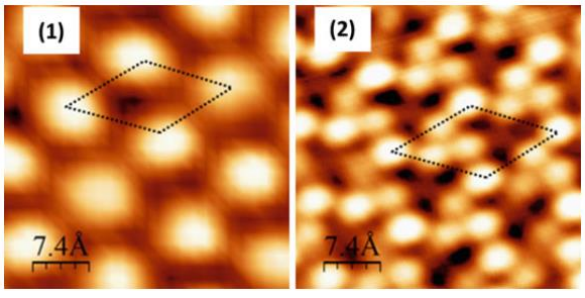

Figure 4.3: Atomically resolved STM images corresponding to the (√13×√13)R13.9° (V = -1.5 V, I = 0.2 nA) for (1) type I, and (2) type II. The corresponding unit cells are shown with dotted lines. [167]

Three-dimensional models for the type I and type II structures were investigated in the earlier DFT calculations [41,53]. They found that the type I and type II structures correspond to orientations of 5.2° and 33° relative to the (111) surface, respectively. These results indicate that two different configurations co-exist with different atomic positions. In other words, small changes in the buckling of the silicene modify the observed structure.

A continuous two dimensional (2D) sheet of silicene with a large area of an almost defect free honeycomb structure presenting a $(2\sqrt{3}\times2\sqrt{3})R30°$ structure on the Ag(111) surface, was observed for the first time by Scanning Tunneling Microscopy (STM) [56]. Subsequent claims that the STM image of $(2\sqrt{3}\times2\sqrt{3})R30°$ did not correspond to a silicene layer but to a bare Ag(111) surface due to a contrast inversion [57] (a graphically inverted image or to a tip effect) can be ruled out by the STM observations. Figure 4.4 (1) and (2) show the STM images obtained, respectively, on the bare Ag(111) substrate, and after the deposition of one silicon monolayer giving rise to a $(2\sqrt{3}\times2\sqrt{3})R30°$ superstructure. The atomic resolved STM images reveal a highly ordered silicon honeycomb lattice structure (Figure 4.4 (2)).

You can see clearly that the basal chains of the honeycomb silicene sheet are rotated by an angle of $(30-19.1)° = 10.9°$ with respect to the axes of the Ag(111). This matches very well the expected rotation for a $(2\sqrt{3} \times 2\sqrt{3})R30°$ structure. In the case of an inversion of contrast of the STM image of bare silver, the angle between the observed honeycomb structure, and that of the bare Ag(111) would be 0° and not 10.9°. In Figure 4.4 (3), the line profile along line (A) gives a lateral Si–Si distance of 0.2 nm, and a height difference between neighbouring Si atoms (buckling) of 0.02 nm. This can be compared to the corrugation of the bare Ag(111) surface, which is 10 times smaller (0.002 nm).

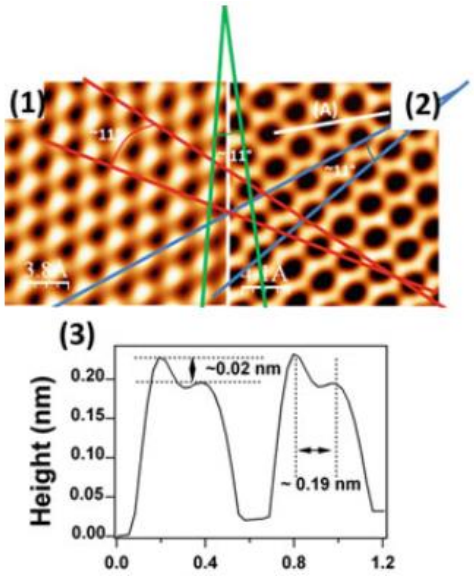

Figure 4.4 (1) Filled-state atomically resolved STM image of the clean Ag(111) surface. (2) Filled-state atomically resolved STM image of the same sample (without any rotation) after deposition of one silicon monolayer. (3) Line-profile joining neighboring Si atoms along the direction (A) indicated in (2). [168]

The most crucial puzzle that needs solving for this system is whether the honeycomb structures of silicene formed on Ag(111) host the Dirac fermions and specifically what evidence provides the most convincing answer? In graphene, the most convincing evidence is the anomalous quantum Hall effect (QHE) that is essentially different from the QHE observed in a conventional 2D electronic system [54–56]. In contrast to the integer QHE observed in a conventional 2D electron gas, the half-integer QHE is observed for graphene. The difference comes from the fact that an electron in graphene obeys the relativistic Dirac equation while the normal electron obeys the Schrödinger equation.

In general, when an external magnetic field is applied to condensed matter, the orbital motion of the electron is quantized because a parabolic potential well generated by the magnetic field confines the electron. The continuous energy spectrum of a free electron is quantized into discrete Landau levels (LLs). The energy eigenvalues of the LLs for the conventional 2D system are described as:

$$E_n = \hbar\omega\left(n + \frac{1}{2}\right) \qquad (7.1)$$

where $\omega = eB/m$ is the cyclotron frequency of an electron with mass m and charge e, $\hbar$ is Plancks constant divided by 2π, B is the external magnetic field perpendicular to the system and

n is the quantum number [4]. The energy spectrum is the same as that of a harmonic oscillator and the energy separations between the consecutive LLs are constant with *n*. On the other hand, the energy spectrum for the Dirac fermion is described as:

$$E_n = \pm v_F \sqrt{2e\hbar Bn} \qquad (7.2)$$

where v_F is the Fermi velocity [4]. In contrast to the conventional 2D case, the energy separations between the consecutive LLs are not constant with *n* because the energy is proportional to $\sqrt{n}$. Thus, the spectral evolution of the LL sequence as a function of magnetic field enables us to distinguish which type of electron exists. Measuring the linear electronic band structure also presents a signature of the Dirac fermion. Angle-resolved photoelectron spectroscopy (ARPES) has been widely used to investigate the electronic band structure. In the ARPES experiments, the kinetic energy of photoelectron is measured as a function of the momentum and then we can determine the band dispersions experimentally. For the graphene, the crossing of the linear bands at the K point in the Brillouin zone near the Fermi level has been observed [57,58], which gives strong support for the existence of the Dirac fermions. Thus, the observation of the half-integer QHE and/or the unique LL sequence together with the linear band dispersion is desired for the silicene on Ag (111) to confirm the existence of the Dirac fermion.

Silicene on Ag(111), which is the best studied case, displays the particular property of forming a manifold of allotropic structures, depending on the growth temperature and Si coverage [12,42,59]. These honeycomb structures have a similar in-plane atomic geometry, with interatomic distances close to those expected for free-standing silicene. They differ with respect to the registry relations to the substrate, out-of-plane atomic buckling, and surface periodicity. Scanning tunneling microscopy (STM) and low-energy electron diffraction (LEED) report silicene structures with (4×4), ($\sqrt{13}\times\sqrt{13}$)*R*13.9°, and ($2\sqrt{3}\times2\sqrt{3}$)*R*30° periodicity compared to the Ag unit cell, besides minor phases observed in the early growth stages [12,59].

Total-energy electronic structure calculations derive structural geometries in good agreement with the STM experimental observations [174]. The theoretical results also show that the silicene allotropes are nearly degenerate, with cohesive energy between Si and Ag in the

range of a weak covalent bonding, accounting thus for their coexistence under most or all growth conditions [59,60].

A key question regarding the fundamental and applicative properties of silicene is whether the presence of Dirac fermions is preserved on a supporting substrate. Studies aiming to establish to what extent silicene on Ag(111) retains the electronic structure of free-standing silicene were mainly focused on the (4×4) structure. Early ARPES data have been interpreted as providing evidence for linearly dispersing bands close to E_F, [61,62] like the Dirac cones in graphene. Experimental [36,39,63] and theoretical [36,39,64–66] investigations have more recently demonstrated that this assignment is not correct, since the spectral features of the (4×4) structure originally interpreted as silicene bands derive from bulk and interface Ag states. These studies show that the π-symmetry states become delocalized due to the hybridization with the substrates, lose the 2D honeycomb character, and do not form Dirac cones. The σ-bands turn out to be less interacting and moderately affected by the substrate [39,67].

The effect of the electronic interaction with the substrate for the (√13×√13)*R*13.9° and (2√3×2√3)*R*30° structures is largely unexplored. While the (√13×√13)*R*13.9° structure has not been examined yet by ARPES, a recent study addressed the (2√3×2√3)*R*30° structure [182], but the absence or presence of the Dirac cone was not established. Contrary to the (4×4) structure, ARPES results on the (2√3×2√3)*R*30° phase find a manifold of σ bands shifted much closer to E_F than in free-standing silicene, besides the formation of an interface state with energy similar to the one observed on the (4×4) structure [182]. These observations raise therefore the question whether and to what extent silicene allotropes on Ag(111) present dissimilar electronic properties.

Very recently, Sheverdyaeva *et al* [183] compare the electronic structure of (4×4), (√13×√13)*R*13.9°, and (2√3×2√3)*R*30° silicene monolayers on Ag(111) by means of ARPES and first-principles calculations. They find that all phases display similar Ag-derived interface states and σ bands weakly perturbed by the substrate interaction. Intense spectral features, including those previously attributed to σ band emission from the (2√3×2√3)*R*30° structure, are found to originate from umklapp replicas of the Ag interface state and Ag sp-bulk bands. All the examined silicene allotropes do not display the characteristic Dirac cones of free-standing

silicene, proving that the π bands are strongly modified by the interaction with the substrate bands independently of the structural detail of the allotrope.

Here we show a study of the $\left(2\sqrt{3}\times 2\sqrt{3}\right)R30°$ phase and of the phase made of (4×4), $\left(\sqrt{13}\times\sqrt{13}\right)R13.9°$, $\left(2\sqrt{3}\times 2\sqrt{3}\right)R30°$ coexisting phases.

All the measurements were performed in ultra-high vacuum (UHV) chamber operating at a base pressure of 2×10^{-10} mbar. Ag substrate (a disk about 8*mm* diameter, Figure 4.5) was cleaned through several cycles of Ar^{+} ion sputtering and annealing at 500℃ until a sharp LEED pattern showed the achievement of a clean and well-ordered Ag(111) surface, as confirmed by the LEED patternd and by the XPS spectrum (Figure 4.6 and Figure 4.7).

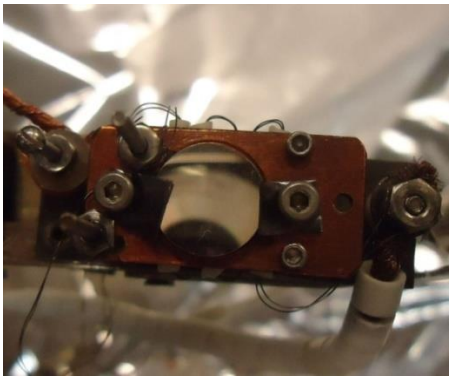

Figure 4.5**:** Ag(111) sample (8mm diameter) mounted on the sample holder

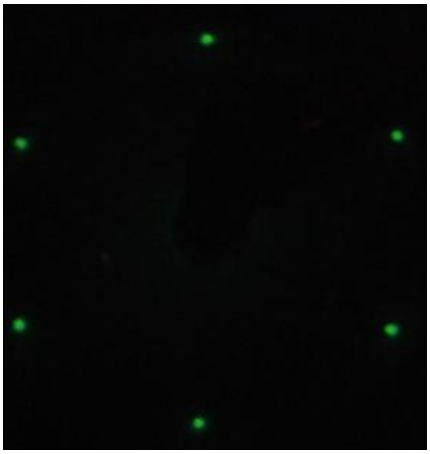

Figure 4.6: LEED pattern of the clean Ag(111) sample

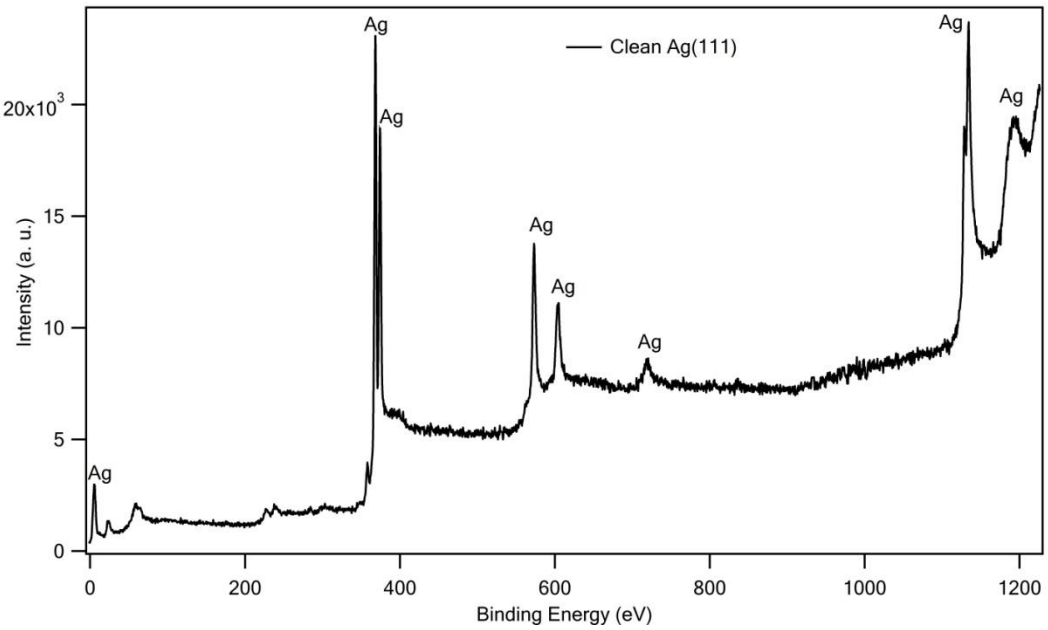

Figure 4.7: XPS spectrum of clean sample of Ag(111) substrate surface

The deposition of Si was carried out by direct heating of a Si wafer piece placed a distance of about 10 cm in front of the sample. We used a heating current of 8 A to evaporate Si while the substrate temperature was fixed at different values and controlled by a thermocouple.

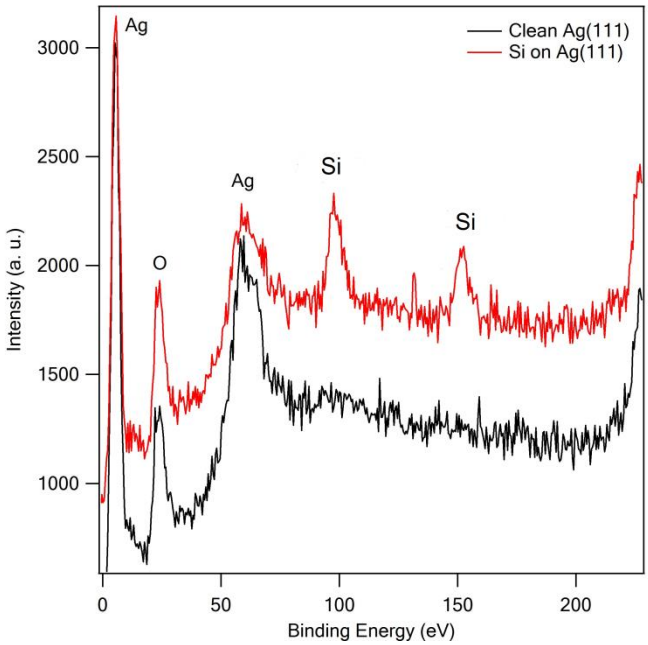

Figure 4.8**:** XPS spectra obtained after silicon deposition (red curve) and for clean Ag(111) substrate (black curve).

Figure 4.8 shows the XPS spectra obtained after the silicon deposition. At a substrate temperature substrate 270 °C during deposition, we observed the coexistence of the silicene phases (4×4), $\left(\sqrt{13} \times \sqrt{13}\right)R13.9°$, $\left(2\sqrt{3} \times 2\sqrt{3}\right)R30°$ (Figure 4.9 (a)). By increasing the substrate temperature to 300 °C during the deposition, we observed a well-ordered $\left(2\sqrt{3} \times 2\sqrt{3}\right)R30°$ (Figure 4.9 (b)). Figure 4.9 shows the patterns obtained in ref. [48], that are very similar to those obtained in the present investigation, in which the spots associated to the different structures are shown. Similar LEED results have been obtained by Lalmi *et al.* [56], Moras *et al*. [173] and Jamgotchian *et al.* [184].

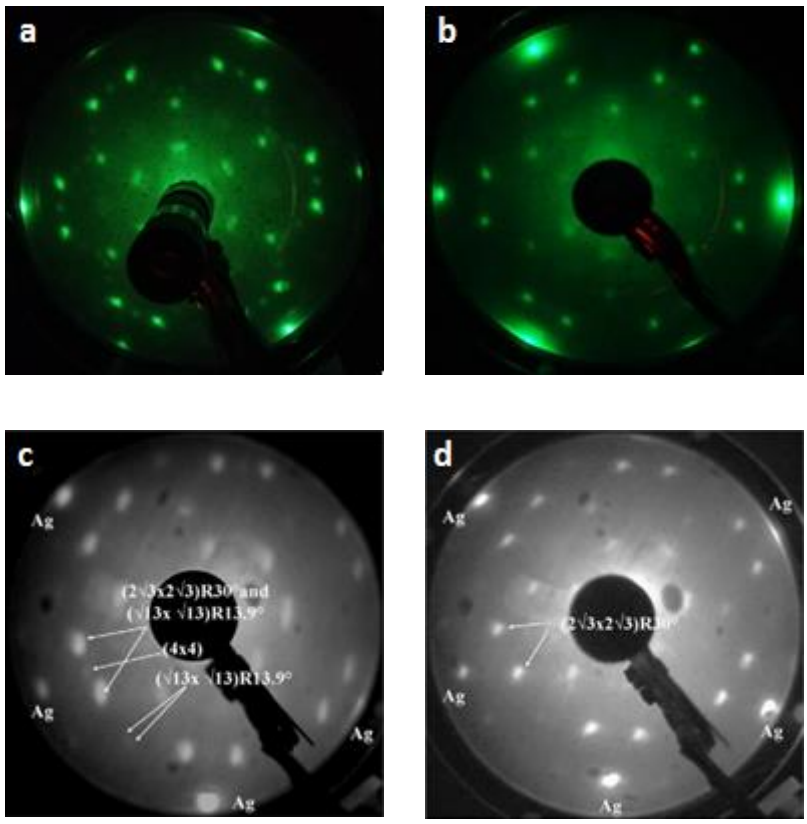

Figure 4.9**:** (a) (4×4), $\left(\sqrt{13} \times \sqrt{13}\right)R13.9°$, $\left(2\sqrt{3} \times 2\sqrt{3}\right)R30°$ and (b) $\left(2\sqrt{3} \times 2\sqrt{3}\right)R30°$ LEED patterns of silicene on Ag(111) taken at room temperature with the kinetic energy of 40eV. (c), (d), LEED patterns reproduced from Jamgotchian *et al*. [48].

Figure 4.10 shows the ordered arrangements of Si atoms on the Ag(111) surface which originate the LEED patterns observed [48].

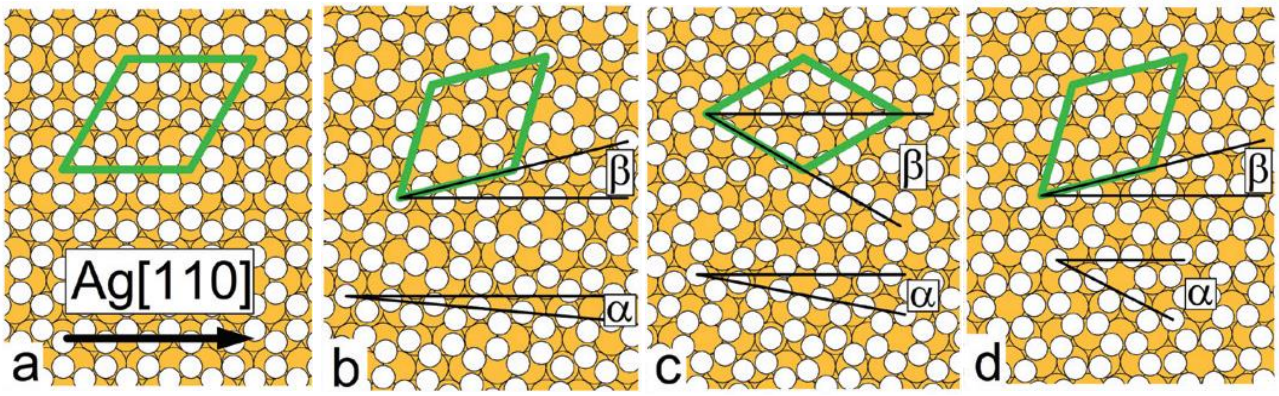

Figure 4.10: (a) Ordered arrangement of silicon atoms on the Ag(111) surface which give rise to the LEED patterns observed: (a) (4×4), $(b)\left(\sqrt{13} \times \sqrt{13}\right)R13.9°, \alpha = 5.2°, (c)$ $\left(2\sqrt{3} \times 2\sqrt{3}\right)R30°$ and (d) $\left(\sqrt{13} \times \sqrt{13}\right)R13.9°, \alpha = 27°$.

We have studied the clean Ag(111) and the two phases of Silicene on Ag(111) by Electron Energy Loss Spectroscopy. EELS experiments were performed by using a high resolution electron energy loss spectrometer. The incident electron beam was at fixed angle of $\theta = 45°$ with respect to the surface normal, with 40 eV kinetic energy. The energy resolution was tuned to 25 meV to improve the signal-to-noise ratio. The momentum transfer component parallel to the surface $q_{\parallel}$ was calculated by the following equation:

$$q_{\parallel} = (2m\,E_P/\hbar^2)^{1/2}\left[\sin\theta_i - (1 - E_i/E_P)^{1/2}\sin\theta_s\right]$$

where m is the mass of free electron, E_P the energy of the primary electron beam, E_i the loss energy, θ_i and θ_s the incident and scattering angles with respect to the surface normal, respectively.

Figure 4.11 **(**a) shows the EEL spectra for clean Ag(111) obtained by varying the analysis angle with respect to the surface normal. All spectra exhibit a well defined surface plasmon peak, located in the 3.7-3.9 eV loss range, which moves in energy with changing the analysis angle.

The energy position and width of each peak were determined after backgroud substraction, by a polynomial fit. The $q_{\parallel}$ trasferred for each EEL spectrum was calculated using the equation mentioned above. The values of the maximum of the energy loss of the peaks are

reported *vs* $q_{\parallel}$, as in Figure 4.11 **(**b), for the bare Ag(111) surface. The curve was fitted with a parabolic form:

$$\hbar\omega = k_0 + k_1 q_{\parallel} + k_2 q_{\parallel}^2$$

where $k_0 = (3.740 \pm 0.005)$ eV represents the energy loss due to the surface plasmon in the optical limit ($q_{\parallel} = 0$).

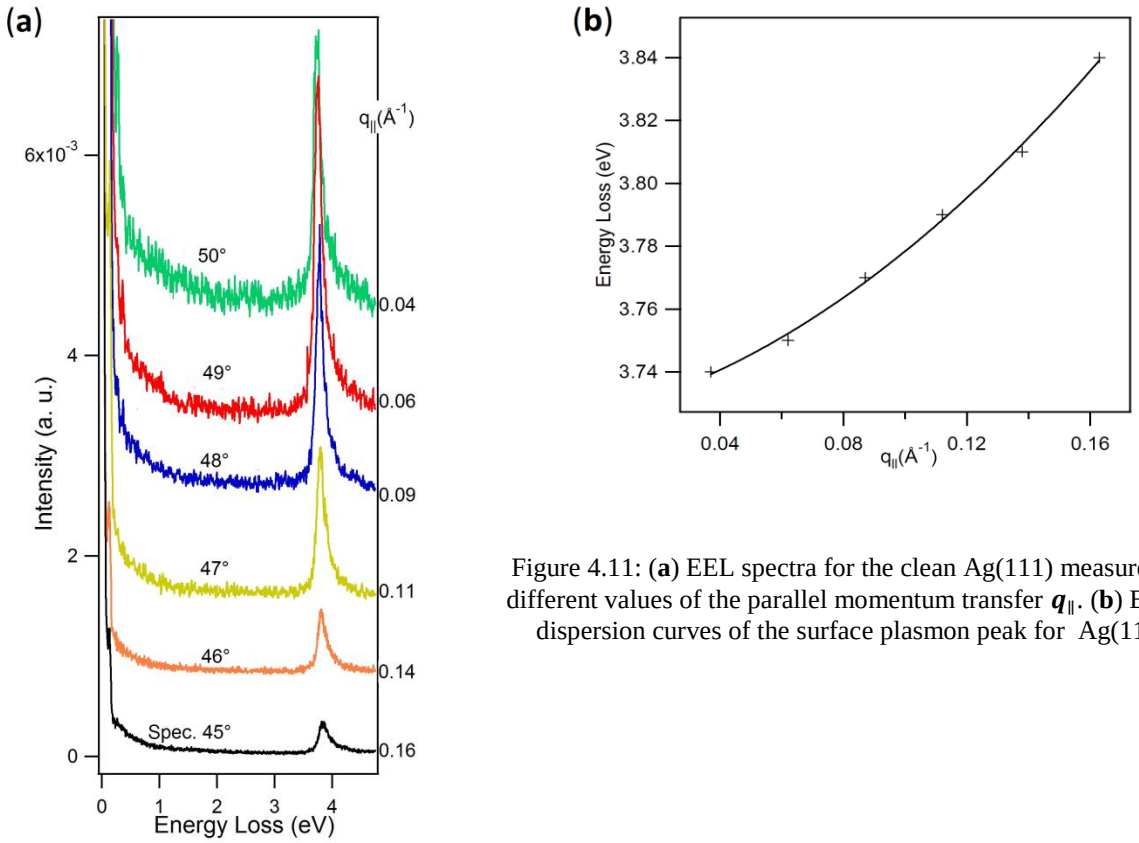

Figure 4.11: (**a**) EEL spectra for the clean Ag(111) measured for different values of the parallel momentum transfer $\boldsymbol{q}_{\parallel}$. (**b**) Energy dispersion curves of the surface plasmon peak for Ag(111).

It is evident from the data that the initial surface plasmon dispersion of Ag(111) is positive, in contrast to the negative initial slope found on all simple metals [17– 21]. The origin of such an effect is explained by the *s-d* polarization model [188]. In this scheme, the 5*s* electrons are treated as a *jellium system* and the occupied 4*d* bands are described in terms of a polarizable medium that screens the Coulomb interaction between the conduction electrons.

However, a part of the fluctuating plasmon charge is located outside the *d* electron medium due to the spill out of the *s* electron density and is not exposed to the *s-d* screening. This effect induces a frequency shift: at small values of $q_{\parallel}$, the plasmon field decays slowly and the shift is small, while with increasing $q_{\parallel}$ the plasmon field decays more rapidly, the *s-d* polarization becomes less effective and the blue-shift increases.

Then, the presence of *d* electrons modifies the properties of induced screening charge causing a different behavior of the Ag surface plasmon dispersion compared to that expected from the free electron model.

The deposition of Silicene in the different phases modifies substantially the EEL spectra with respect to the clean Ag(111) surface. Figure 4.12 shows the spectrum obtained on the (4×4, √13×√13R19°, 2√3×2√3R30°) phase.

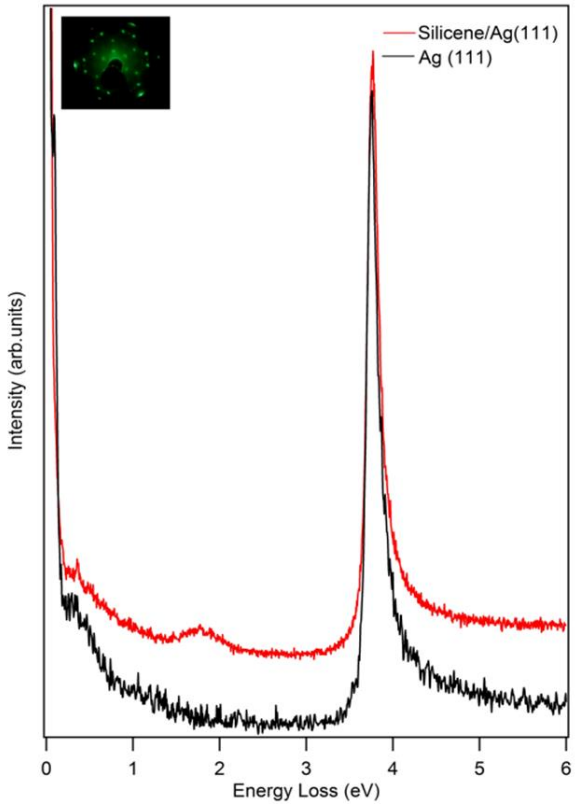

Figure 4.12: EEL spectra of the Ag(111) surface covered by Silicene in the (4×4, √13×√13R19°, 2√3×2√3R30°) phase (red curve). For comparison, the spectrum of the clean surface is also shown (black curve).

The presence of Silicene induces the appearance of a well-defined peak whose center is located at about 1.75 eV. Such peak does not change sensibly its energy with changing detection angle and then momentum transfer. In fact, the specular beam was no very well defined with respect to the detection angle, probably due to some kind of disorder in the mixed-phase Silicene layer. This fact did not allow us to define the momentum transfer in each spectrum, and thus also for detection angles out of the "nominal" specular direction, the dominant contribution to the spectra arise from loss processes with $q_{\parallel} = 0$. Nevertheless, the observation of the peak at 1.75 eV, which we attribute to a plasmon associated to the Silicene layer, remains a remarkable finding. In fact, such plasmon has never been observed in the literature.

The EEL spectrum changes when Silicene in adsorbed in the more ordered $2\sqrt{3}\times2\sqrt{3}R30^{\circ}$ phase. Figure 4.13 shows different spectra taken at different detection angles.

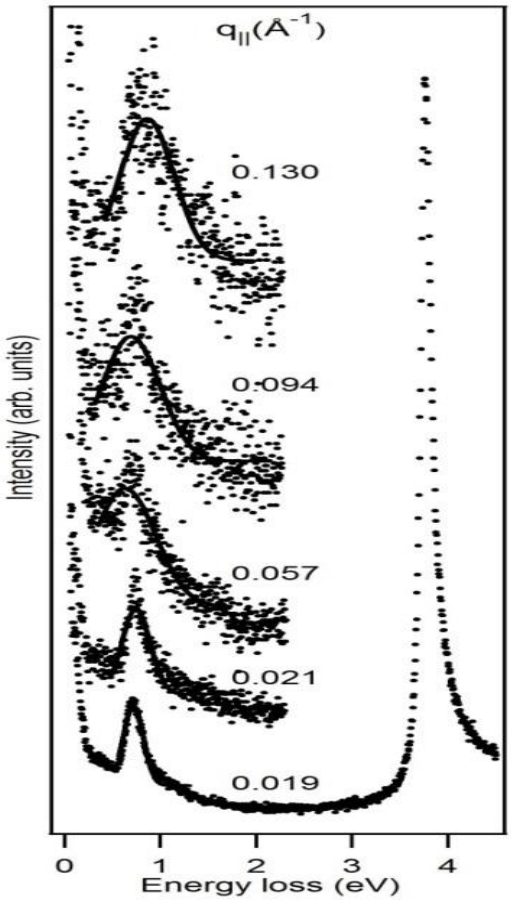

Figure 4.13: EEL spectra of the Ag(111) surface covered by Silicene in the $2\sqrt{3}\times2\sqrt{3}R30^{\circ}$ phase, obtained at different detection angles. The values of the momentum transfer relative to the loss at about 0.7 eV are shown.

The peak which is located at about 0.75 eV moves clearly towards higher energies with increasing momentum transfer. Figure 4.14 shows the dispersion relation obtained from such spectra. The typical parabolic dispersion confirms that the peak is due to a collective excitation which is evidently associated to the Silicene layer.

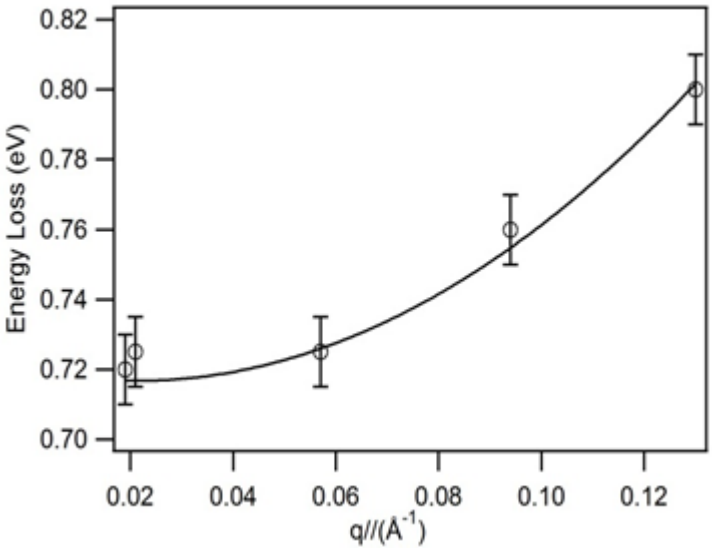

Figure 4.14: Dispersion relation obtained from the spectra shown in Figure 4.13

4.2 Conclusions

Our results show that the plasmonic properties of Silicene on Ag(111) are strongly dependent on the geometrical arrangement of Si atoms with respect to the substrate. We observe plasmons on both the (4×4, $\sqrt{13}\times\sqrt{13}R19°$,$2\sqrt{3}\times2\sqrt{3}R30^{\circ}$) phase and the $2\sqrt{3}\times2\sqrt{3}R30^{\circ}$ phase. The value of the plasmon loss energy obtained on the mixed phase corresponds surprisingly to the plasmon energy calculated recently for free-standing silicene [190]. Moreover, this finding is in disagreement with calculations of the dielectric properties of the silicene/Ag(111) system, in which it seems that the presence of silver causes a strong decrease and a shift of the plasmon loss peak [191]. More theoretical work is needed to clarify these points. Nevertheless, our results open a relevant question about the plasmonic properties of supported silicene.

CHAPTER FIVE

CARBON NANO-ONIONS

5.1 Carbon Nano-Onions

In 2001 Sano and co-workers reported the arc discharge synthesis of carbon nano onions underwater [1,2]. In this method, two high purity graphite rods were electrically arced under water by applying a bias potential of 16–17 V between them and maintaining a constant current of 30 A. During the synthesis, carbon nano onions were obtained as a floating powder on the surface of the water while other subproducts such as multi-walled carbon nanotubes precipitated to the bottom of the container (see Figure 5.1). Although it immediately may be presumed that the density of carbon nano onions is less than that of water, this is not the case. The density of carbon nano onions is far greater than water (1.64 g/cm^3) therefore the floating carbon onions on the surface of water is presumed to be due to the formation of large van der Waals crystals as described in the next section [192].

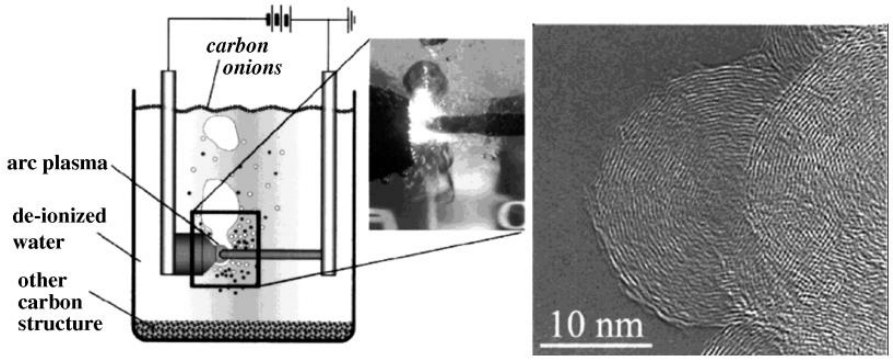

Figure 5.1**:** Scheme of the apparatus used for the arc discharge synthesis of CNOs. [192]

The arc discharge method offers an alternative to vacuum processes for the synthesis of larger carbon nano onions in reasonable quantities. In addition, the arc discharge method is considerably cheaper and simpler than other methods. Carbon nano onions obtained by this method exhibit diameters between 15 and 25 nm (20–30 shells). Xu and co-workers reported later that the mean carbon nano onion size is 40 nm, considerably larger than carbon nano onions obtained from nanodiamonds [193]. The UV-vis characteristic of these carbon nano onions exhibit remarkable similarities with the interstellar dust ultraviolet absorption spectrum which

has been widely studied and therefore the presence of carbon nano onions in dense interstellar clouds has been proposed [194].

Figure 5.2 shows a pictorial representation of the model used by Sano to explain the formation of carbon nano onions under water [192]. Sano proposed that during an arcing process a gradient of temperature exists which can be divided into multiple zones.

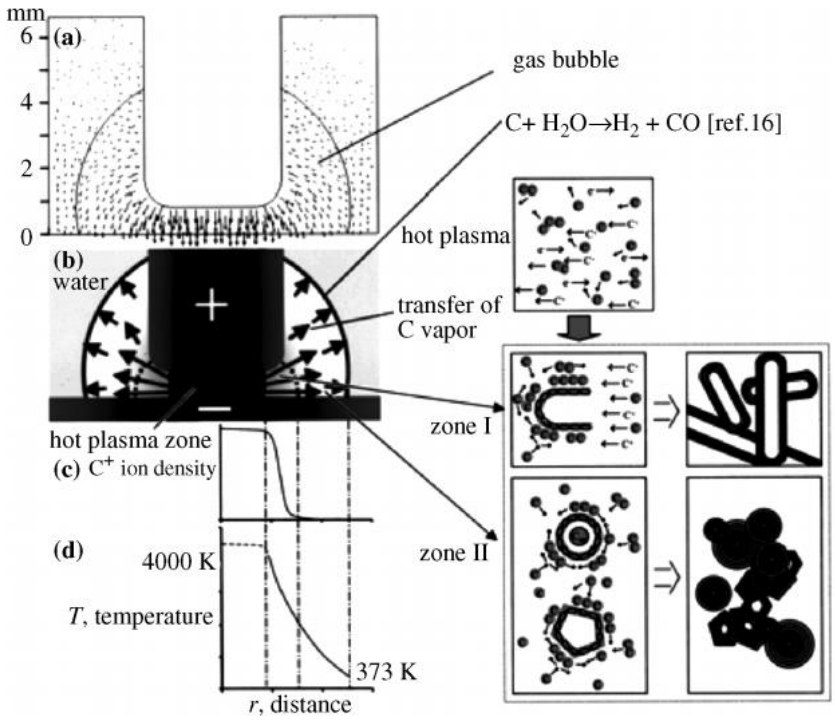

Figure 5.2**:** Suggested mechanism for the formation of carbon nano onions produced in water. (a) Direction of the electric field formed between the two electrodes. (b) Direction of thermal expansion from the plasma to water. (c) Ion density distribution as a function the distance from the plasma. (d) Gradient of temperature and formation of different nanoparticles. [192]

The Raman spectroscopy of these carbon nano onions shows the D (1344 cm^{-1}) and the G band (1569–1577 cm^{-1}), respectively. The ratio of the intensities of the D and G peaks is often used to estimate the degree of perfection of graphene planes. For example, the absence of the D peak in HOPG implies perfect graphene planes. Thus, a very weak D peak and a strong G peak from carbon nano onions signify that only slight imperfections are present in the graphene planes

of the onions [195]. There are many methods of synthesis of carbon nano onions have appeared in the literature.

Among all the methods published, annealing of nano diamonds and arc discharge under water of graphite electrodes offer optimal amounts of pure CNOs although their sizes differ considerably. Current research has therefore been directed towards the selective synthesis of small CNOs with regular size, since smaller CNOs feature larger surface areas and therefore are more reactive towards chemical functionalization. This was demonstrated by Echegoyen et al. who studied the differences between carbon nano onions obtained from arcing [A-CNOs] and from annealing of nanodiamonds [N-CNOs] [196].

The classical papers devoted to study carbon nano-onions by Raman data [5,7,8] showed that contrary to what can be thought, their spectra are very different with respect to fullerenes. Certainly, they resemble the spectra of graphene and graphite. This fact can be explained taking into account that the Raman spectra of fullerenes are dominated by a radial breathing mode and by the so-called pinch-pentagonal mode, linked with the vibrations of the atoms located in the vertices of pentagons in order to close the structure[199]. In nano-onions, as the number of shells increases, the number of pentagons, relative to the number of hexagons, decreases, and then the contribution of the pentagonal modes becomes smaller. At the same time, the existence of several shells, in interaction through the Van der Waals forces, provokes the disappearance of the radial mode. Eventually, the vibration modes of multi-shell nanoonions resemble those observed in curved graphene. The most important characteristic of the Raman spectra of nano-onions is the shift at higher energies of the first-order Raman-allowed mode (G band) due to the strain produced in the graphene planes by this curvature [5,8].

After the mentioned seminal papers [5,7,8], Raman spectroscopy has been used systematically as a tool for characterization of nano-onions mainly to distinguish the different products that participate in their synthesis as is reflected in Refs.[10–12], but in these papers there is no information about the fine structure of the spectra neither on their relation with the structure of the nano-onions.

It is important to remark that most of the information about Raman spectra of closed-shell carbon nanostructures refers to spherical nano-onions. In a recent work of Bogdanov et al. [81], there is an extensive Raman spectroscopy study of nano-onions produced by annealing of nano diamonds. In his work, Bogdanov includes not only the spherical nano-onions, but also the polyhedral variants of these nanostructures (polyhedral carbon onions) obtained at high annealing temperatures. However, there is no distinction there, about the features of the Raman spectra depending on the kind of onion.

As a matter of fact, the importance of polyhedral carbon onions has been increasing in the last years. They are the kind of material obtained in several experimental methods of preparation of nano-onions, as for example, the one based on a submerged arc discharge of graphite electrodes in water [192], a technique used to obtain nano-onions in the present work and a method frequently utilized for producing high-purity materials [202].

Codorniu Pujals *et al* obtained a typical Raman spectrum of the samples using underwater arc discharge method is displayed in Figure 5.3. The TEM image in the inset shows the polyhedral shape of nano-onions [203].

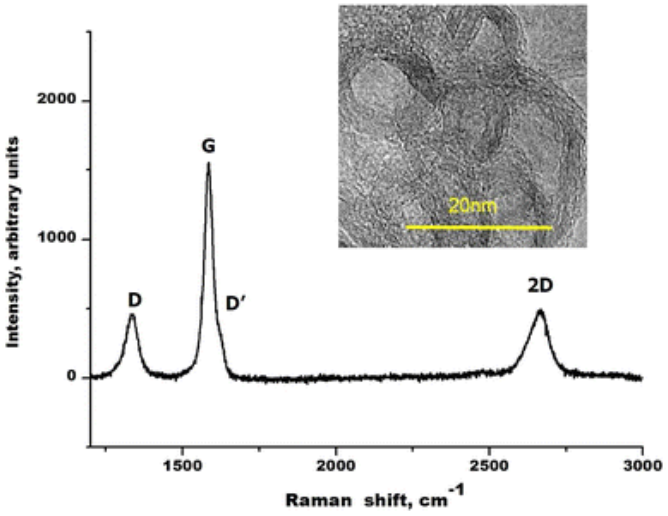

Figure 5.3**:** Raman spectrum of a sample containing polyhedral carbon onions. In the inset the corresponding TEM image is displayed. [203]

The polyhedral carbon onions spectrum contains the same features reported for graphene and graphite [204], characterized by the presence of three main bands. The first two bands correspond to one-phonon processes so-called firstorder Raman spectrum, the G band linked to a Ramanactive optic in-plane stretching mode (E_{2g}), and the D band, located at about 1580 and 1350 cm^{-1}, respectively. The presence of the D band in the spectra of graphite and graphene is due to defects in their crystalline lattice. In pristine samples of these materials, this band, due to the A_{1g} breathing mode of six-atom rings at K, is not allowed because of the fundamental Raman selection rule.

In the presence of defects, adding an electron-defect scattering event to the process allows to satisfy the overall momentum conservation [96]. In curved carbon structures, like nanotubes and nano-onions, the D band is always present. The third band of the spectrum, located near 2700 cm^{-1} and called 2D and corresponds to a two-phonon process involving phonons with opposite wave vectors.

Besides the three main bands, a small peak very close to the G band can also be observed. This peak is identified as the D′ mode and is also produced by a double resonance process activated by defects, but in this case only one Dirac cone of the electronic structure of graphene is participating instead of two which usually are involved in the case of the D band formation.

5.2 Synthesis of CNOs

We created a metallic structure, consisting of two stainless steel flanges held together by three threaded columns (Figure 5.4). The upper plate was drilled in the center to allow assembly of the micrometer that would allow a good accuracy of advancement of the anode towards the cathode. Therefore, the micrometer allows the translation towards the cathode during discharge, which is indispensable in maintaining the *gap* constant [12,13,19–23]. The lower plate, instead, is characterized by a ceramic zone which isolates it electrically from the rest of the chassis; the cathode stand, made of copper, was precisely mounted on this area.

Figure 5.4: Apparatus assembled to synthesis of CNOs by arc discharge in water.

A power supply was used, that allowed the achievement of current values between 0-70A, with a difference of potential between 0-24V; this is controlled by a toroidal VARIAC variable power transformer, see Figure 5.5.

The AC exiting the power supply and regulated by the transformer, then converted into DC power by a rectifier bridge.

Through the use of a tester and of a current clamp, we measured the potential difference before starting the discharge, as well as the value of the current once discharge has started. These readings result as being of fundamental importance in order to maintain a constant arc during the experiment, by acting on the micrometer regulating the translation of the anode. A thermocouple thermometer was fixed in the synthesis chamber to constantly monitor the temperature of water.

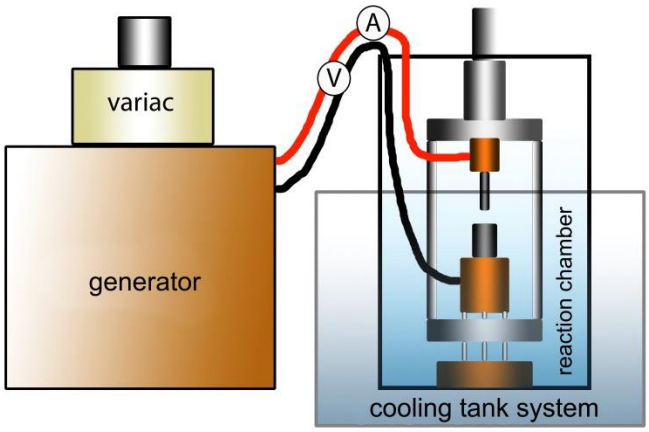

Figure 5.5: Diagram of apparatus for synthesis of CNOs by arc discharge in water.

Two graphite electrodes of similar purity of 99.99% (anode and cathode, 5 and 10 mm diameter respectively) cut to measure, were mounted on the chassis. Then we proceeded with the insertion in deionized water with a specific resistivity of 1.4 MΩ with a gap of 1 mm. The arc discharge was initiated by contacting the anode with the cathode (Figure 5.6), the discharge voltage was 15V.

The arc discharge in water was stable maintained anode-cathode gap of about 1 mm. The discharge can be characterized as an anodic arc as the smaller anode electrode is consumed.

The discharge proceeds until the almost total consumption of the anode, maintaining the synthesis chamber temperature under control: in our case, starting from a temperature equal to the ambient temperature (T=25°C) after approximately 70 seconds, a temperature of 83°C was reached, which was kept constant until the end of the discharge.

Figure 5.6: Digital image of the experimental process during arc discharge between anode and cathode of graphite.

During the discharge, in the plasmatic zone area on the cathode, a gradual deposition of material occurred, thus forming a small disk-shaped tablet as shown in Figure 5.7. In fact, it grew in correspondence of the center of the arc, and was in the maximum temperature zone. This assessment is essential to compare our results with those reported in the literature [12–14,24].

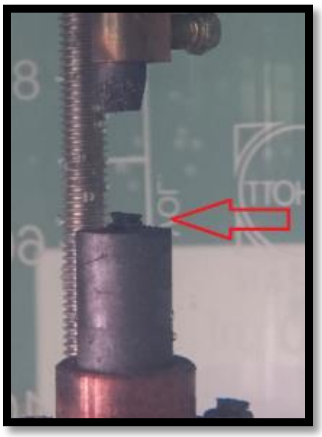

Figure 5.7: Discoid formed on the cathode during arc discharge.

Figure 5.8: Material gendered by arc discharge in the synthesis chamber.

Three sample groups were individuated from the synthesis chamber: powder floating on the water surface (S), the material precipitated on the bottom of water (B), and discoid formed on cathode (D).

The surface (Sp) and bottom (Bp) particles were sonicated for 3.5 h, in order to obtain a better dispersion of the carbonaceous material (Figure 5.9). After sonication, 2 phases of the material are presented: supernatant and precipitate; the precipitate material was heated to 80°C to evaporate water, thus the Sp and Bp samples were obtained.

Figure 5.9: Suspensions obtained after sonication of the three groups of material collected in reaction chamber: (a) from surface the reaction water, (b) collected on bottom of reaction water

The discoid sample (Ds) was divided to two pieces, one heated to 400 °C and the other without heating, then they have been converted to powder using a grinding machine, and the resulting powder materials of Ds were collected (Figure 5.10).

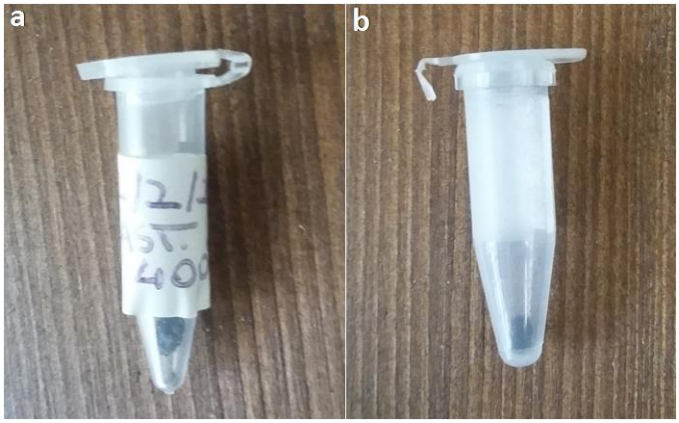

Figure 5.10: Agglomerates formed on the cathode, a) heated to 400 °C, b) without heating.

The samples of (Sp), (Bp) and (Ds) were characterised by microscopic and spectroscopic techniques. Transmission electron microscopy (TEM) was performed in JEOL Jem-2100, and Raman spectroscopy was made by using a Horiba-Jobin-Ivon Labram Raman spectrometer with a He Ne laser (632.8 nm) as excitation source.

TEM images reveal that the samples Sp and Bp are conformed by same CNPs, although they were obtained from different zones of synthesis chamber clearly showing the presence of carbon nano-onions (CNOs) and carbon nanotubes (CNTs) of various dimensions, and also some thin structures.

Figure 5.11 shows agglomerates of CNTs with CNOs surrounding. The CNOs present dimensions of the order of tens of nanometers and CNTs with diameters of the order of some nanometers.

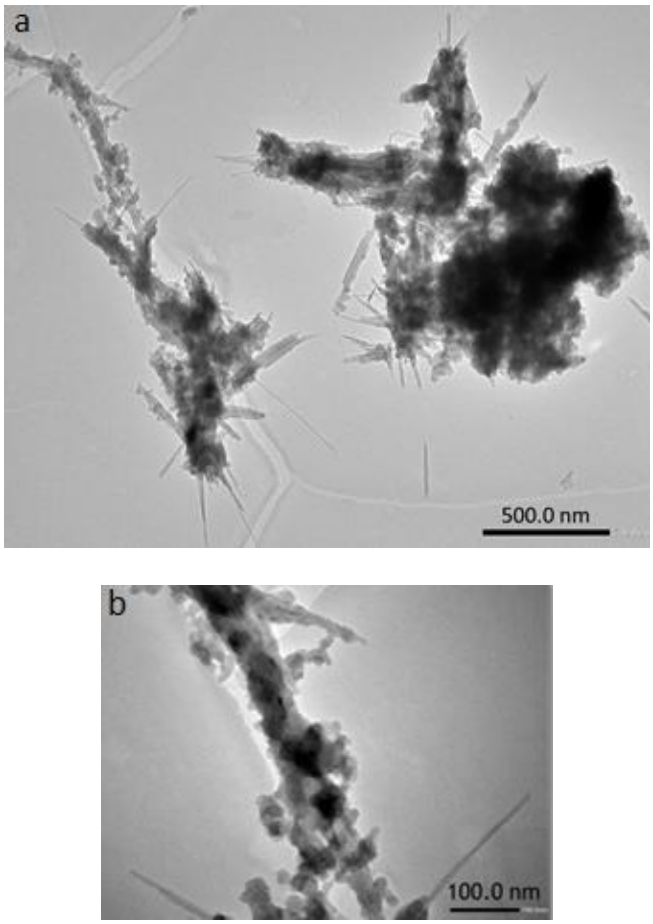

Figure 5.11: (a) TEM image shows agglomerates of different CNPs (CNT, CNO, lamellar structures). (b)Zoom image shows clearly agglomerates formed only of CNOs and CNTs

Moreover, other image reveals also the presence of some larger particles with order dimensions of hundreds of nanometers. Figure 5.12 evidences a CNO of high dimension ~ 640 nm, and its diffraction image acquired by select-area electron diffraction (SAED). It shows a pattern that can be attributed to a hexagonal structure with rotational disorder.

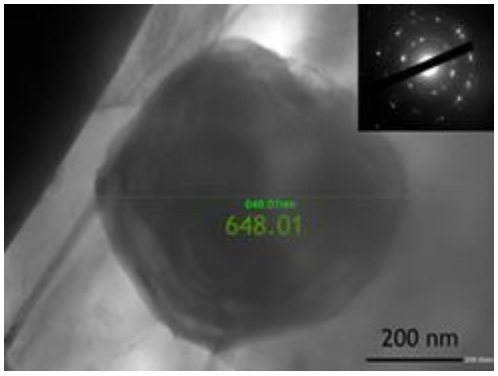

Figure 5.12: TEM image of a carbon-onion of high dimension and inset SEAD image.

Thin layered structures of extended dimensions also were found in the Sp samples. Figure 5.13 a shows structures with planar geometry that can be attributed to multilayer graphene. We observe also some structures in which graphene layer has lost the typical planarity showing a curved geometry (Figure 5.13 b).

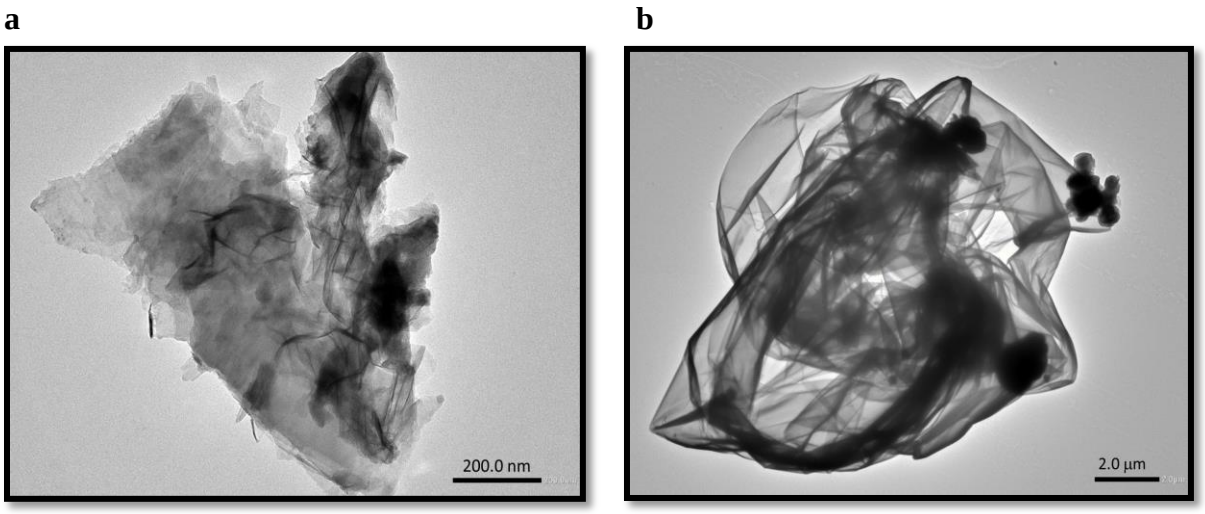

Figure 5.13: TEM images of (a) planar and corrugated fragments without evidence of CNOs and (b) clear corrugate structure of high dimension with low presence of CNOs.

Figure 5.14 shows typical zones contenting CNPs, distinguish structures attributable to nano-onions and nanotubes together with lamellar zones with a multilayer graphene aspect. While in Figure 5.15, CNOs with high dimensions (>100 nm) are present in isolated form, and finally in (b) we observe CNO surrounded of smaller CNOs with a diameter dimension around 10 nm.

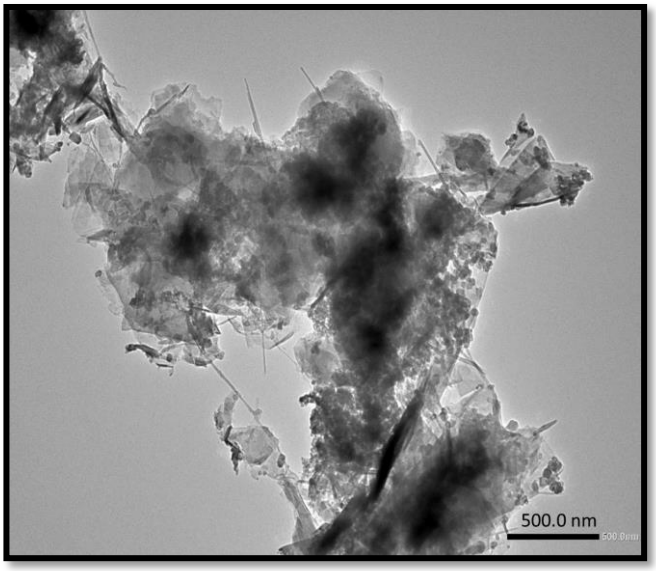

Figure 5.14: TEM images of carbon nanomaterials observed in Bp sample.

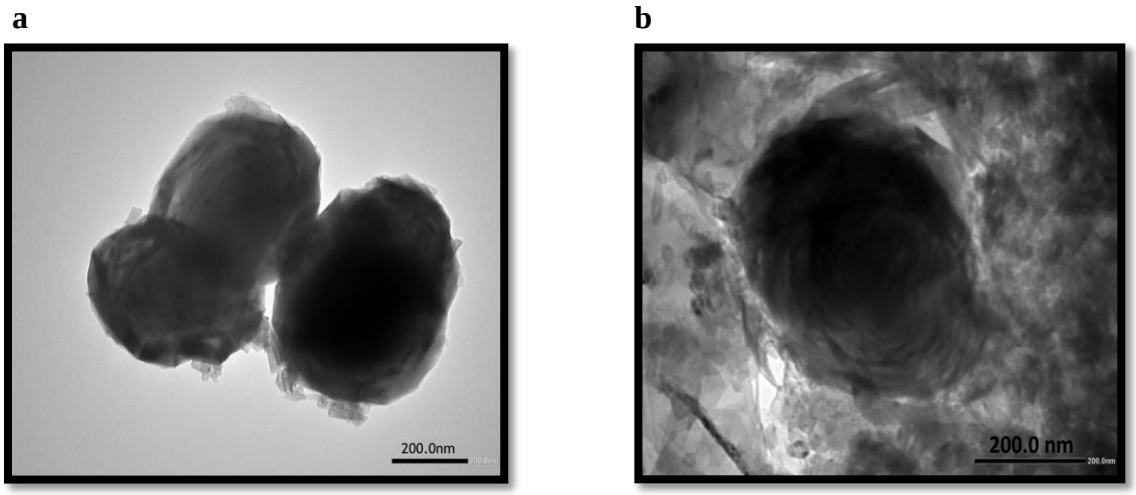

Figure 5.15: (a) image conteneting only CNOs of extended diameter observed in Bp sample. (b) CNO of extended diameter and sorrundimg of smaller CNOs.

The presence of CNTs with different diameters is evident in our nanomaterial. In Figure 5.16 both sample Sp (a) and sample Bp (b) show TEM images of CNTs always with CNO agglomerates, which present different dimensions and diameters.

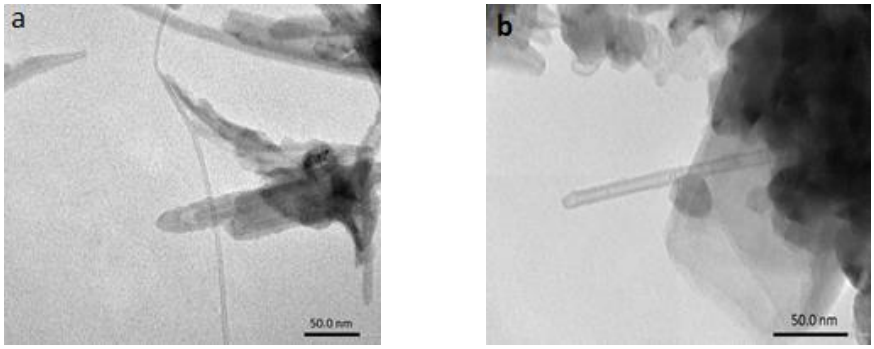

Figure 5.16: SEM images of CNTs produced during synthesis of CNOs by arc discharge in water. (a) Sp sample and (b) Bp sample.

The Raman spectrum from Sp samples is indistinguishable of the spectrum from Bp sample, and this is indicative of the fact that they are constituted by very similar carbon structures; therefore, we analyzed one Raman spectrum as representative for both samples.

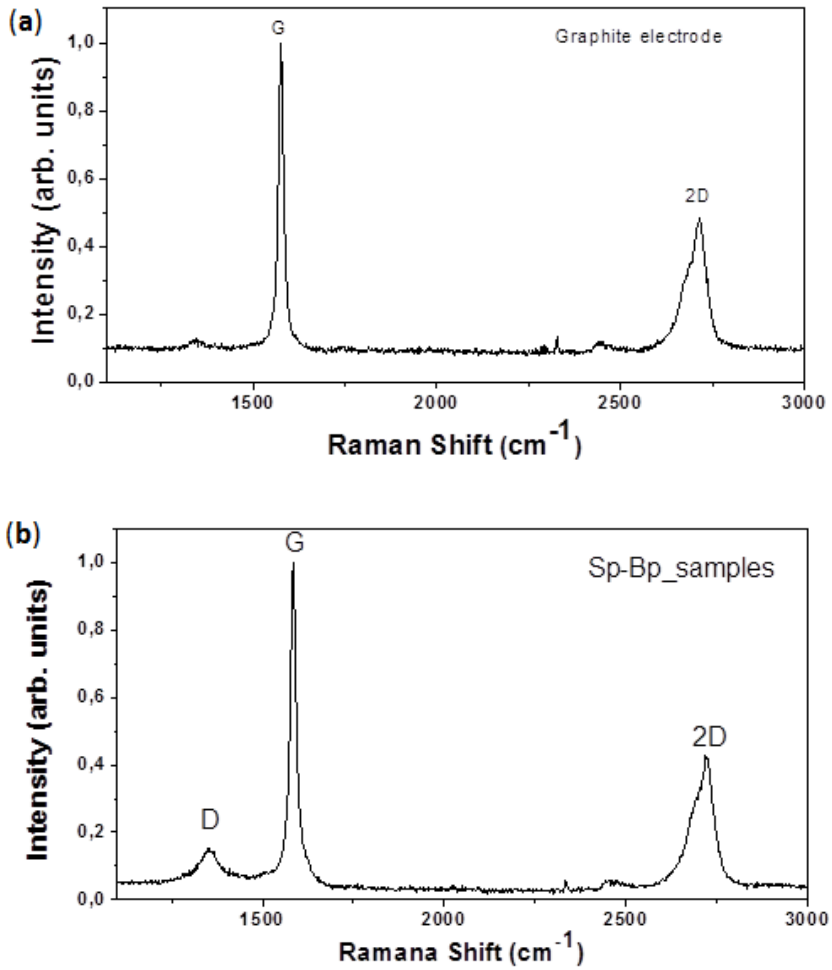

Figure 5.17: Raman spectra of graphite (a) and floating CNPs formed on surface (b).

The similarity between Raman spectra of Sp and graphite shown in Figure 5.17 suggests that the anode fragments play a decisive role in determining the shape of Raman spectra of Sp. Furthermore, such fragments show a structural disorder (defects, reduced flake dimensions) that is increased compared to the original material, as shown by the increased intensity of the D peak.

Different results respect to Ds are observed on samples obtained by the grinded dust of the solid discoid fragmentation formed in the plasmatic zone. The TEM characterization of Ds sample (Figure 5.18), shows the presence of fragments consists a large proportion of CNOs with dimensions estimated at tens of nanometers. In contrast, the CNTs have become more reduction comparing with previous TEM results of Sp and Bp.

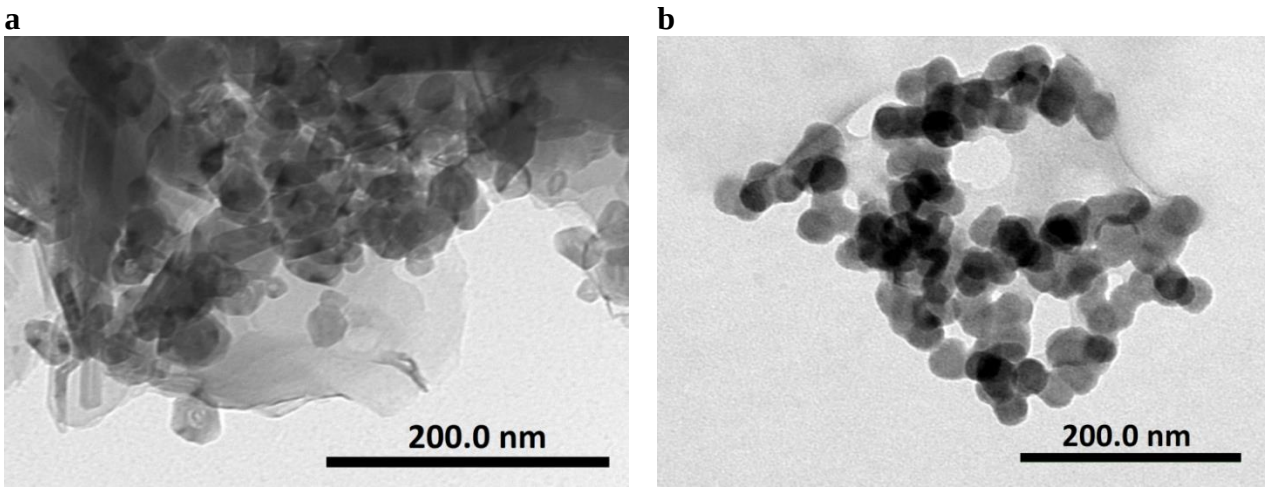

Figure 5.18: a) TEM image shows agglomerates of different CNPs (with more amounts of CNOs). b) Image shows clearly agglomerates formed only of CNOs.

The best results have been obtained when we heated a part of the discoid fragment at 400°C, and then grinded by a vibratory micro-mill machine (Fritsch Pulverisette 0) to obtain fine powder of the CNPs. The TEM characterization of this sample (Figure 5.19), shows the presence of fragments consisting exclusively of CNOs. More precisely, we have been observed in some fragments a polyhedral structure of CNOs with dimensions estimated at tens of nanometers.

This is a completely new finding, showing that the discoid formed in the plasmatic zone only needs to be grinded to get a nanomaterial made only of CNOs, without the need of

purification methods, as it would be necessary to obtain CNOs from the nanoparticles found on the surface or at the bottom of the vessel.

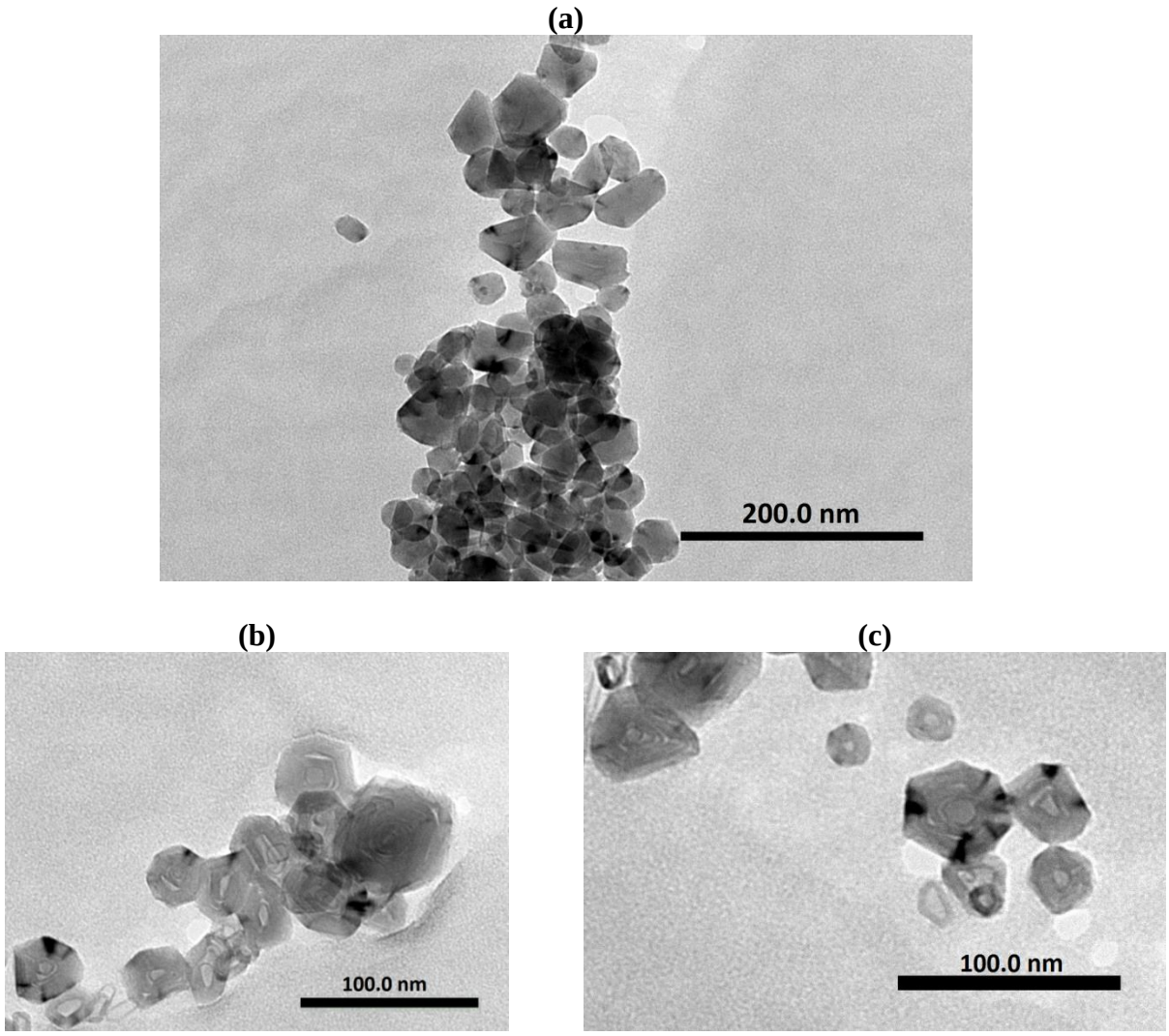

Figure 5.19: TEM images of grinded Ds sample. (a) Fragment consisting of only CNOs clearly distinguishes each one. (b) Image shows clearly polyhedral structures of CNOs, (c) A polyhedral CNOs with dimensions of (20-50) nm.

In Figure 5.20 we show the Raman spectra of Ds and Sp with Ds. The degree of structural disorder on graphitic planes present in the two samples is similar, as shown by the similar intensity of the D peaks (Figure 5.20. b). The most significant difference is found in the form of the 2D peak. Unlike the 2D peak of Sp sample, which presents the typical *bimodal* shape as in graphite, the spectrum obtained on Ds sample is essentially *monomodal*.

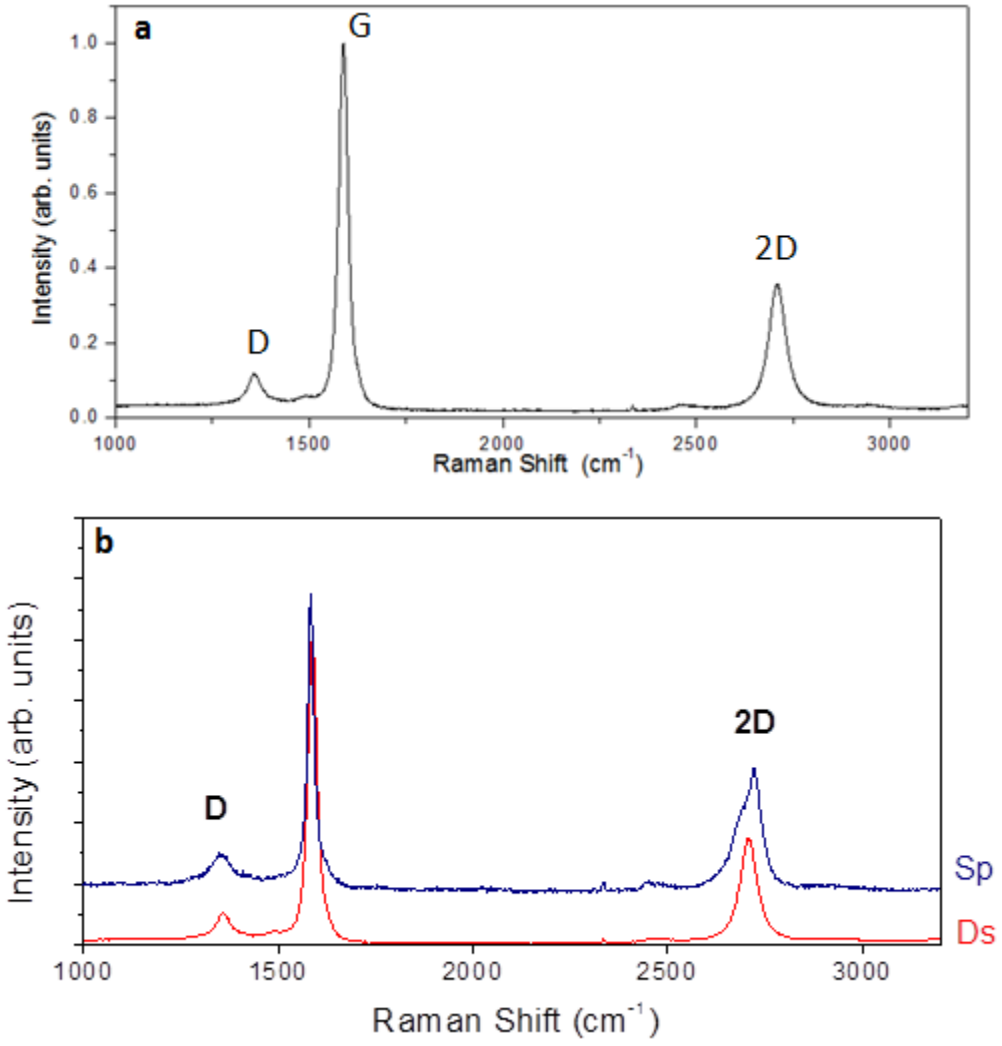

Figure 5.20: Plots of Raman spectra of material: a) discoid formed on the cathode (Ds), b) floating on surface of water (Sp) compared with material of discoid formed on the cathode (Ds).

A monomodal 2D peak can be attributed to turbostratic graphite, namely graphite in which there is rotational disorder in the "stacking" between adjacent graphene sheets. As for the CNOs, it can be hypothesized that the planar areas are formed by turbostratic graphite, and that the curved parts, if present, do not significantly contribute to the 2D peak [7,19]. Figure 5.21 shows the fit of the 2D band evidence in Raman spectra (a) fit of 2D band of Ds sample with composition of polyhedral CNOs, and (b) the form of the 2D band reported by Codorniu Pujals *et al.* [203], obtained on polyhedral nano-onions in the presence of curved zones (such as

fullerene). It has to be noted that the difference in the 2D peak location compared to our spectrum is due to the use of a laser with a different wavelength (632 nm instead of 514 nm).

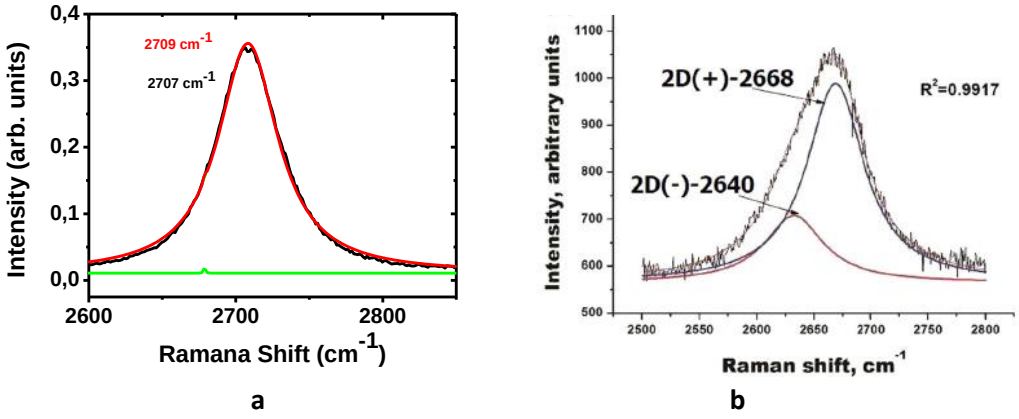

Figure 5.21: (a) Fit of 2D band Raman spectra Ds sample formed exclusively of CNOs fragments.

(b) Fit of the 2D band of polyhedral CNOs [203].

The results obtained show that the discharge procedure in deionized water between two graphite electrodes generated carbonaceous nanostructures with different geometry. There are, in fact, polyhedral CNOs with diameters ranging from tens to hundreds of nanometers, multi-walled CNTs with a variable diameter between approximately 10 and 20 nm, and planar structures also extended up to a few micrometers, attributable to multi-layer graphene, which in some cases show typical graphite oxide undulations. In the samples collected at the bottom and on the surface of the reaction vessel, there are also carbonaceous structures that do not have a particular symmetry, probably due to a fragmentation of the anode not followed by a rearrangement process in the plasmatic environment.

Our results showed that, under our experimental conditions, there is a similar percentage of CNOs and CNTs in samples taken on the water surface and on the bottom of the reaction vessel. In these samples, the CNOs have variable dimensions in a very high range, the presence of a considerable quantity of CNOs with a diameter of the order of tens of nanometers is noted, as well as the presence of a numerically lower quantity of CNOs with dimensions of up to 400 nanometers.

The presence of thin undulated nanostructures along with thin planar nanostructures is very important. This last can be interpreted as multi-layer graphene, and their presence is compatible with an exfoliation process of the anode fragments guided by the pressure conditions present in the vicinity of the plasmatic zone.

Perhaps the more important observation in our experiments is the formation of a solid agglomerate in the zone of the plasma, which remains on the cathode but is not bonded to it. In fact, the cathode surface remains unchanged after having removed such agglomerate. Raman and TEM studies revealed that the agglomerate is made exclusively of CNOs, and this is a particularly important finding, in view of the fact that complex purification procedures are usually necessary to obtain small CNOs quantities from the carbonaceous particles which are found in the discharge water.

Our results lead us to make some hypotheses on the way in which, following the sublimation of carbon atoms, crystallization takes place to form the detected nanostructures. In our experiments, the formation of the agglomerate of CNOs, formed on the cathode surface in full plasmatic zone, contradicts the mechanism proposed in the literature [12–14].

Sano and coworkers reported [85] that from a gaseous state reached at the center of the plasmatic zone (sublimation), the carbon atoms, pushed outwards by the pressure of gases generated, crystallize by means of an epitaxial temperature gradient, assuming the allotropic forms typical of carbon nanostructures:

- The CNTs are formed in the area immediately adjacent to the plasmatic zone, favored by the presence of an epitaxial current of C^+ ions.
- The CNOs formed immediately in the immediately successive zone, where there is an absence of an epitaxial current, promote an increase of isotropic structures.

In our work, the presence of an agglomerate of discoidal form adhering to the cathode surface in correspondence of the axial position of the anode during the electrical discharge, but in

reality easily withdrawable from the cathode surface without leaving macroscopic signs of damage is incompatible with the model reported by Sano *et al*.

Figure 5.22 shows the mechanism we propose for the formation of the discoidal agglomerate made of CNOs. Such formation can only be explained if we assume that the synthesis of the nanostructures occurs in the plasmatic zone because of the temperature gradient very close to the cathode surface, and that such nanostructures are deposited on the cathode, forming the discoid of CNOs.

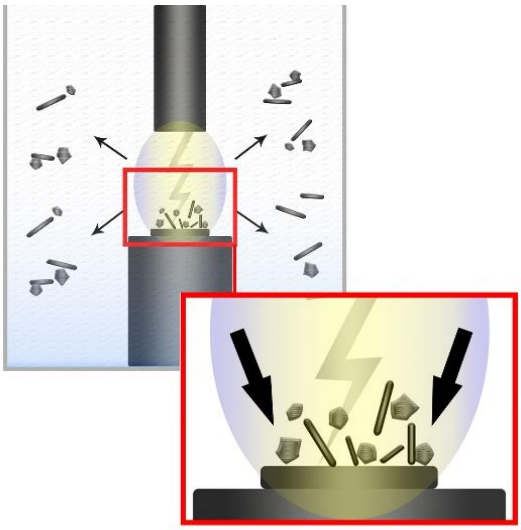

Figure 5.22: Schema of the mechanism of formation of CNPs in our synthesis.

Furthermore, the TEM and Raman results show that there are notable differences between the particles deposited on the cathode forming the discoid and those present in suspension. The TEM images show that the CNOs present in the discoid all have dimensions of the order of tens of nanometers, and they are not observed with much larger dimensions (up to 600 nanometers) as in the case of the samples in suspension. In some fragments, they result as being linked to nanotubes of various diameters, but there are also fragments consisting only of CNOs.

It should also be noted that the images of the fragments which constitute the discoid show no apparent areas of “disorder”, as in the case of the fragments in suspension. The discoid is mainly made of CNOs, and this observation is in agreement with the Raman spectrum obtained on the agglomeration area.

5.3 Conclusions

Our results show a new crystallization mechanism in the underwater arc discharge production of CNOs. Such mechanism generates an agglomerate of CNOs on the surface of the cathode, then in a zone adjacent to the plasma, in which carbon ions crystallize without any interaction with surrounding water. The agglomerate is made of CNOs strongly bonded each other, probably by Van der Waals forces. We made various attempts to disaggregate it, and we obtain the best result by the vibratory micro-mill method. In this way, we are able to obtain CNOs without any purification method.

REFERENCES

[1] N. Taniguchi, “On the basic concept of ‘nano-technology,’” in *Proc. Intl. Conf. Prod. Eng., Part II, Japan Society of Precision Engineering*, 1974.

[2] “See: ‘http://www.foresight.org/nano/history.html’ for a short history of nanotechnology,” *Foresight Institute*, 2013. .

[3] A. K. Geim and K. S. Novoselov, “The rise of graphene.,” *Nat. Mater.*, vol. 6, no. 3, pp. 183–91, 2007.

[4] A. H. Castro Neto, F. Guinea, N. M. R. Peres, K. S. Novoselov, and A. K. Geim, “The electronic properties of graphene,” *Rev. Mod. Phys.*, vol. 81, no. 1, pp. 109–162, 2009.

[5] a K. Geim, “Graphene: Status and Prospects,” *Science (80-.).*, vol. 324, no. June, pp. 1530–1534, 2009.

[6] Q. Yu, J. Lian, S. Siriponglert, H. Li, Y. P. Chen, and S. S. Pei, “Graphene segregated on Ni surfaces and transferred to insulators,” *Appl. Phys. Lett.*, vol. 93, no. 11, pp. 10–13, 2008.

[7] J.-Y. C. and K.S. Kim, Y. Zhao, H. Jang, S.Y. Lee, J.M. Kim, K.S. Kim, J.-H. Ahn, P. Kim and B. H. Hong, “Large-scale pattern growth of graphene films for stretchable transparent electrodes.,” *Nature*, vol. 457, no. 4, pp. 706–710, 2009.

[8] X. Li *et al.*, “Large area synthesis of high quality and uniform graphene films on copper foils,” *Science (80-.).*, vol. 324, no. 5932, pp. 1312–1314, 2009.

[9] S. Bae *et al.*, “Roll-to-roll production of 30-inch graphene films for transparent electrodes,” *Nat. Nanotechnol.*, vol. 5, no. 8, pp. 574–578, 2010.

[10] J. Bai *et al.*, “Very large magnetoresistance in graphene nanoribbons.,” *Nat. Nanotechnol.*, vol. 5, no. 9, pp. 655–659, 2010.

[11] J. Cai *et al.*, “Atomically precise bottom-up fabrication of graphene nanoribbons.,” *Nature*, vol. 466, no. 7305, pp. 470–3, 2010.

[12] E. R. T. Ohta, T. Seyller, K. Horn, “Controlling the Electronic Structure of Bilayer Graphene,” *Science (80-.).*, vol. 313, no. 5789, pp. 951–954, 2006.

[13] Y. Zhang *et al.*, “Direct observation of a widely tunable bandgap in bilayer graphene.,” *Nature*, vol. 459, no. 7248, pp. 820–3, 2009.

[14] X. Wang *et al.*, “N-doping of graphene through electrothermal reactions with ammonia,” *Science (80-.).*, vol. 324, no. 5928, pp. 768–771, 2009.

[15] S. Dutta and S. K. Pati, “Half-metallicity in undoped and boron doped graphene nanoribbons in the presence of semilocal exchange-correlation interactions,” *J. Phys. Chem. B*, vol. 112, no. 5, pp. 1333–1335, 2008.

[16] Y. Mao, J. Yuan, and J. Zhong, “Density functional calculation of transition metal adatom adsorption on graphene,” *Phys. B Condens. Matter*, vol. 405, no. 16, pp. 3337–3341, 2010.

[17] J. Wintterlin and M. L. Bocquet, “Graphene on metal surfaces,” *Surf. Sci.*, vol. 603, no. 10–12, pp. 1841–1852, 2009.

[18] P. A. Khomyakov, G. Giovannetti, P. C. Rusu, G. Brocks, J. Van Den Brink, and P. J. Kelly, “First-principles study of the interaction and charge transfer between graphene and metals,” *Phys. Rev. B - Condens. Matter Mater. Phys.*, vol. 79, no. 19, pp. 1–12, 2009.

[19] E. Rotenberg, A. Bostwick, T. Ohta, J. L. McChesney, T. Seyller, and K. Horn, “Origin of the energy bandgap in epitaxial graphene.,” *Nat. Mater.*, vol. 7, no. 4, pp. 258-259-260, 2008.

[20] S. Y. Zhou *et al.*, “Origin of the energy bandgap in epitaxial graphene.,” *Nat. Mater.*, vol. 7, no. 4, pp. 258-259-260, 2008.

[21] G. Giovannetti, P. A. Khomyakov, G. Brocks, P. J. Kelly, and J. Van Den Brink, “Substrate-induced band gap in graphene on hexagonal boron nitride: Ab initio density functional calculations,” *Phys. Rev. B - Condens. Matter Mater. Phys.*, vol. 76, no. 7, pp. 2–5, 2007.

[22] A. M. Shikin, G. V. Prudnikova, V. K. Adamchuk, F. Moresco, and K. H. Rieder, “Surface intercalation of gold underneath a graphite monolayer on Ni(111) studied by angle-resolved photoemission and high-resolution electron-energy-loss spectroscopy,” *Phys. Rev. B - Condens. Matter Mater. Phys.*, vol. 62, no. 19, pp. 13202–13208, 2000.

[23] Y. Dedkov *et al.*, “Intercalation of copper underneath a monolayer of graphite on Ni(111),” *Phys. Rev. B*, vol. 64, no. 3, pp. 1–6, 2001.

[24] Y. S. Dedkov, M. Fonin, U. Rüdiger, and C. Laubschat, “Graphene-protected iron layer on Ni(111),” *Appl. Phys. Lett.*, vol. 93, no. 2, pp. 0–3, 2008.

[25] I. Gierz, C. Riedl, U. Starke, C. R. Ast, and K. Kern, “Atomic hole doping of graphene,” *Nano Lett.*, vol. 8, no. 12, pp. 4603–4607, 2008.

[26] C. Enderlein, Y. S. Kim, A. Bostwick, E. Rotenberg, and K. Horn, “The formation of an energy gap in graphene on ruthenium by controlling the interface,” *New J. Phys.*, vol. 12, no. 111, 2010.

[27] I. Gierz *et al.*, “Electronic decoupling of an epitaxial graphene monolayer by gold

intercalation," *Phys. Rev. B - Condens. Matter Mater. Phys.*, vol. 81, no. 23, pp. 1–6, 2010.

[28] K. T. Chan, J. B. Neaton, and M. L. Cohen, "First-principles study of metal adatom adsorption on graphene," *Phys. Rev. B - Condens. Matter Mater. Phys.*, vol. 77, no. 23, pp. 1–12, 2008.

[29] D. W. Boukhvalov and M. I. Katsnelson, "Chemical functionalization of graphene," *Molecules*, vol. 344205, 2009.

[30] C. Coletti *et al.*, "Charge neutrality and band-gap tuning of epitaxial graphene on SiC by molecular doping," *Phys. Rev. B - Condens. Matter Mater. Phys.*, vol. 81, no. 23, pp. 1–8, 2010.

[31] E. J. H. Lee, K. Balasubramanian, R. T. Weitz, M. Burghard, and K. Kern, "Contact and edge effects in graphene devices," *Nat. Nanotechnol.*, vol. 3, no. August, pp. 486–490, 2008.

[32] F. Xia *et al.*, "Photocurrent imaging and efficient photon detection in a graphene transistor," *Nano Lett.*, vol. 9, no. 3, pp. 1039–1044, 2009.

[33] T. Mueller, F. Xia, M. Freitag, J. Tsang, and P. Avouris, "Role of contacts in graphene transistors: A scanning photocurrent study," *Phys. Rev. B - Condens. Matter Mater. Phys.*, vol. 79, no. 24, pp. 1–6, 2009.

[34] B. Huard, N. Stander, J. A. Sulpizio, and D. Goldhaber-Gordon, "Evidence of the role of contacts on the observed electron-hole asymmetry in graphene," *Phys. Rev. B - Condens. Matter Mater. Phys.*, vol. 78, no. 12, 2008.

[35] A. Nagashima, H. Itoh, T. Ichinokawa, C. Oshima, and S. Otani, "Change in the electronic states of graphite overlayers depending on thickness," *Phys. Rev. B*, vol. 50, no. 7, pp. 4756–4763, 1994.

[36] C. Oshima and A. Nagashima, "Ultra-thin epitaxial films of graphite and hexagonal boron nitride on solid surfaces," *J. Phys. Condens. Matter*, vol. 9, pp. 1–20, 1997.

[37] K. S. Novoselov *et al.*, "Electric Field Effect in Atomically Thin Carbon Films," *Science (80-.).*, vol. 306, no. 5696, pp. 666–669, 2004.

[38] K. Takeda and K. Shiraishi, "Electronic-Structure of Si-Skeleton Materials," *Phys. Rev. B*, vol. 39, no. 15, pp. 11028–11037, 1989.

[39] K. Takeda and K. Shiraishi, "of Si of," vol. 50, no. 20, 1994.

[40] Y. Wang, K. Scheerschmidt, and U. Gösele, "Theoretical investigations of bond properties in graphite and graphitic silicon," *Phys. Rev. B*, vol. 61, no. 19, pp. 12864–12870, 2000.

[41] X. Yang and J. Ni, “Electronic properties of single-walled silicon nanotubes compared to carbon nanotubes,” *Phys. Rev. B - Condens. Matter Mater. Phys.*, vol. 72, no. 19, pp. 1–5, 2005.

[42] E. Durgun, S. Tongay, and S. Ciraci, “Silicon and III-V compound nanotubes: Structural and electronic properties,” *Phys. Rev. B - Condens. Matter Mater. Phys.*, vol. 72, no. 7, pp. 1–10, 2005.

[43] H. Nakano, M. Ishii, and H. Nakamura, “Preparation and structure of novel siloxene nanosheets.,” *Chem. Commun. (Camb).*, vol. 2, no. 23, pp. 2945–2947, 2005.

[44] H. Nakano *et al.*, “Soft synthesis of single-crystal silicon monolayer sheets,” *Angew. Chemie - Int. Ed.*, vol. 45, no. 38, pp. 6303–6306, 2006.

[45] A. Kara *et al.*, “Physics of silicene stripes,” *J. Supercond. Nov. Magn.*, vol. 22, no. 3, pp. 259–263, 2009.

[46] D. Chiappe, C. Grazianetti, G. Tallarida, M. Fanciulli, and A. Molle, “Local electronic properties of corrugated silicene phases,” *Adv. Mater.*, vol. 24, no. 37, pp. 5088–5093, 2012.

[47] B. Feng *et al.*, “Evidence of silicene in honeycomb structures of silicon on Ag(111),” *Nano Lett.*, vol. 12, no. 7, pp. 3507–3511, 2012.

[48] H. Jamgotchian *et al.*, “Growth of silicene layers on Ag(111): unexpected effect of the substrate temperature,” *J. Phys. Condens. Matter*, vol. 24, no. 17, p. 172001, 2012.

[49] C. L. Lin *et al.*, “Structure of silicene grown on Ag(111),” *Appl. Phys. Express*, vol. 5, no. 4, pp. 5–8, 2012.

[50] P. Vogt *et al.*, “Silicene: Compelling experimental evidence for graphenelike two-dimensional silicon,” *Phys. Rev. Lett.*, vol. 108, no. 15, pp. 1–5, 2012.

[51] G. G. Guzmán-Verri and L. C. Lew Yan Voon, “Electronic structure of silicon-based nanostructures,” *Phys. Rev. B - Condens. Matter Mater. Phys.*, vol. 76, no. 7, 2007.

[52] L. Tao *et al.*, “Silicene field-effect transistors operating at room temperature,” *Nat. Nanotechnol.*, vol. 10, no. 3, pp. 227–231, 2015.

[53] K. Takeda and K. Shiraishi, “Theoretical possibility of stage corrugation in Si and Ge analogs of graphite,” *Phys. Rev. B*, vol. 50, no. 20, 1994.

[54] S. Cahangirov, M. Topsakal, E. Aktürk, H. Šahin, and S. Ciraci, “Two- and one-dimensional honeycomb structures of silicon and germanium,” *Phys. Rev. Lett.*, vol. 102, no. 23, pp. 1–4, 2009.

[55] B. Aufray *et al.*, “Graphene-like silicon nanoribbons on Ag(110): A possible formation of silicene,” *Appl. Phys. Lett.*, vol. 96, no. 18, pp. 1–4, 2010.

[56] B. Lalmi *et al.*, “Epitaxial growth of a silicene sheet,” *Appl. Phys. Lett.*, vol. 97, no. 22, pp. 96–98, 2010.

[57] G. Le Lay, P. De Padova, a Resta, T. Bruhn, and P. Vogt, “Epitaxial silicene: can it be strongly strained?,” *J. Phys. D. Appl. Phys.*, vol. 45, p. 392001, 2012.

[58] V. Ongun Özçelik and S. Ciraci, “Local reconstructions of silicene induced by adatoms,” *J. Phys. Chem. C*, vol. 117, no. 49, pp. 26305–26315, 2013.

[59] S. Cahangirov, V. O. Ozcelik, A. Rubio, and S. Ciraci, “Silicite: The layered allotrope of silicon,” *Phys. Rev. B - Condens. Matter Mater. Phys.*, vol. 90, no. 8, pp. 1–5, 2014.

[60] S. Cahangirov *et al.*, “Atomic structure of the 3 × 3 phase of silicene on Ag(111),” *Phys. Rev. B*, vol. 90, no. 3, p. 35448, 2014.

[61] L. Tao *et al.*, “Silicene field-effect transistors operating at room temperature,” *Nat. Nanotechnol.*, vol. 10, no. 3, pp. 227–231, 2015.

[62] M. Peplow, “Silicene makes its transistor debut,” *Nature*, vol. 518, p. 17, 2015.

[63] M. Davenport, “Two-Dimensional Silicon Makes Its Device Debut,” *acs.org*, 2015.

[64] J. C. Garcia, D. B. de Lima, L. V. C. Assali, and J. F. Justo, “Group-IV Graphene-and Graphane-Like Nanosheets,” *J. Phys. Chem. C*, vol. 115, pp. 13242–13246, 2011.

[65] D. Jose and A. Datta, “Structures and Chemical Properties of Silicene: Unlike Graphene,” *Acc. Chem. Res.*, vol. 47, no. 2, pp. 593–602, 2014.

[66] Y. Du *et al.*, “Tuning the band gap in silicene by oxidation,” *ACS Nano*, vol. 8, no. 10, pp. 10019–10025, 2014.

[67] P. De Padova *et al.*, “Burning match oxidation process of silicon nanowires screened at the atomic scale,” *Nano Lett.*, vol. 8, no. 8, pp. 2299–2304, 2008.

[68] L. Chen *et al.*, “Evidence for Dirac fermions in a honeycomb lattice based on silicon,” *Phys. Rev. Lett.*, vol. 109, no. 5, pp. 1–5, 2012.

[69] Z. X. Guo, S. Furuya, J. I. Iwata, and A. Oshiyama, “Absence of dirac electrons in silicene on Ag(111) surfaces,” *J. Phys. Soc. Japan*, vol. 82, no. 6, pp. 1–5, 2013.

[70] Y. P. Wang and H. P. Cheng, “Absence of a Dirac cone in silicene on Ag(111): First-principles density functional calculations with a modified effective band structure technique,” *Phys. Rev. B*, vol. 87, no. 24, pp. 1–5, 2013.

[71] R. Arafune, C.-L. Lin, R. Nagao, M. Kawai, and N. Takagi, "Comment on 'Evidence for Dirac Fermions in a Honeycomb Lattice Based on Silicon,'" *Phys. Rev. Lett.*, vol. 110, no. 22, p. 229701, 2013.

[72] C. L. Lin *et al.*, "Substrate-induced symmetry breaking in silicene," *Phys. Rev. Lett.*, vol. 110, no. 7, pp. 1–5, 2013.

[73] P. Gori, O. Pulci, F. Ronci, S. Colonna, and F. Bechstedt, "Origin of Dirac-cone-like features in silicon structures on Ag(111) and Ag(110)," *J. Appl. Phys.*, vol. 114, no. 11, pp. 1–6, 2013.

[74] X. Xu *et al.*, "Effects of oxygen adsorption on the surface state of epitaxial silicene on Ag(111).," *Sci. Rep.*, vol. 4, p. 7543, 2014.

[75] S. K. Mahatha *et al.*, "Silicene on Ag(111): A honeycomb lattice without Dirac bands," *Phys. Rev. B*, vol. 89, no. 20, pp. 1–5, 2014.

[76] J. Gao and J. Zhao, "Initial geometries, interaction mechanism and high stability of silicene on Ag(111) surface.," *Sci. Rep.*, vol. 2, no. 111, p. 861, 2012.

[77] H. W. Kroto, J. R. Heath, S. C. O'Brien, R. F. Curl, and R. E. Smalley, "C 60: buckminsterfullerene," *Nature*, vol. 318, p. 162, 1985.

[78] S. Iijima, "Helical microtubules of graphitic carbon," *Nature*, vol. 354, pp. 627–628, 1991.

[79] D. Ugarte, "Curling and closure of graphitic networks under electron-beam irradiation.," *Nature*, vol. 359, no. 6397, pp. 707–709, 1992.

[80] J. McDonough and Y. Gogotsi, "Carbon Onions: Synthesis and Electrochemical Applications," *Electrochem. Soc. Interface*, vol. 22, no. 3, pp. 61–66, 2013.

[81] K. Bogdanov *et al.*, "Annealing-induced structural changes of carbon onions: High-resolution transmission electron microscopy and Raman studies," *Carbon N. Y.*, vol. 73, pp. 78–86, 2014.

[82] F.-D. Han, B. Yao, and Y.-J. Bai, "Preparation of Carbon Nano-Onions and Their Application as Anode Materials for Rechargeable Lithium-Ion Batteries," *J. Phys. Chem. C*, vol. 115, no. 18, pp. 8923–8927, 2011.

[83] J. Macutkevic *et al.*, "Terahertz probing of onion-like carbon-PMMA composite films," *Diam. Relat. Mater.*, vol. 17, no. 7–10, pp. 1608–1612, 2008.

[84] T. Cabioc'h, J. P. Riviere, and J. Delafond, "A new technique for fullerene onion formation," *J. Mater. Sci.*, vol. 30, no. 19, pp. 4787–4792, 1995.

[85] N. Sano, H. Wang, M. Chhowalla, I. Alexandrou, and G. A. J. Amaratunga, "Synthesis of carbon 'onions' in water," *Nature*, vol. 414, no. 6863, p. 506, 2001.

[86] I. Alexandrou, H. Wang, N. Sano, and G. A. J. Amaratunga, "Structure of carbon onions and nanotubes formed by arc in liquids," *J. Chem. Phys.*, vol. 120, no. 2, pp. 1055–1058, 2004.

[87] J. Bartelmess and S. Giordani, "Carbon nano-onions (multi-layer fullerenes): chemistry and applications," *Nanotechnology*, no. 5, pp. 1980–1998, 2014.

[88] J. F. Watts and J. Wolstenholme, *An Introduction to Surface Analysis by XPS and AES*. England: Wiley & Sons Ltd., 2003.

[89] A. A. Lucas, "Fast-Electron Spectroscopy of Surface Excitations," *Phys. Rev. Lett.*, vol. 26, no. 5, 1971.

[90] E. Evans and D. L. Mills, "Theory of inelastic scattering of slow electrons by long-wavelength surface of optical phonons," *Phys. Rev. B*, vol. 5, no. 10, p. 4126, 1972.

[91] E. Evans and D. L. Mills, "Theory of Inelastic Scattering of Slow Electrons by Long-Wavelength Surface of Optical Phonons: Multiphonon Processes," *Phys. Rev. B*, vol. 7, no. 2, p. 853, 1973.

[92] D. L. Mills, "The scattering of low energy electrons by electric field fluctuations near crystal surfaces," *Surf. Sci.*, vol. 48, no. 1, pp. 59–79, 1975.

[93] F. Wooten, "Optical Properties of Solids," *Acad. Press N.Y.*, 1972.

[94] "'Raman spectroscopy basis' Princeton Instruments." .

[95] E. Widenkvist, "Fabrication and Functionalization of graphene and other carbon nanomaterials in solution," 2010.

[96] A. C. Ferrari, "Raman spectroscopy of graphene and graphite: Disorder, electron-phonon coupling, doping and nonadiabatic effects," *Solid State Commun.*, vol. 143, no. 1–2, pp. 47–57, 2007.

[97] A. C. Ferrari *et al.*, "Raman spectrum of graphene and graphene layers," *Phys. Rev. Lett.*, vol. 97, no. 18, pp. 1–4, 2006.

[98] D. B. Williams and C. B. Carter, *Transmission Electron Microscopy: A Textbook for Materials Science*, vol. 1–4. 2009.

[99] "http://www.nanoscience.gatech.edu/zlwang/research/tem.html." .

[100] L. C. Isett and J. M. Blakely, "Binding energies of carbon to Ni(100) from equilibrium

segregation studies," *Surf. Sci.*, vol. 47, no. 2, pp. 645–649, 1975.

[101] L. C. Isett and J. M. Blakely, "Segregation isosteres for carbon at the (100) surface of nickel," *Surf. Sci.*, vol. 58, no. 2, pp. 397–414, 1976.

[102] J. C. Shelton, J. C. SHELTON, H. R. PATIL, and J. M. BLAKELY, "Equilibrium Segregation of Carbon To a Nickel (111) Surface : a Surface Phase Transition," *Surf. Sci.*, vol. 43, 1974.

[103] M. Eizenberg and J. M. Blakely, "Carbon monolayer phase condensation on Ni(111)," *Surf. Sci.*, vol. 82, no. 1, pp. 228–236, 1979.

[104] M. Eizenberg and J. M. Blakely, "Carbon interaction with nickel surfaces: Monolayer formation and structural stability," *J. Chem. Phys.*, vol. 71, no. 8, p. 3467, 1979.

[105] R. Rosei, M. De Crescenzi, F. Sette, C. Quaresima, A. Savoia, and P. Perfetti, "Structure of graphitic carbon on Ni(111): A surface extended-energy-loss fine-structure study," *Phys. Rev. B*, vol. 28, no. 2, pp. 1161–1164, 1983.

[106] Y. GAMO, A. NAGASHIMA, M. WAKABAYASHI, M. TERAI, and C. OSHIMA, "Atomic Structure of Monolayer Graphite Formed on Ni(111).," *Hyomen Kagaku*, vol. 374, no. 12, pp. 61–64, 1997.

[107] R. Rosei, S. Modesti, F. Sette, C. Quaresima, A. Savoia, and P. Perfetti, "Photoemission spectroscopy investigation of the electronic structure of carbidic and graphitic carbon on Ni (111)," *Solid State Commun.*, vol. 46, no. 12, pp. 871–874, 1983.

[108] A. Nagashima, N. Tejima, and C. Oshima, "Electronic states of the pristine and alkali-metal-intercalated monolayer graphite/Ni(111) systems," *Phys. Rev. B*, vol. 50, no. 23, pp. 17487–17495, 1994.

[109] E. Voloshina and Y. Dedkov, "Electronic and Magnetic Properties of the Graphene-Ferromagnet Interfaces: Theory vs. Experiment," *(INTECH Educ. Publ. Vienna, 2010)*, no. June 2016.

[110] A. Grüneis and D. V. Vyalikh, "Tunable hybridization between electronic states of graphene and a metal surface," *Phys. Rev. B - Condens. Matter Mater. Phys.*, vol. 77, no. 19, pp. 1–4, 2008.

[111] Y. S. Dedkov and M. Fonin, "Electronic and magnetic properties of the graphene-ferromagnet interface," *New J. Phys.*, vol. 12, p. 125004, 2010.

[112] G. Bertoni, L. Calmels, A. Altibelli, and V. Serin, "First-principles calculation of the electronic structure and EELS spectra at the graphene/Ni(111) interface," *Phys. Rev. B - Condens. Matter Mater. Phys.*, vol. 71, no. 7, pp. 1–8, 2004.

[113] V. M. Karpan *et al.*, "Graphite and graphene as perfect spin filters," *Phys. Rev. Lett.*, vol. 99, no. 17, 2007.

[114] V. M. Karpan *et al.*, "Theoretical prediction of perfect spin filtering at interfaces between close-packed surfaces of Ni or Co and graphite or graphene," *Phys. Rev. B - Condens. Matter Mater. Phys.*, vol. 78, no. 19, pp. 1–11, 2008.

[115] M. Fuentes-Cabrera, M. I. Baskes, A. V. Melechko, and M. L. Simpson, "Bridge structure for the graphene/Ni(111) system: A first principles study," *Phys. Rev. B - Condens. Matter Mater. Phys.*, vol. 77, no. 3, pp. 1–5, 2008.

[116] G. Kalibaeva, R. Vuilleumier, S. Meloni, A. Alavi, G. Ciccotti, and R. Rosei, "Ab initio simulation of carbon clustering on an Ni(111) surface: A model of the poisoning of nickel-based catalysts," *J. Phys. Chem. B*, vol. 110, no. 8, pp. 3638–3646, 2006.

[117] C. Klink, I. Stensgaard, F. Besenbacher, and E. Lægsgaard, "An STM study of carbon-induced structures on Ni(111): evidence for a carbidic-phase clock reconstruction," *Surf. Sci.*, vol. 342, no. 1–3, pp. 250–260, 1995.

[118] Y. S. Dedkov, M. Fonin, and C. Laubschat, "A possible source of spin-polarized electrons: The inert graphene/Ni(111) system," *Appl. Phys. Lett.*, vol. 92, no. 5, pp. 95–98, 2008.

[119] Y. S. Dedkov, M. Fonin, U. Rudiger, and C. Laubschat, "Rashba effect in the graphene/Ni(111) system," *Phys. Rev. Lett.*, vol. 100, no. 10, pp. 1–4, 2008.

[120] E. Voloshina and Y. Dedkov, "Electronic and Magnetic Properties of the Graphene-Ferromagnet Interfaces: Theory vs. Experiment," *Phys. Appl. Graphene - Exp.*, no. June 2016, 2011.

[121] A. Grüneis, K. Kummer, and D. V. Vyalikh, "Dynamics of graphene growth on a metal surface: A time-dependent photoemission study," *New J. Phys.*, vol. 11, no. 1, 2009.

[122] K. Yamamoto, M. Fukushima, T. Osaka, and C. Oshima, "Charge-transfer mechanism for the (monolayer graphite) /Ni(111) system," *Phys. Rev. B*, vol. 45, no. 19, pp. 11358–11361, 1992.

[123] Y. Souzu and M. Tsukada, "Electronic states and scanning tunneling spectroscopy image of monolayer graphite on a nickel (111) surface by the DV-X ?? method," *Surf. Sci.*, vol. 326, no. 1–2, pp. 42–52, 1995.

[124] M. Weser *et al.*, "Induced magnetism of carbon atoms at the graphene/Ni(111) interface," *Appl. Phys. Lett.*, vol. 96, no. 1, pp. 1–4, 2010.

[125] J. Rusz *et al.*, "Dynamical effects in x-ray absorption spectra of graphene and monolayered h -BN on Ni(111)," *Phys. Rev. B - Condens. Matter Mater. Phys.*, vol. 81,

no. 7, pp. 4–7, 2010.

[126] O. Wessely, M. I. Katsnelson, and O. Eriksson, “Ab initio theory of dynamical core-hole screening in graphite from x-ray absorption spectra,” *Phys. Rev. Lett.*, vol. 94, no. 16, pp. 1–4, 2005.

[127] G. Giovannetti, P. A. Khomyakov, G. Brocks, V. M. Karpan, J. Van Den Brink, and P. J. Kelly, “Doping graphene with metal contacts,” *Phys. Rev. Lett.*, vol. 101, no. 2, pp. 4–7, 2008.

[128] E. L. Shirley, L. J. Terminello, A. Santoni, and F. J. Himpsel, “Brillouin-zone-selection effects in graphite photoelectron angular distributions,” *Phys. Rev. B*, vol. 51, no. 19, pp. 13614–13622, 1995.

[129] E. H. Hwang and S. Das Sarma, “Dielectric function, screening, and plasmons in two-dimensional graphene,” *Phys. Rev. B - Condens. Matter Mater. Phys.*, vol. 75, no. 20, pp. 1–6, 2007.

[130] T. Ando, A. B. Fowler, and F. Stern, “Electronic properties of two-dimensional systems,” *Rev. Mod. Phys.*, vol. 54, no. 2, pp. 437–672, 1982.

[131] Y. Liu, R. F. Willis, K. V. Emtsev, and T. Seyller, “Plasmon dispersion and damping in electrically isolated two-dimensional charge sheets,” *Phys. Rev. B - Condens. Matter Mater. Phys.*, vol. 78, no. 20, pp. 2–5, 2008.

[132] S. Y. Shin, C. G. Hwang, S. J. Sung, N. D. Kim, H. S. Kim, and J. W. Chung, “Observation of intrinsic intraband π-plasmon excitation of a single-layer graphene,” *Phys. Rev. B - Condens. Matter Mater. Phys.*, vol. 83, no. 16, pp. 3–6, 2011.

[133] A. Nagashima *et al.*, “Two-dimensional plasmons in monolayer graphite,” *Solid State Commun.*, vol. 83, no. 8, pp. 581–585, 1992.

[134] M. Weser, E. N. Voloshina, K. Horn, and Y. S. Dedkov, “Electronic structure and magnetic properties of the graphene/Fe/Ni(111) intercalation-like system,” *Phys. Chem. Chem. Phys.*, vol. 13, no. 16, p. 7534, 2011.

[135] Y. S. Dedkov and M. Fonin, “Electronic and magnetic properties of the graphene-ferromagnet interface,” *New J. Phys.*, vol. 12, 2010.

[136] E. N. Voloshina, A. Generalov, M. Weser, S. Böttcher, K. Horn, and Y. S. Dedkov, “Structural and electronic properties of the graphene/Al/Ni(111) intercalation system,” *New J. Phys.*, vol. 13, no. 1, 2011.

[137] R. H. Ritchie, “Plasma Losses by Fast Electrons in Thin Films,” *phys. Rev.*, vol. 106, no. 5, pp. 874–875, 1956.

[138] K. Zeppenfeld, “Nonvertical interband transitions in graphite by inelastic electron scattering,” *Springer-Verlag*, vol. 243, no. 3, pp. 229–243, 1971.

[139] a. Marinopoulos, L. Reining, A. Rubio, and V. Olevano, “Ab initio study of the optical absorption and wave-vector-dependent dielectric response of graphite,” *Phys. Rev. B*, vol. 69, no. 24, pp. 1–12, 2004.

[140] J. Yan, K. S. Thygesen, and K. W. Jacobsen, “Nonlocal screening of plasmons in graphene by semiconducting and metallic substrates: First-principles calculations,” *Phys. Rev. Lett.*, vol. 106, no. 14, pp. 1–4, 2011.

[141] T. Eberlein *et al.*, “Plasmon spectroscopy of free-standing graphene films,” *Phys. Rev. B - Condens. Matter Mater. Phys.*, vol. 77, no. 23, pp. 1–4, 2008.

[142] C. Kramberger *et al.*, “Linear plasmon dispersion in single-wall carbon nanotubes and the collective excitation spectrum of graphene,” *Phys. Rev. Lett.*, vol. 100, no. 19, pp. 1–4, 2008.

[143] J. Lu, K. Loh, H. Huang, W. Chen, and A. Wee, “Plasmon dispersion on epitaxial graphene studied using high-resolution electron energy-loss spectroscopy,” *Phys. Rev. B*, vol. 80, no. 11, pp. 2–5, 2009.

[144] and C. O. A.Nagashima, K.Nuka, H.Itoh, T.Ichinokawa, “Two-dimensional plasmons in monolayer graphite,” *Soiid State Commun.*, vol. 83, no. 8, pp. 581–585, 1992.

[145] a. V. Generalov and Y. S. Dedkov, “EELS study of the epitaxial graphene/Ni(111) and graphene/Au/Ni(111) systems,” *Carbon N. Y.*, vol. 50, no. 1, p. 31, 2011.

[146] G. Bertoni and L. Calmels, “First-principles calculation of the electronic structure and energy loss near edge spectra of chiral carbon nanotubes,” *Micron*, vol. 37, no. 5, pp. 486–491, 2006.

[147] F. Stern, “POLARIZABILITY OF A TWO-DIMENSIONAL ELECTRON GAS,” *Phys. Rev. Lett.*, vol. 18, no. 14, pp. 0–2, 1967.

[148] K. O. M. Nakayama, T. Kato, “Theory of the intersurface band plasmon,” *Solid State Comm.*, vol. 50, no. 5, pp. 409–412, 1984.

[149] A. Nagashima *et al.*, “Electronic structure of monolayer graphite on some transition metal carbide surfaces,” *Surf. Sci.*, vol. 287–288, no. PART 2, pp. 609–613, 1993.

[150] K. Suenaga and M. Koshino, “Atom-by-atom spectroscopy at graphene edge.,” *Nature*, vol. 468, no. 7327, pp. 1088–1090, 2010.

[151] L. Papagno, L. S. Caputi, M. De Crescenzi, and R. Rosei, “Graphite: Electronic and structural properties studied by electron-energy-loss and secondary-electron-emission

spectroscopy," *Phys. Rev. B*, vol. 26, no. 4, pp. 2320–2322, 1982.

[152] R. A. Rosenberg, P. J. Love, and V. Rehn, "Polarization-dependent C(K) near-edge x-ray-absorption fine structure of graphite," *phys. Rev. B*, vol. 33, no. 6, pp. 4034–4037, 1986.

[153] W. Zhao *et al.*, "Graphene on Ni (111): Coexistence of Different Surface Structures," *J. Chem. Phys. Lett.*, vol. 2, no. 111, pp. 759–764, 2011.

[154] F. Bianchini, L. L. Patera, M. Peressi, C. Africh, and G. Comelli, "Atomic Scale Identi fi cation of Coexisting Graphene Structures on Ni(111)," *J. Phys. Chem. Lett.*, no. 111, 2014.

[155] D. E. Parreiras *et al.*, "Graphene/Ni(111) surface structure probed by low-energy electron diffraction, photoelectron diffraction, and first-principles calculations," *Phys. Rev. B - Condens. Matter Mater. Phys.*, vol. 90, no. 15, pp. 1–9, 2014.

[156] Y. Kobayashi, K. I. Fukui, T. Enoki, and K. Kusakabe, "Edge state on hydrogen-terminated graphite edges investigated by scanning tunneling microscopy," *Phys. Rev. B - Condens. Matter Mater. Phys.*, vol. 73, no. 12, pp. 1–8, 2006.

[157] Z. Majzik *et al.*, "Combined AFM and STM measurements of a silicene sheet grown on the Ag(111) surface.," *J. Phys. Condens. Matter*, vol. 25, no. 22, p. 225301, 2013.

[158] R. Arafune *et al.*, "Structural transition of silicene on Ag(111)," *Surf. Sci.*, vol. 608, pp. 297–300, 2013.

[159] M. R. Tchalala *et al.*, "Atomic and electronic structures of the (13 × 13)R13.9° of silicene sheet on Ag(1 1 1)," *Appl. Surf. Sci.*, vol. 303, pp. 61–66, 2014.

[160] P. Sutter, J. T. Sadowski, and E. Sutter, "Graphene on Pt(111): Growth and substrate interaction," *Phys. Rev. B - Condens. Matter Mater. Phys.*, vol. 80, no. 24, pp. 1–10, 2009.

[161] M. Gao *et al.*, "Epitaxial growth and structural property of graphene on Pt(111)," *Appl. Phys. Lett.*, vol. 98, no. 3, pp. 10–13, 2011.

[162] L. Meng *et al.*, "Multi-oriented moiré superstructures of graphene on Ir(111): experimental observations and theoretical models.," *J. Phys. Condens. Matter*, vol. 24, no. 31, p. 314214, 2012.

[163] S. K. H??m??l??inen *et al.*, "Structure and local variations of the graphene moir?? on Ir(111)," *Phys. Rev. B - Condens. Matter Mater. Phys.*, vol. 88, no. 20, pp. 1–6, 2013.

[164] W. Moritz *et al.*, "Structure determination of the coincidence phase of graphene on Ru(0001)," *Phys. Rev. Lett.*, vol. 104, no. 13, pp. 13–16, 2010.

[165] A. Resta *et al.*, "Atomic structures of silicene layers grown on Ag(111): scanning

tunneling microscopy and noncontact atomic force microscopy observations.," *Sci. Rep.*, vol. 3, p. 2399, 2013.

[166] M. A. Van Hove, "Atomic-scale structure: From surfaces to nanomaterials," *Surf. Sci.*, vol. 603, no. 10–12, pp. 1301–1305, 2009.

[167] M. R. Tchalala *et al.*, "Atomic and electronic structures of the ()R13.9° of silicene sheet on Ag(111)," *Appl. Surf. Sci.*, vol. 303, pp. 61–66, 2014.

[168] H. Enriquez *et al.*, "Atomic structure of the (2√3×2√3) R 30° of silicene on Ag(111) surface," *J. Phys. Conf. Ser.*, vol. 491, p. 12004, 2014.

[169] K. S. Novoselov *et al.*, "Two-dimensional gas of massless Dirac fermions in graphene," *Nature*, vol. 438, no. 7065, pp. 197–200, 2005.

[170] G. Li and E. Y. Andrei, "Observation of Landau levels of Dirac fermions in graphite," *Nat. Phys.*, vol. 3, no. 9, pp. 623–627, 2007.

[171] S. Y. Zhou *et al.*, "First direct observation of Dirac fermions in graphite," *Nat. Phys.*, vol. 2, no. September, pp. 595–599, 2006.

[172] K. Sugawara, T. Sato, S. Souma, T. Takahashi, and H. Suematsu, "Fermi surface and edge-localized states in graphite studied by high-resolution angle-resolved photoemission spectroscopy," *Phys. Rev. B - Condens. Matter Mater. Phys.*, vol. 73, no. 4, pp. 3–6, 2006.

[173] P. Moras, T. O. Mentes, P. M. Sheverdyaeva, a Locatelli, and C. Carbone, "Coexistence of multiple silicene phases in silicon grown on Ag(1 1 1).," *J. Phys. Condens. Matter*, vol. 26, no. 18, p. 185001, 2014.

[174] Z. X. Guo, S. Furuya, J. I. Iwata, and A. Oshiyama, "Absence and presence of Dirac electrons in silicene on substrates," *Phys. Rev. B*, vol. 82, no. 23, pp. 1–10, 2013.

[175] P. Vogt *et al.*, "Silicene: Compelling experimental evidence for graphenelike two-dimensional silicon," *Phys. Rev. Lett.*, vol. 108, no. 15, pp. 1–5, 2012.

[176] J. Avila *et al.*, "Presence of gapped silicene-derived band in the prototypical (3 × 3) silicene phase on silver (111) surfaces," *J. Phys. Condens. Matter*, vol. 25, no. 26, p. 262001, 2013.

[177] D. Tsoutsou, E. Xenogiannopoulou, E. Golias, P. Tsipas, and A. Dimoulas, "Evidence for hybrid surface metallic band in (4 x 4) silicene on Ag(111)," *Appl. Phys. Lett.*, vol. 103, no. 23, 2013.

[178] S. Cahangirov *et al.*, "Electronic structure of silicene on Ag(111): Strong hybridization effects," *Phys. Rev. B - Condens. Matter Mater. Phys.*, vol. 88, no. 3, pp. 1–6, 2013.

[179] M. X. Chen and M. Weinert, “Revealing the substrate origin of the linear dispersion of Silicene/Ag(111),” *Nano Lett.*, vol. 14, no. 9, pp. 5189–5193, 2014.

[180] H. Ishida, Y. Hamamoto, Y. Morikawa, E. Minamitani, R. Arafune, and N. Takagi, “Electronic structure of the 4x4 silicene monolayer on semi-infinite Ag(111),” *New J. Phys.*, vol. 17, no. 111, 2015.

[181] S. K. Mahatha *et al.*, “Absence of Dirac cones in monolayer silicene and multilayer Si films on Ag(111),” *J. Electron Spectros. Relat. Phenomena*, 2016.

[182] W. Wang, W. Olovsson, and R. I. G. Uhrberg, “Experimental and theoretical determination of σ bands on (‘2√3×2√3’) silicene grown on Ag(111),” *Phys. Rev. B - Condens. Matter Mater. Phys.*, vol. 92, no. 20, pp. 1–6, 2015.

[183] P. M. Sheverdyaeva *et al.*, “Electronic States of Silicene Allotropes on Ag(111),” *ACS Nano*, no. 111, p. acsnano.6b07593, 2016.

[184] H. Jamgotchian *et al.*, “Silicene on Ag(111) : domains and local defects of the observed superstructures,” *J. Phys. Conf. Ser.*, vol. 491, no. 1, p. 12001, 2014.

[185] K. D. Tsuei, E. W. Plummer, and P. J. Feibelman, “Surface-plasmon dispersion in simple metals,” *Phys. Rev. Lett.*, vol. 63, no. 20, pp. 2256–2259, 1989.

[186] P. T. Sprunger, G. M. Watson, and E. W. Plummer, “The normal modes at the surface of Li and Mg,” *Surf. Sci.*, vol. 269–270, no. C, pp. 551–555, 1992.

[187] P. J. Feibelman, “Surface electromagnetic fields: Information on non-locality and screening with quantum plasmonics,” *Prog. Surf. Sci.*, vol. 12, no. 4, pp. 287–407, 1982.

[188] A. Liebsch, “Surface plasmon dispersion of Ag,” *Phys. Rev. Lett.*, vol. 71, no. 1, pp. 145–148, 1993.

[189] A. Cupolillo, N. Ligato, and L. S. Caputi, “Two-dimensional character of the interface-?? plasmon in epitaxial graphene on Ni(1 1 1),” *Carbon N. Y.*, vol. 50, no. 7, pp. 2588–2591, 2012.

[190] C. V. Gomez, M. Pisarra, M. Gravina, P. Riccardi, and A. Sindona, “Plasmon properties and hybridization effects in silicene,” *Phys. Rev. B*, vol. 85419, no. 95, p. 85419, 2017.

[191] L. Rast and V. K. Tewary, “Electron Energy Loss Function of Silicene and Germanene Multilayers on Silver,” *Condens. Matter*, 2013.

[192] N. Sano *et al.*, “Properties of carbon onions produced by an arc discharge in water,” *J. Appl. Phys.*, vol. 92, no. 5, pp. 2783–2788, 2002.

[193] J. Guo, X. Wang, Y. Yao, X. Yang, X. Liu, and B. Xu, “Structure of nanocarbons

prepared by arc discharge in water," *Mater. Chem. Phys.*, vol. 105, no. 2–3, pp. 175–178, 2007.

[194] M. Chhowalla, H. Wang, N. Sano, K. B. K. Teo, S. B. Lee, and G. a J. Amaratunga, "Carbon onions: carriers of the 217.5 nm interstellar absorption feature.," *Phys. Rev. Lett.*, vol. 90, no. 15, p. 155504, 2003.

[195] D. Roy *et al.*, "Characterisation of carbon nano-onions using Raman spectroscopy," *Chem. Phys. Lett.*, vol. 373, no. 1–2, pp. 52–56, 2003.

[196] A. Palkar *et al.*, "Reactivity differences between Carbon Nano Onions (CNOs) prepared by different methods," *Chem. - An Asian J.*, vol. 2, no. 5, pp. 625–633, 2007.

[197] W. S. Bacsa, W. A. de Heer, D. Ugarte, and A. Ch??telain, "Raman spectroscopy of closed-shell carbon particles," *Chem. Phys. Lett.*, vol. 211, no. 4–5, pp. 346–352, 1993.

[198] E. D. Obraztsova, M. F. Workspace.c, S. Hayashi, V. L. Kuznetsov, Y. V. Butenko, and A. L. Chuvilin, "Raman identification of onion-like carbon," *Carbon N. Y.*, vol. 36, no. 5–6, pp. 821–826, 1998.

[199] P. C. E. M.S. Dresselhaus, G. Dresselhaus, *Science of fullerenes and Carbon Nanotubes*. London: Academy Press, 1995.

[200] X. Wang, B. Xu, X. Liu, H. Jia, and I. Hideki, "The Raman spectrum of nano-structured onion-like fullerenes," *Phys. B Condens. Matter*, vol. 357, no. 3–4, pp. 277–281, 2005.

[201] E. D. Bokova-Sirosh, S. N.; Pershina, A. V.; Kuznetsov, V. L.; Ishchenko, A. V.; Moseenkov, S. I.; Orekhov, A. S.; Obraztsova, "Raman Spectra for Characterization of Onion-Like Carbon," *J. Nanoelectron. Optoelectron.*, vol. 8, no. 1, pp. 106–109, 2013.

[202] R. Borgohain, J. Yang, J. P. Selegue, and D. Y. Kim, "Controlled synthesis, efficient purification, and electrochemical characterization of arc-discharge carbon nano-onions," *Carbon N. Y.*, vol. 66, pp. 272–284, 2014.

[203] D. Codorniu Pujals, O. Arias de Fuentes, L. F. Desdin Garcia, E. Cazzanelli, and L. S. Caputi, "Raman spectroscopy of polyhedral carbon nano-onions," *Appl. Phys. A Mater. Sci. Process.*, vol. 120, no. 4, pp. 1339–1345, 2015.

[204] A. Jorio, R. Saito, G. Dresselhaus, and M. S. Dresselhaus, *Raman Spectroscopy in Graphene Related Systems*. Weinheim, Germany, 2011.

[205] N. Sano, T. Charinpanitkul, T. Kanki, and W. Tanthapanichakoon, "Controlled synthesis of carbon nanoparticles by arc in water method with forced convective jet," *J. Appl. Phys.*, vol. 96, no. 1, pp. 645–649, 2004.

[206] N. Sano *et al.*, "Pressure effects on nanotubes formation using the submerged arc in water

method," *Chem. Phys. Lett.*, vol. 378, no. 1–2, pp. 29–34, 2003.

[207] Y. I. Kim, E. Nishikawa, and T. Kioka, "Carbon Nano Materials Produced by Using Arc Discharge in Foam," *J. K. Phy. Soc*, vol. 54, no. 3, pp. 1032–1035, 2009.

[208] S. Jong Lee, H. Koo Baik, J. Yoo, and J. Hoon Han, "Large scale synthesis of carbon nanotubes by plasma rotating arc discharge technique," *Diam. Relat. Mater.*, vol. 11, no. 3–6, pp. 914–917, 2002.

PUBLICATIONS

1. A. Cupolillo, N. Ligato, **S.M. Osman**, and L. S. Caputi, *Carbon K-edge electron-energy-loss near-edge structure in the reflection mode on graphene/Ni(111)*, Appl. Phys. Lett. 109, 161603 (2016); DOI: 10.1063/1.4965856

2. **S.M. Osman** and M. Alsheikh, *Synthesis and characterization of hematite and spinel ferrite ($ZnFe_2O_4$)*, Uni. Kass. Jour. 3, vol. 1, pp. 169-194, (2014).

3. A. Sindona, A. Cupolillo, F. Alessandro, M. Pisarra, D.C. Coello Fiallos, **S.M. Osman**, and L.S. Caputi, *Evidence of an interband π-like plasmon in silicene grown on silver*, submitted to Phys. Rev. Letters

4. F. Alessandro, **S.M. Osman**, A. Sindona, M. Pisarra, A. Cupolillo and L.S. Caputi, *Plasmonic properties of the mixed (4×4, $\sqrt{13}\times\sqrt{13}R19°$,$2\sqrt{3}\times2\sqrt{3}R30^{\circ}$) Silicene phase supported on Ag(111)*, submitted to Phys. Rev. Letters

5. **S.M. Osman**, F. Alessandro, A. Sindona, M. Pisarra, A. Cupolillo and L.S. Caputi, *A comparison of the dielectric properties of two Silicene phases on Ag(111)*, in preparation

6. A. Scarcello, F. Alessandro, **S.M. Osman** and L.S. Caputi, *Carbon nano-onions from underwater arc discharge: a novel crystallization mechanism*, in preparation